

Copyright is owned by the Author of the thesis. Permission is given for a copy to be downloaded by an individual for the purpose of research and private study only. The thesis may not be reproduced elsewhere without the permission of the Author.

**The Linear Wave Response  
of a Single and a Periodic Line-Array of  
Floating Elastic Plates**

A thesis presented in partial fulfillment

of the requirement for the degree of

Doctor of Philosophy

in

Mathematics

at Massey University, Albany, New Zealand

**Cynthia Dewi Wang**

2004

# Abstract

We propose an improved technique to calculate the linear response of a single and multiple plates models due to ocean waves. The single plate model is the basis for the multiple plates model which we take to be a periodic array of identical plates. For the single plate model we solve the plate displacement by the Finite Element Method (FEM) and the water potential by the Boundary Element Method (BEM). The displacement is expanded in terms of the basis functions of the FEM. The boundary integral equation representing the potential is approximated by these basis functions. The resulting integral operator involving the free-surface Green's function is solved using an elementary integration scheme. Results are presented for the single plate model. We then use the same technique to solve for the periodic array of plates problem because the single and the periodic array plates model differ only in the expression of the Green's function. For the periodic array plate model the boundary integral equation for the potential involves a periodic Green's function which can be obtained by taking an infinite sum of the free-surface Green's function for the single plate model. The solution for the periodic array plate is derived in the same way as the single plate model. From this solution we then calculate the waves scattered by this periodic array.

# Acknowledgments

I would like to express my greatest gratitude to Dr. Michael Meylan who has been an excellent supervisor to me and the inspiration for this thesis. I thank him for being a teacher, a father, and a friend to me in the last five years. I would also like to thank my second supervisor Professor Robert McKibbin for his invaluable moral support during the completion of this thesis. I gratefully acknowledge Mr. Adrian Swift who had kindly spared his time to proofread this thesis. I would like to acknowledge the following people: Ms. Jill Duncalfe, Dr. Caroline Meade, the staff of the Health and Counseling Centre of Massey University Albany, and the CATT team of North Shore Hospital for their unconditional love and support. They have made this thesis possible.

# Contents

<b>1</b>	<b>Introduction</b>	<b>1</b>
<b>2</b>	<b>The Three-dimensional Single Floating Elastic Plate Model</b>	<b>8</b>
2.1	The Pictorial Description of the Model	8
2.2	The Mathematical Description of the Model	8
2.2.1	The Equation of Motion for the Water	10
2.2.2	The Equation of Motion for the Plate	11
2.2.3	Non-Dimensionalizing the Variables	11
2.2.4	The Single Frequency Problem	12
2.3	The Application of the Boundary Element Method to the Water Potential	13
2.3.1	Transforming the Boundary Value Problem for the Potential into a Boundary Integral Equation	14
2.3.2	The Free-surface Green's function for water of finite and infinite depth	15
<b>3</b>	<b>Solving the Motion of the Plate and the Water</b>	<b>18</b>
3.1	Discretization of the Plate	18
3.2	The Expansion of the Plate's displacement	19
3.3	Solving for the Displacement of the Plate	22
3.3.1	The variational form of the displacement equation	23
3.3.2	Minimization of the Discretized Variational Equation	23
3.4	Solving the Plate-Water Motion by the Constant Panel Method	26

3.4.1	Solving the Potential.....	27
3.4.2	Coupling the Water and the Plate.....	28
3.5	A Higher Order method to solve the Plate-water motion. ....	29
3.5.1	Solving for the Potential.....	30
3.5.2	Coupling the Plate and the Water.....	34
3.5.3	Numerical Scheme to Solve the Green's Integral Equation.....	34
<b>4</b>	<b>Numerical Implementation and Results of the Higher Order Method.....</b>	<b>37</b>
4.1	Implementing the Mass and the Stiffness Matrices.....	37
4.2	Implementing the Green's Matrix.....	41
4.3	Results.....	43
4.3.1	The Comparison Between Meylan's Method and the Higher Order Method.....	43
4.3.2	The Convergence of the Higher Order Method.....	45
4.3.3	The Displacement of the Plate.....	56
<b>5</b>	<b>An Infinite Line-Array of Periodically-Arranged Identical Plates... ..</b>	<b>62</b>
5.1	The Application of Diffraction Grating.....	62
5.2	The Application of the Floquet's Theorem to the Periodic Grating.....	63
5.3	The Far-field Approximation of the Periodic Green's function.....	66
5.4	Accelerating the periodic Green's function.....	67
<b>6</b>	<b>The Scattering of Waves by the Periodic Line-Array of Plates.....</b>	<b>71</b>
6.1	The Modes of the Scattered Waves.....	71
6.2	The Diffracted, Reflected, and Transmitted Waves.....	73

6.2.1	The Diffracted Waves .....	74
6.2.2	The Reflected and the Transmitted Waves .....	75
6.3	The Energy Balance .....	78
<b>7</b>	<b>Results for the Multiple Plates Model .....</b>	<b>79</b>
7.1	The Convergence of the Periodic Green's Function .....	79
7.2	A Periodic Line-Array of Stiff and Unmovable Plates .....	85
7.2.1	The Case of Joined Square Plates .....	85
7.2.2	The Case of Periodical Square Plates with Gaps .....	85
7.2.3	The Case of Oblique Incident Wave .....	87
7.3	A Periodic Line-Array of Elastic and Separated Plates .....	89
7.3.1	The Dependency of the Scattered Waves to the Wavelength, the Channel Width, and the Incident Angle .....	89
7.3.2	The Scattering of Wave with Various Incident Angles .....	94
7.3.3	The Displacement of the Plates .....	102
<b>8</b>	<b>Summary and Conclusion .....</b>	<b>108</b>
<b>A</b>	<b>The Derivation of the Incident Plane Wave .....</b>	<b>111</b>
<b>B</b>	<b>The Derivation of the Integral Equation for the Potential .....</b>	<b>113</b>
<b>C</b>	<b>Computing the Matrices, the Vectors and the Operators .....</b>	<b>115</b>
<b>D</b>	<b>The Asymptotic Representation of the periodic Green's Function .</b>	<b>119</b>
D.1	The Spatial Representation of the Periodic Green's function .....	119
D.2	The Spectral Representation of the Periodic Green's function .....	120

<b>Bibliography</b> .....	<b>122</b>
<b>Index</b> .....	<b>126</b>

## List of Figures

<b>Figure 2.1.1.</b> The depiction of the domain for the single plate model. ....	9
<b>Figure 3.1.1.</b> The discretisation of a plate of arbitrary geometry by rectangular panels. (a) The plate is covered by $p$ total number of panels where each panel is denoted by $\Delta_d$ and numbering of $d = 1, \dots, p$ is directed by the arrows. (b) Each rectangular panel is of area $4ab$ and its corners are numbered locally by $q_j^{(d)}$ ( $j = 1, 2, 3, 4$ ). In total a plate has $q$ nodes which are the corners of the rectangular panels. ....	20
<b>Figure 4.1.1.</b> The distribution diagram of a panel matrix into the matrix for the plate. ....	42
<b>Figure 4.3.1.</b> The comparison of the plate's displacement generated by Meylan's method with 900 panels (right hand side) and the higher order method with 100 panels (left hand side). The plate is of stiffness $\beta = 0.01$ and mass $\gamma = 0$ . The incident wave has length $\lambda = 2$ and propagates at waveangle $\theta = \pi/6$ . The water is infinitely deep. ....	46
<b>Figure 4.3.2.</b> The diagram showing the five geometries of the plate shapes that will be used to illustrate the subsequent examples using the higher order method. The direction of the incident wave is shown in Figure 2.1.1. ....	49
<b>Figure 4.3.3.</b> An illustration of the effect of panel size on approximating an isosceles triangle. The size of the panels in (b) are double from the ones in (a). ....	50
<b>Figure 4.3.4.</b> The absolute value of the Kochin's function $H(\tau)$ as a function of the angle $\tau$ for a square plate of area 16, mass $\gamma = 0$ , and given stiffness. The number of panels used are 32 (dotted line), 64 (broken line), 128 (chained line), and 256 (solid line). The incident wave of unit amplitude has wavelength $\lambda = 2$ and waveangle $\theta = \pi/6$ . The figures show the energy scattering around the square plate for given stiffness constants $\beta$ . ....	51

- Figure 4.3.5.** The absolute value of the Kochin's function  $H(\tau)$  as a function of the angle  $\tau$  for a triangular plate of area 16, mass  $\gamma = 0$ , and given stiffness. The number of panels used are approximately 32 (dotted line), 64 (broken line), 128 (chained line), and 256 (solid line). The incident wave of unit amplitude has wavelength  $\lambda = 2$  and waveangle  $\theta = \pi/6$ . The figures show the energy scattering around the triangular plate for given stiffness constants  $\beta$ . . . . . 52
- Figure 4.3.6.** The absolute value of the Kochin's function  $H(\tau)$  as a function of the angle  $\tau$  for a circular plate of area 16, mass  $\gamma = 0$ , and given stiffness. The number of panels used are approximately 32 (dotted line), 64 (broken line), 128 (chained line), and 256 (solid line). The incident wave of unit amplitude has wavelength  $\lambda = 2$  and waveangle  $\theta = \pi/6$ . The figures show the energy scattering around the circle plate for given stiffness constants  $\beta$ . . . . . 53
- Figure 4.3.7.** The absolute value of the Kochin's function  $H(\tau)$  as a function of the angle  $\tau$  for a parallelogram plate of area 16, mass  $\gamma = 0$ , and given stiffness. The number of panels used are approximately 32 (dotted line), 64 (broken line), 128 (chained line), and 256 (solid line). The incident wave of unit amplitude has wavelength  $\lambda = 2$  and waveangle  $\theta = \pi/6$ . The figures show the energy scattering around the parallelogram plate for given stiffness constants  $\beta$ . . . . . 54
- Figure 4.3.8.** The absolute value of the Kochin's function  $H(\tau)$  as a function of the angle  $\tau$  for a trapezoidal plate of area 16, mass  $\gamma = 0$ , and given stiffness. The number of panels used are approximately 32 (dotted line), 64 (broken line), 128 (chained line), and 256 (solid line). The incident wave of unit amplitude has wavelength  $\lambda = 2$  and waveangle  $\theta = \pi/6$ . The figures show the energy scattering around the trapezoidal plate for given stiffness constants  $\beta$ . . . . . 55
- Figure 4.3.9.** The displacement of a square plate with area 16, stiffness  $\beta = 0.01$ , and mass  $\gamma = 0$  floating on water of given depth. The plate is discretized using 100 panels. The area integral over the panel uses 16 quadrature points. The incident wave of unit amplitude and length  $\lambda = 2$  propagates at angle  $\theta = \pi/6$ . The figures show that waves with higher frequency (deeper water) affect the plate's displacement more than waves with lower frequency (shallower water). . . . . 57

**Figure 4.3.10.** The displacement of a triangular plate with area 16, stiffness  $\beta = 0.01$ , and mass  $\gamma = 0$  floating on water of given depth. The plate is discretized using 105 panels. The area integral over the panel uses 16 quadrature points. The incident wave of unit amplitude and length  $\lambda = 2$  propagates at angle  $\theta = \pi/6$ . The figures show that waves with higher frequency (deeper water) affect the plate's displacement more than waves with lower frequency (shallower water). . . . . 58

**Figure 4.3.11.** The displacement of a circular plate with area 16, stiffness  $\beta = 0.01$ , and mass  $\gamma = 0$  floating on water of given depth. The plate is discretized using 93 panels. The area integral over the panel uses 16 quadrature points. The incident wave of unit amplitude and length  $\lambda = 2$  propagates at angle  $\theta = \pi/6$ . The figures show that waves with higher frequency (deeper water) affect the plate's displacement more than waves with lower frequency (shallower water). . . . . 59

**Figure 4.3.12.** The displacement of a parallelogram plate with area 16, stiffness  $\beta = 0.01$ , and mass  $\gamma = 0$  floating on water of given depth. The plate is discretized using 110 panels. The area integral over the panel uses 16 quadrature points. The incident wave of unit amplitude and length  $\lambda = 2$  propagates at angle  $\theta = \pi/6$ . The figures show that waves with higher frequency (deeper water) affect the plate's displacement more than waves with lower frequency (shallower water). . . . . 60

**Figure 4.3.13.** The displacement of a trapezoidal plate with area 16, stiffness  $\beta = 0.01$ , and mass  $\gamma = 0$  that floats on water of given depth. The plate is discretized using 116 panels. The area integral over the panel uses 16 quadrature points. The incident wave of unit amplitude and length  $\lambda = 2$  propagates at angle  $\theta = \pi/6$ . The figures show that waves with higher frequency (deeper water) affect the plate's displacement more than waves with lower frequency (shallower water). . . . . 61

**Figure 5.1.1.** The depiction of the periodic surface grating that represents the array of identical floes. . . . . 64

**Figure 6.2.1.** The diagram showing the diffracted waves and the angles of diffraction. . . . . 76

- Figure 7.1.1.** The loglog plot of the relative errors  $\hat{E}_{12}$  (solid line) and  $\hat{E}_{13}$  (chained line) between the near-field periodic Green's function with  $10^6$  terms  $G_{\mathbf{P}}^{(1)}$  and, respectively, the near-field  $G_{\mathbf{P}}^{(2)}$  and the far-field  $G_{\mathbf{P}}^{(3)}$  with the given number of terms. The parameters used are  $X = 0$ ,  $Y = 0.01$ , channel width  $l = 1$ , wavelength  $\lambda = 2$ , and waveangle  $\theta = \pi/4$ . . . . . 81
- Figure 7.1.2.** The loglog plot of the relative error  $\hat{E}_{14}$  between the slow convergent near-field periodic Green's function with  $10^6$  terms  $G_{\mathbf{P}}^{(1)}$  and the fast convergent  $G_{\mathbf{P}}^{(4)}$  calculated using the given number of terms. The number of spatial terms ( $m$ ) is equal to the number of the spectral terms ( $n$ ) in the summation. The smoothing factor is  $c = 0.05$ . Other parameters used are  $X = 0$ ,  $Y = 0.01$ , channel width  $l = 1$ , wavelength  $\lambda = 2$ , and waveangle  $\theta = \pi/4$ . . . . . 82
- Figure 7.1.3.** The plot of the number of terms used in the summation representing the spatial and the spectral parts in the accelerated periodic Green's function versus the smoothing parameter  $c$ . The result from each combination is compared with the one from slow convergent  $G_{\mathbf{P}}$  with  $10^6$  terms. The relative error is set to be of maximum  $10^{-5}$ . The absolute error between results from different combination of parameters is set to be  $10^{-4}$ . The parameters used are  $X = 0$ ,  $Y = 0.01$ , channel width  $l = 1$ , wavelength  $\lambda = 2$ , and waveangle  $\theta = \pi/4$ . . . . . 84
- Figure 7.2.1.** The comparison plot of various wavelengths versus the scattered coefficients due to a periodic array of stiff, unmovable, and joined plates in three dimensional domain and a stiff and unmovable beam in two dimensional. In the three dimensional domain the plates are squares of area 1 (side length of 1), the length of the channel is  $l = 1$  ( $b = 0$ ), and the waveangle is  $\theta = 0$ . In the two dimensional the length of the beam is 1. This figure shows the agreement in the results for the stiff, unmovable, and joined three-dimensional plates with the two-dimensional beam. . . . . 86
- Figure 7.2.2.** The scattering of waves by a periodic array of stiff and unmovable square plates where each has area 16 and is confined by channel of length  $l = 6$ . The incident wave of length  $\lambda = 4$  is oblique at angle  $\theta = -\pi/3$ . There are 3 pairs of diffracted waves of order from 0 to 4 (all are generated in the positive  $y$  region). The amplitude  $|A_m^{\pm}|$  of the scattered wave is shown in Table 7.2.2. . . . . 90

- Figure 7.2.3.** The scattering of waves by a periodic array of stiff and unmovable square plates where each has area 16 and is confined by channel of length  $l = 6$ . The incident wave of length  $\lambda = 4$  is oblique at angle  $\theta = -\pi/6$ . There are 3 pairs of diffracted waves of order from  $M = -1$  (one originated from the negative  $y$  region) to  $N = 3$  (three originated from the positive  $y$  region). The amplitude  $|A_m^\pm|$  of the scattered wave is shown in Table 7.2.3. . . . . 91
- Figure 7.2.4.** The scattering of waves by a periodic array of stiff and unmovable square plates where each has area 16 and is confined by channel of length  $l = 6$ . The incident wave of length  $\lambda = 4$  is oblique at angle  $\theta = 0$ . There are 3 pairs of diffracted waves of order from  $M = -2$  to  $N = 2$  (both positive and negative  $y$  regions generate two). The amplitude  $|A_m^\pm|$  of the scattered wave is shown in Table 7.2.4. . . . . 92
- Figure 7.2.5.** The scattering of waves by a periodic array of stiff and unmovable square plates where each has area 16 and is confined by channel of length  $l = 6$ . The incident wave of length  $\lambda = 4$  is oblique at angle  $\theta = \pi/4$ . There are 3 pairs of diffracted waves of order from  $M = -3$  to  $N = 0$  (all generated in the negative  $y$  region). The amplitude  $|A_m^\pm|$  of the scattered wave is shown in Table 7.2.5. . . . . 93
- Figure 7.3.1.** The scattering of waves of wavelength  $\lambda = 4$  by a periodic array of square plates of area 16, stiffness  $\beta = 0.1$ , and mass  $\gamma = 0$ . Each plate is confined by a channel of width  $l = 6$ . (a) The reflection amplitude  $|R|$  versus the incident angle  $\theta$ . (b) The transmission amplitude  $|T|$  versus the incident angle  $\theta$ . (c) The overlapping plot of the diffracted wave of order 1. (d) The overlapping plot of the diffracted wave of order 2. The waves are directed towards positive  $x$  (solid line) and negative  $x$  (chained line) in the negative  $y$  region and directed towards positive  $x$  (dotted line) and negative  $x$  (dashed line) in the positive  $y$  region. The figures show symmetry about angle  $\theta = 0$  in all the scattered waves and this is due to the symmetry of the shape of the plates and the periodic gratings. . . . . 97
- Figure 7.3.2.** The scattering of waves of wavelength  $\lambda = 4$  by a periodic array of triangular plates of area 16, stiffness  $\beta = 0.1$ , and mass  $\gamma = 0$ . Each plate is confined by a channel of width  $l = 6$ . (a) The reflection amplitude  $|R|$  versus the incident angle  $\theta$ . (b) The

transmission amplitude  $|T|$  versus the incident angle  $\theta$ . (c) The overlapping plot of the diffracted wave of order 1. (d) The overlapping plot of the diffracted wave of order 2. The waves are directed towards positive  $x$  (solid line) and negative  $x$  (chained line) in the negative  $y$  region and directed towards positive  $x$  (dotted line) and negative  $x$  (dashed line) in the positive  $y$  region. The scattered waves are not symmetric about  $\theta = 0$  because the shape of the plates are not symmetric. . . . . 98

**Figure 7.3.3.** The scattering of waves of wavelength  $\lambda = 4$  by a periodic array of circle plates of area 16, stiffness  $\beta = 0.1$ , and mass  $\gamma = 0$ . Each plate is confined by a channel of width  $l = 6$ . (a) The reflection amplitude  $|R|$  versus the incident angle  $\theta$ . (b) The transmission amplitude  $|T|$  versus the incident angle  $\theta$ . (c) The overlapping plot of the diffracted wave of order 1. (d) The overlapping plot of the diffracted wave of order 2. The waves are directed towards positive  $x$  (solid line) and negative  $x$  (chained line) in the negative  $y$  region and directed towards positive  $x$  (dotted line) and negative  $x$  (dashed line) in the positive  $y$  region. The figures show symmetry about angle  $\theta = 0$  in all the scattered waves and this is due to the symmetry of the shape of the plates and the periodic gratings. . . . . 99

**Figure 7.3.4.** The scattering of waves of wavelength  $\lambda = 4$  by a periodic array of parallelogram plates of area 16, stiffness  $\beta = 0.1$ , and mass  $\gamma = 0$ . Each plate is confined by a channel of width  $l = 6$ . (a) The reflection amplitude  $|R|$  versus the incident angle  $\theta$ . (b) The transmission amplitude  $|T|$  versus the incident angle  $\theta$ . (c) The overlapping plot of the diffracted wave of order 1. (d) The overlapping plot of the diffracted wave of order 2. The waves are directed towards positive  $x$  (solid line) and negative  $x$  (chained line) in the negative  $y$  region and directed towards positive  $x$  (dotted line) and negative  $x$  (dashed line) in the positive  $y$  region. The scattered waves are not symmetric about  $\theta = 0$  because the shape of the plates are not symmetric. . . . . 100

**Figure 7.3.5.** The scattering of waves of wavelength  $\lambda = 4$  by a periodic array of trapezoidal plates of area 16, stiffness  $\beta = 0.1$ , and mass  $\gamma = 0$ . Each plate is confined by a channel of width  $l = 6$ . (a) The reflection amplitude  $|R|$  versus the incident angle  $\theta$ . (b) The transmission amplitude  $|T|$  versus the incident angle  $\theta$ . (c) The overlapping plot of the diffracted wave of order 1. (d) The overlapping plot of the diffracted wave of order 2. The waves are

directed towards positive  $x$  (solid line) and negative  $x$  (chained line) in the negative  $y$  region and directed towards positive  $x$  (dotted line) and negative  $x$  (dashed line) in the positive  $y$  region. The figures show symmetry about angle  $\theta = 0$  in all the scattered waves and this is due to the symmetry of the shape of the plates and the periodic gratings. . . . . 101

**Figure 7.3.6.** The displacement plot of five square plates as part of the periodic array. Each plate has area 16, stiffness  $\beta = 0.1$ , mass  $\gamma = 0$ , and is confined by a channel of width  $l = 6$ . The array is subjected to incident wave of wavelength (a)  $\lambda = 4$  and (b)  $\lambda = 8$ . The incident angle is  $\theta = \pi/6$ . . . . . 103

**Figure 7.3.7.** The displacement plot of five triangular plates as part of the periodic array. Each plate has area 16, stiffness  $\beta = 0.1$ , mass  $\gamma = 0$ , and is confined by a channel of width  $l = 6$ . The array is subjected to incident wave of wavelength (a)  $\lambda = 4$  and (b)  $\lambda = 8$ . The incident angle is  $\theta = \pi/6$ . . . . . 104

**Figure 7.3.8.** The displacement plot of five circular plates as part of the periodic array. Each plate has area 16, stiffness  $\beta = 0.1$ , mass  $\gamma = 0$ , and is confined by a channel of width  $l = 6$ . The array is subjected to incident wave of wavelength (a)  $\lambda = 4$  and (b)  $\lambda = 8$ . The incident angle is  $\theta = \pi/6$ . . . . . 105

**Figure 7.3.9.** The displacement plot of five parallelogram plates as part of the periodic array. Each plate has area 16, stiffness  $\beta = 0.1$ , mass  $\gamma = 0$ , and is confined by a channel of width  $l = 6$ . The array is subjected to incident wave of wavelength (a)  $\lambda = 4$  and (b)  $\lambda = 8$ . The incident angle is  $\theta = \pi/6$ . . . . . 106

**Figure 7.3.10.** The displacement plot of five trapezoidal plates as part of the periodic array. Each plate has area 16, stiffness  $\beta = 0.1$ , mass  $\gamma = 0$ , and is confined by a channel of width  $l = 6$ . The array is subjected to incident wave of wavelength (a)  $\lambda = 4$  and (b)  $\lambda = 8$ . The incident angle is  $\theta = \pi/6$ . . . . . 107

## List of Tables

**Table 4.3.1.** The error  $E_{mn}$  in the results by Meylan’s method using different number of panels. Column  $n$  represents the varying number of panels and column  $m$  is the reference of 2500 panels. The plate used is a square with area 16, stiffness  $\beta = 0.01$ , and mass  $\gamma = 0$ . The wave parameters are  $\lambda = 2$  and  $\theta = \pi/6$ . The table shows that the result converges as we increase the number of panels used to discretized the plate..... 44

**Table 4.3.2.** The error  $E_{mn}$  in the results produced by the higher order method using different number of panels. Column  $n$  represents the varying number of panels and column  $m$  is the reference of 900 panels. The plate used is a square with area 16, stiffness  $\beta = 0.01$ , and mass  $\gamma = 0$ . The wave parameters are  $\lambda = 2$  and  $\theta = \pi/6$ . The table shows that the result converges as we increase the number of panels used to discretized the plate..... 44

**Table 4.3.3.** The error  $E_{mn}$  in the results by Meylan’s low order method versus the results by the higher order method. Column  $n$  represents Meylan’s method that uses various number of panels and column  $m$  is the reference that is the higher order method with 900 panels. The plate used is a square with area 16, stiffness  $\beta = 0.01$ , and mass  $\gamma = 0$ . The wave parameters are  $\lambda = 2$  and  $\theta = \pi/6$ . The table shows that the accuracy using 2500 panels in Meylan’s method is equivalent to the accuracy using 900 panels in the higher order method..... 44

**Table 4.3.4.** The error  $E_{QP}$  showing the convergence of the higher order method using various number of panels versus number of quadrature points. The referencing result uses 900 panels and 64 quadrature points. The area of the square plate is 16, its stiffness is  $\beta = 0.01$ , and its mass is  $\gamma = 0$ . The wavelength is  $\lambda = 2$  and the waveangle is  $\theta = 0$ . ..... 48

**Table 7.2.1.** The convergence of the total energy for identical plates with area 16. Each plate is discretized using the specified number of panels. The width of the channel is  $l = 12$ . The parameters for the incident wave are  $\lambda = 8$  and  $\theta = 0$ . The incoming energy is 1. .... 88

<b>Table 7.2.2.</b> Table of the scattered amplitude $A_m^-$ and $A_m^+$ ( $0 \leq m \leq 2$ ) depicted by Figure 7.2.2. due to a periodic array of plates of area 16. The incident wave is oblique at angle $\theta = -\pi/3$ . The scattered amplitudes of diffraction order $m = 0$ represents the reflected amplitude $R = A_0^-$ and the transmitted amplitude $T = 1 - A_0^+$ .....	90
<b>Table 7.2.3.</b> Table of the scattered amplitude $A_m^-$ and $A_m^+$ ( $-1 \leq m \leq 2$ ) depicted by Figure 7.2.3. due to a periodic array of plates of area 16. The incident wave is oblique at angle $\theta = -\pi/6$ . The scattered amplitudes of diffraction order $m = 0$ represents the reflected amplitude $R = A_0^-$ and the transmitted amplitude $T = 1 - A_0^+$ .....	91
<b>Table 7.2.4.</b> Table of the scattered amplitude $A_m^-$ and $A_m^+$ ( $-1 \leq m \leq 1$ ) depicted by Figure 7.2.4. due to a periodic array of plates of area 16. The incident wave is oblique at angle $\theta = 0$ . The scattered amplitudes of diffraction order $m = 0$ represents the reflected amplitude $R = A_0^-$ and the transmitted amplitude $T = 1 - A_0^+$ .....	92
<b>Table 7.2.5.</b> Table of the scattered amplitude $A_m^-$ and $A_m^+$ ( $-2 \leq m \leq 0$ ) depicted by Figure 7.2.5. due to a periodic array of plates of area 16. The incident wave is oblique at angle $\theta = \pi/4$ . The scattered amplitudes of diffraction order $m = 0$ represents the reflected amplitude $R = A_0^-$ and the transmitted amplitude $T = 1 - A_0^+$ .....	93
<b>Table 7.3.1.</b> The number of diffracted waves $M$ generated in the negative $y$ region for various $\lambda$ and $l$ while $\theta = 0$ . .....	95
<b>Table 7.3.2.</b> The number of diffracted waves $N$ generated in the positive $y$ region for various $\lambda$ and $l$ while $\theta = 0$ . Adding the value of this table to its counter part in Table 7.3.1. gives the total number of diffracted waves for the specified $\lambda$ and $l$ . Both this table and Table 7.3.1. show that the variability of the diffraction waves number depends greatly on $\lambda$ and $l$ . .....	95
<b>Table 7.3.3.</b> The number of diffracted waves generated in the negative $y$ region for varying $\theta$ and $l$ while $\lambda = 8$ is constant. ....	95

**Table 7.3.4.** The number of diffracted waves generated in the positive  $y$  region for varying  $\theta$  and  $l$  while  $\lambda = 8$  is constant. Adding the values in this table to its counterpart in Table 7.3.3. gives the total number of diffracted waves for the specified  $\theta$  and  $l$ . This table and Table 7.3.3. show that the varying angle causes the number of diffracted waves to vary as well. Nevertheless the number of the diffracted waves in the opposite  $y$  regions 'moves' with the angle as it traverses about  $\theta = 0$ . . . . . 96

## Nomenclature

$\Omega$	water domain
$\Delta$	plate-covered area
$H$	water depth
$\lambda$	wavelength
$k$	wavenumber
$\theta$	wave-angle
$\omega$	angular frequency
$\Phi$	dimensional, time-dependent water potential
$W$	dimensional, time-dependent surface displacement
$L$	arbitrary length variable
$\phi$	dimensionless, spatial-dependent water potential
$\phi^{In}$	incident wave
$\phi^s$	scattered wave
$w$	dimensionless, spatial-dependent water potential
$\alpha$	dimensionless angular frequency
$\beta$	stiffness constant
$\gamma$	mass constant
$A^{In}$	incident amplitude
$p$	total number of panels
$q$	total number of nodes
$a$	half length of the side of a panel
$q_j^{(d)}$	index of the $j$ -th node of panel $d$
$H_0(x)$	Struve function of order zero
$J_0(x)$	first kind Bessel function of order zero
$Y_0(x)$	second kind Bessel function of order zero
$H_0(x)$	Hankel function of order zero
$P_j(x)$	Legendre polynomial of order $j$
$P, Q$	total number of integration point
$l$	width of a channel
$b$	width of a gap
$\sigma l$	phase difference
$\sigma_m$	propagation constant in $y$ -direction
$\mu_m$	propagation constant in $x$ -direction
$c$	smoothing parameter
$\psi_m^\pm$	angle of diffraction
$\tilde{\phi}_m^\pm$	diffracted wave
$A_m^\pm$	diffracted amplitude
$M$	lower diffraction order
$N$	upper diffraction order

# Chapter 1

## Introduction

The thin elastic plate model is used to depict a thin and flat structure floating on the water surface. The structure's thickness is far smaller than its length and width. The structure is flexible and rocks in response to the water motion; we neglect its submerged part. This is known as the shallow-draft model.

The thin elastic plate model arises from the need to understand the hydroelastic behaviour of realistic structures, such as a Very Large Floating Structure (VLFS) and ice floes in the Marginal Ice Zone (MIZ), when exposed to the ocean waves. A VLFS (e.g. the megafloat and floating runway) is usually rectangular while ice floes have irregular shapes and usually come in packs.

The VLFS is aimed to provide space for additional airports, storage, etc. Experimental observations have been made by building small-scale models both offshore and in the wavetanks. On the theoretical side numerous methods of calculating the response of the VLFS have been developed. Reviews on both experimental and theoretical works are given by Kashiwagi (2000) and Watanabe et al. (2004). We shall discuss selective examples of the solution methods. Generally the methods separately solve the water at the interface with the plate and the wave-induced response of the plate. The water part can be solved by either calculating the pressure (referred to as the pressure-distribution method) or the velocity potential. The plate part can be solved by either calculating the vibration modes of the plate's deflection (referred to as the modes-expansion method) or solving the displacement directly.

In the water part the solution sought can be in terms of the pressure or the velocity potential. If the pressure is calculated (referred to as the pressure-distribution ) then the potential is eliminated from the Bernoulli-Euler equation and the pressure across the interface is represented by an integral equation involving a zero-draft Green's function. If the velocity potential of the water is calculated then the pressure is eliminated from the

Bernoulli-Euler's equation by substituting it with the linearized Bernoulli's law. In either approaches the solution involves the displacement of the plate .

The pressure-distribution method may yield solutions at either the interface between the water and the plate (known as the wet modes) or the interface between the plate and the atmosphere (known as the dry modes). An early solution for the dry modes was presented by Maeda (1995) using 1-D free-free modes of the beam in the  $x$  and  $y$  direction. Takaki & Gu, 1996 solved for the dry modes using the eigenfunctions of the Bernoulli-Euler's equation with constant pressure. Later Lin and Takaki (1998) showed that B-spline functions could be used as the modes. In fact the dry modes can be represented by various functions. The wet modes can be calculated from the dry modes by adding the mass and damping factors (Hamamoto, 1997).

The numerical solution for the pressure-distribution using the modes-expansion method is done by discretizing the plate into panels and representing the pressure by a set of arbitrary functions. Then the plate displacement is solved by way of one of these two approaches: the thin plate vibration mode (referred to as the mode-expansion method) or the direct method. The following are examples of the functions used to represent the pressure in the panels. Maeda et al. (1995) and Takaki and Gu (1996) assumed that the unknown pressure was constant on each panel. Another method by Yasuzawa et al. (1996) used the pressure as a linear function. Hamamoto et al. (1997) used an 8-point quadratic function for the pressure on each panels. The drawback of these methods is the lengthy computation time for short wavelengths. For this purpose, Kashiwagi (1996) proposed an efficient computation scheme using the bi-cubic B-spline functions to represent the unknown pressure on each panel.

In the mode-expansion method the unused vibration modes are included to calculate the deflection of the flexible plate. The calculation of these unused modes was costly and hence this method was undesirable. This is because the primary solution sought is the total displacement and not the vibration modes. Therefore the direct method was developed to bypass these unused modes. Yago and Endo (1996) used a standard third degree polynomial of the finite element method (FEM) and the pressure-distribution method to couple

the water and the plate. The panels were discrete and only moved vertically. The panel displacement was then substituted into the pressure forcing equation. The results found were presented in the form of the diffracted potential, the dry and the wet modes of the plate, and a comparison of the computed result with experimental data. Yasuzawa et al. (1996) also used the standard third degree polynomial; however their panels were connected rigidly or by pins. Also the Boundary Element Method (BEM) was used for the water potential. This was solved using Bi-linear boundary elements and numerical integration with 16 Gauss points. Their results were presented as calculation of the wet modes (i.e. the potential at the interface between the plate and the water). Hamamoto (1997) used the standard second degree polynomial on connected panels (modules) that were anchored to the seabed. Like Yasuzawa, Hamamoto used the BEM for the potential. This was done by discretizing the boundary into 4-node linear elements. The potential was expanded in terms of the FEM's polynomial. Both Yasuzawa and Hamamoto used the linearized Bernoulli's equation for the pressure to couple the plate and the water.

Recently Kashiwagi (1998) developed an effective computational scheme for the short wavelength case. The method involved a set of bi-cubic B-spline functions representing the unknown pressure and converting the integral equation for the pressure into a linear system of equations by a Galerkin Scheme (referred to as the bi-cubic B-spline Galerkin scheme). The linear system was solved to give the constants of the bi-cubic B-spline functions. This method is of higher order due to the use of the Galerkin scheme but it is difficult to extend to solve plates that are not rectangular. This restricts its use on other shapes.

Rather than a rectangular shape (on which the VLFS is based on generally) a circular plate model was developed by Meylan and Squire (1996). The model was used to represent a single ice floe in the Marginal Ice Zone (MIZ). The water potential was related to the motion of the circular floe by a boundary integral equation involving an infinite-depth Green's function. This integral equation was solved by expanding the motion in terms of the eigenvalues of circular thin plates. An alternative solution was found using a different Green's

function involving the eigenvalues of a circular ice floe. The results were calculated for long crested ocean waves.

Models based on plates of arbitrary geometry were in fact developed to investigate the behaviour of ice floes in the MIZ. There are many interpretations on the meaning of MIZ. Wadhams (1986) describes the MIZ as the ice-covered part of the polar region that is close enough to the open ocean boundary to be affected by its presence. Since the MIZ is greatly affected by ocean swell it is composed of many ice floes which differ in shape and size. Various experiments have been conducted around the region and numerous models have been developed to depict the floes and the ocean waves. In modelling the MIZ, several of its features are investigated including the break-up of ice sheets into ice floes, the arrangement of floes into patterns by ocean waves, and the dispersion and the attenuation of ocean waves by the ice floes. A detailed summary on the mathematical study of the waves and the MIZ is given by Squire et al. (1995).

A generalized model of a thin elastic plate of arbitrary geometry was developed by Hermans (2000) and Meylan (2002). Hermans performed extensive calculations of the diffraction of waves by such a platform using the boundary element method. Current-induced and non-current-induced free-surface Green's functions were presented and both kinds were solved numerically. The integro-differential equation obtained via the boundary element method was solved by two approaches. The first approach used a set of orthogonal functions that are the eigenfunctions corresponding to the eigenmodes of the deflection of the plate. However it was difficult to extend this method to solve the two-dimensional platform problem. Therefore Hermans gave an alternative approach using the finite difference method with grids of equal length. The application of this technique to the two-dimensional platform was shown but computations were given only for the one dimensional platform in long crested-waves.

A similar model based on a plate of arbitrary geometry was developed by Meylan (2002) to model an ice floe. He used a hybrid finite element-boundary element method to calculate the response of the ice floe. The FEM was used to determine the modes of vibration of an elastic plate. The BEM was used to convert the laplacian and the boundary

conditions of the water potential into an integral equation involving the free-surface Green's function. The integration was then solved using the constant panel method, a method of lower order.

Since the MIZ is composed of many ice floes this leads to the development of multiple floe models from the single floe ones. An early model based on a single floe model was proposed by Masson and LeBlond (1989). They used a model where the floe was circular and rigid. Hence its movement was restricted by its mass and rigidity. Based on single floe scattering they developed a multiple scattering theory using the energy balance equation of the wave spectra where it included the wind-generated energy, the dissipated energy, and the non-linear interaction between the spectrum. An improved model was later developed by Meylan et al. (1997). Meylan et al. used a circular, flexible plate to represent the solitary ice floe. Furthermore the wind-generated energy and the non-linear interaction terms were dropped from the energy balance equation. Apart from these two works there are many other works on the modelling the behaviour of ice floes in the MIZ; for example Marchenko and Voliak (1996) who also worked on the scattering model and Moritz and Ukita (2000) who worked on the deformation of the ice pack.

Here we are interested in studying the scattering of waves by plates of arbitrary geometry. We base the multiple plate model on the single plate model. For the multiple plates models we use a periodic array of plates. For the single plate model we present a solution method analogous to Meylan (2002) but of higher order. This thesis is separated into two parts based on the single and the multiple model.

In the first part of this thesis we present the full solution to the single plate model using the direct method. We shall also compare our methodology with the one used by Meylan. In the first chapter we describe the single plate model physically and mathematically. In the physical description of the model we portray the plate of arbitrary geometry and the water domain and then we show the mathematical formulation of the problem. In second chapter the solution of the plate displacement is discussed. This involves discretizing the plate into a finite number of rectangular (later square) panels and expressing the equation of motion for the plate in terms of its variational equation. The variational equa-

tion is then solved directly using the FEM basis functions. In the third chapter we solve the boundary integral equation for the water potential and then couple the water and the plate together. There are two approaches to solve the integral equation; one is to use the constant panel method (as used by Meylan) and the other is to combine the FEM basis functions with an elementary numerical integration scheme. Both methods will be shown. Since the free-surface Green's function involved in the integral equation is singular we also show ways to avoid the singularity. In the fourth chapter we implement the higher order method. We omit the implementation of Meylan's method as this has already been done and results have been presented. The result for the higher order method is derived in terms of the displacement of the plate and/or the velocity potential of the water. These are then compared to Meylan's results and later are shown to perform better. The effect of discretization on various shapes is also shown using Kochin's function. Finally the response of a plate of various shapes is plotted in terms of its displacement.

For the second part of this thesis the solution of the single plate using a higher order method is extended to solve an infinite line-array of periodically-arranged identical plates. We note that similar problem have been solved by Fernyhough and Evans (1995) and Potter and Evans (1998). Fernyhough and Evans solved the scattering by a periodic array of rectangular vertical barriers that extended throughout the water depth. Porter and Evans considered the problem of trapped modes which are Rayleigh-Bloch surface waves in a periodic array of circular cylinder that also extended throughout the water depth. The difference between the two and our periodic array of plates is that the rectangular barrier and the circular cylinder are stiff and unmoved whereas our plates are elastic and movable. However our integral equation for the water potential is similar to theirs.

In the fifth chapter we describe the periodic array of plates. Here we pose the problem that we aim to solve. Such arrangement of plates resembles the surface diffraction grating of Optics. Therefore the diffraction theory will be applied to the coupled plate-water motion. The application of the diffraction theory then gives rise to a new type of integral operator analogous to the single plate's one. We then introduce its kernel, the free-surface periodic Green's function. However the periodic Green's function is slow-

convergent, and so we propose a new approach to accelerate the convergence of this function. In the sixth chapter the derivation of the scattered waves using the modal approach is presented. The modes are found using the Fourier Transform of the asymptotic form of the periodic Green's function. We also classify the diffracted, the reflected, and the transmitted waves and this leads to the calculation of energy balance within the periodic array. Finally we present the results for this periodic array of plates problem in the seventh chapter.

# Chapter 2

## The Three-dimensional Single Floating Elastic Plate Model

We begin with the physical and mathematical model for the problem of the linear wave forcing of a single plate floating on the surface of, either, finitely or infinitely deep water.

### 2.1 The Pictorial Description of the Model

In this section we portray the fluid domain and the plate model for the problem and explain the notation. Figure 2.1.1. depicts the physical domain of the response problem where a thin elastic plate is floating on the surface of water that may be finite or infinite in depth. We denote the entire water domain by  $\Omega$  and the plate covered area is denoted by  $\Delta$ . The surface is at  $z = 0$  and the seafloor (the bottom of the water domain) is  $z = -H$ . For infinitely deep water we take the limit as  $H \rightarrow \infty$ . We neglect the submerged part of the plate (i.e. the surface of the plate is also at  $z = 0$ ) The axis are shown in the figure. An incident wave of amplitude  $A^n$  propagates at direction specified by waveangle  $\theta$ .

### 2.2 The Mathematical Description of the Model

We now present the mathematical model associated with the problem of a single plate floating in the previous section. This theory comes from Stoker [Stoker, 1957], Meylan [Meylan, 2002], and Kashiwagi [Kashiwagi, 1998a], amongst others.

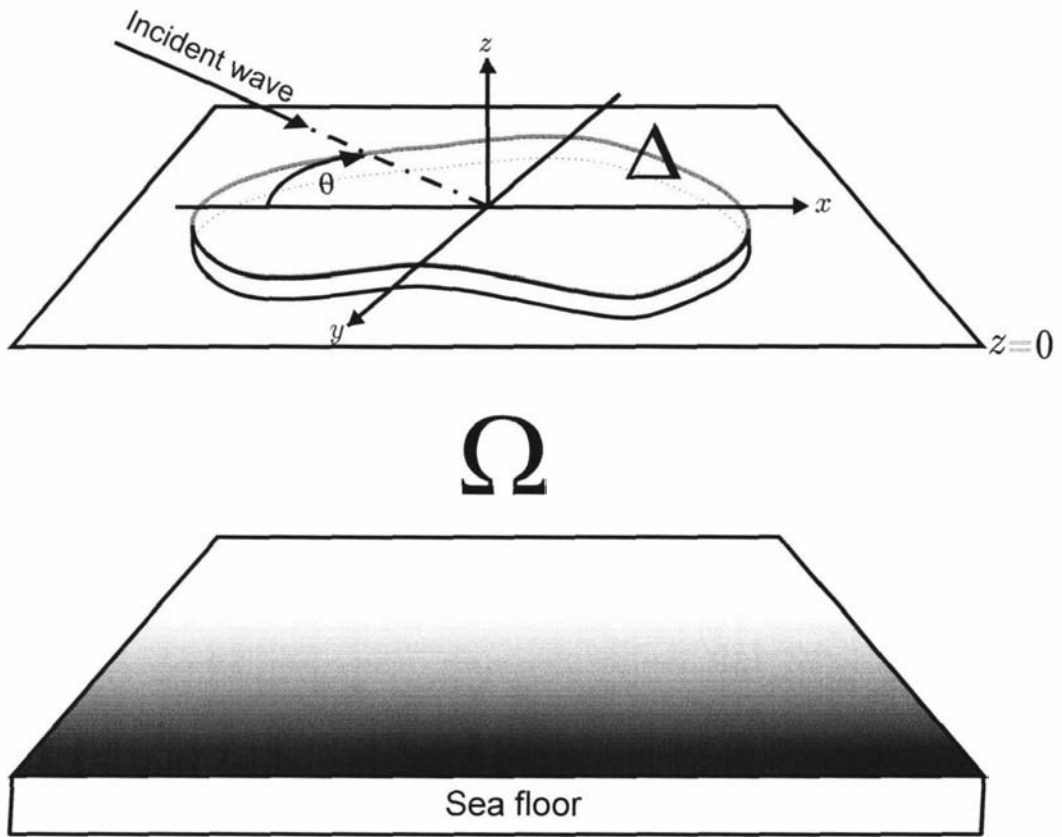


Figure 2.1.1. The depiction of the domain for the single plate model.

### 2.2.1 The Equation of Motion for the Water

We use the linear wave diffraction theory. Assuming that the water flow is irrotational, the velocity potential of the water must satisfy Laplace's equation

$$\nabla^2 \Phi(x, y, z; t) = 0, \quad (x, y, z) \in \Omega, \quad 0 \leq t < \infty, \quad (2.2.1)$$

where  $\Phi(x, y, z; t)$  is the velocity potential of the water. At the water surface the kinematic boundary condition applies

$$\frac{\partial}{\partial z} \Phi(x, y, 0; t) = \frac{\partial}{\partial t} W(x, y; t). \quad (2.2.2)$$

At the interface between the water and the plate the dynamical boundary condition is given by the linearized Bernoulli's Law

$$-\rho \left( \frac{\partial}{\partial t} \Phi(x, y, 0; t) + gW(x, y; t) \right) = p(t) \quad (2.2.3)$$

where  $W(x, y; t)$  is the surface displacement,  $\rho$  is the density of the water, and  $g$  is the gravitational acceleration. At the free surface (the interface between the water and the atmosphere) the pressure is constant. Thus if we take the time derivative of equation (2.2.3) then  $\frac{\partial p}{\partial t} = 0$  and the substitution of (2.2.2) gives rise to condition

$$\frac{\partial^2 \Phi}{\partial t^2} + g \frac{\partial \Phi}{\partial z} = 0.$$

At a fixed surface of the water domain (such as the seafloor) the boundary condition is  $\frac{\partial \Phi}{\partial n} = 0$ , where  $n$  denotes the direction normal to the surface. For water with finite depth the bottom boundary condition is

$$\frac{\partial}{\partial z} \Phi(x, y, -H; t) = 0, \quad (2.2.4)$$

where  $H$  denotes the depth of the water. For infinitely deep water the boundary condition at the bottom becomes

$$\lim_{z \rightarrow -\infty} \text{grad } \Phi = 0. \quad (2.2.5)$$

### 2.2.2 The Equation of Motion for the Plate

The equation of motion for the plate is given by the Bernoulli-Euler equation. For an isotropic plate this is

$$D\nabla^4 W + \rho' h \frac{\partial^2 W}{\partial t^2} = p(t), \quad (2.2.6)$$

together with the free edge boundary conditions

$$\frac{\partial^2 W}{\partial n^2} + \nu \frac{\partial^2 W}{\partial s^2} = 0, \quad (2.2.7)$$

$$\frac{\partial^3 W}{\partial n^3} + (2 - \nu) \frac{\partial^3 W}{\partial s^3} = 0, \quad (2.2.8)$$

where  $W(x, y, t)$  is the plate displacement,  $\rho'$  is the plate density,  $h$  is the plate thickness,  $p$  is the pressure, and  $D$  is the modulus of rigidity of the plate ( $D = Eh^3/12(1 - \nu^2)$ , where  $E$  is the Young's modulus and  $\nu$  is the Poisson's ratio).  $n$  and  $s$  are, respectively, the normal and the tangential directions to the plate edge.

Under the surface of the water covered by the plate we couple equations (2.2.3) and (2.2.6) and obtain the following relation

$$D\nabla^4 W + \rho' h \frac{\partial^2 W}{\partial t^2} = -\rho \frac{\partial \Phi}{\partial t} - \rho g W, \quad (2.2.9)$$

which is the coupled pressure equation. Equation (2.2.9) describes the surface displacement of the plate on the wetted interface.

### 2.2.3 Non-Dimensionalizing the Variables

We non-dimensionalize the spatial variables using

$$x = L\bar{x}, \quad y = L\bar{y}, \quad z = L\bar{z}, \quad W = L\bar{W},$$

and the time variables using

$$t = \sqrt{\frac{L}{g}}\bar{t}, \quad \Phi = L\sqrt{Lg}\bar{\Phi},$$

where  $L$  is a length parameter which may be chosen arbitrarily. Substituting the dimensionless variables into (2.2.9) gives us the displacement equation for the plate on the water

interface

$$\beta \nabla^4 \bar{W} + \gamma \frac{\partial^2 \bar{W}}{\partial \bar{t}^2} = -\frac{\partial \bar{\Phi}}{\partial \bar{t}} - \bar{W}, \quad (2.2.10)$$

where the new constant terms  $\beta$  and  $\gamma$  are

$$\begin{aligned} \beta &= \frac{D}{\rho L^4 g} \\ \gamma &= \frac{\rho' h}{\rho L}. \end{aligned} \quad (2.2.11)$$

We will call  $\beta$  the *stiffness constant* and  $\gamma$  the *mass constant*. Subsequently we shall omit the overbar from all variables.

## 2.2.4 The Single Frequency Problem

Assuming the problem is single frequency we may write the displacement of the plate and the velocity potential of the water as

$$\begin{aligned} W(x, y, t) &= \operatorname{Re} [w(x, y) e^{-i\omega t}], \\ \Phi(x, y, z, t) &= \operatorname{Re} [\phi(x, y, z) e^{-i\omega t}], \end{aligned}$$

where  $\omega$  is the angular frequency of the wave.

Then the single frequency equation of motion for the water becomes

$$\nabla^2 \phi = 0, \quad (x, y, z) \in \Omega, \quad (2.2.12)$$

$$\frac{\partial \phi}{\partial z} - \frac{\omega^2}{g} \phi = 0, \quad (x, y) \notin \Delta, z = 0, \quad (2.2.13)$$

$$\frac{\partial \phi}{\partial z} = -i\omega w, \quad (x, y) \in \Delta, z = 0, \quad (2.2.14)$$

For finite depth  $H$  the condition that  $\frac{\partial \phi}{\partial n} = 0$  at a fixed surface gives

$$\frac{\partial \phi}{\partial z} = 0, \quad z = -H, \quad (2.2.15)$$

and for infinitely deep water

$$\lim_{z \rightarrow -\infty} \left| \frac{\partial \phi}{\partial z} \right| = 0. \quad (2.2.16)$$

The boundary condition at infinity is given by the Sommerfeld radiation condition. This imposes the scattered wave must progress outward [Wehausen & Laitone, 1960]

$$\lim_{|\mathbf{x}| \rightarrow \infty} \sqrt{|\mathbf{x}|} \left( \frac{\partial}{\partial |\mathbf{x}|} - ik \right) (\phi - \phi^{In}) = 0, \quad (2.2.17)$$

where  $k$  is the wavenumber (related to the wavelength  $\lambda$  by  $k = 2\pi/\lambda$ ) and  $\phi^{In}$  is an incident plane wave. Condition (2.2.17) ensures uniqueness of the solution of the boundary value problem given in (2.2.1) to (2.2.15) for water of finite depth or (2.2.16) for water of infinite depth. The derivation of incident wave  $\phi^{In}$  is given in Appendix A. We obtain

$$\phi^{In}(\mathbf{x}) = A^{In} e^{ik(x \cos \theta + y \cos \theta)}, \quad (2.2.18)$$

where  $\theta$  is incident angle. Expression (2.2.18) will be used through out this thesis as the incident wave.

Finally equation (2.2.10) becomes the dimensionless and single frequency displacement equation for the plate

$$\beta \nabla^4 w(\mathbf{x}) - \alpha \gamma w(\mathbf{x}) = i\sqrt{\alpha} \phi(\mathbf{x}) - w(\mathbf{x}), \quad (2.2.19)$$

where

$$\alpha = \omega^2, \quad (2.2.20)$$

is the dimensionless frequency. Equation (2.2.19) is one of two simultaneous equations that govern the coupled motion of the water and the plate.

## 2.3 The Application of the Boundary Element Method to the Water Potential

In this section we derive another equation for the water that will be solved simultaneously together with (2.2.19) for the potential of the water and the displacement of the plate. This will produce a boundary integral equation for the potential that involves the Free-Surface Green's function.

### 2.3.1 Transforming the Boundary Value Problem for the Potential into a Boundary Integral Equation

The potential  $\phi$  can be separated into the incident part and the scattered part

$$\phi(\mathbf{x}, \zeta) = \phi^{In}(\mathbf{x}, \zeta) + \phi^s(\mathbf{x}, \zeta), \quad (2.3.1)$$

where  $\phi^{In}$  is the incident wave (2.2.18) and  $\phi^s$  is the scattered potential.

Clearly  $\phi^{In}$  and  $\phi^s$  satisfy the boundary value problem given by Laplace's equation (2.2.12), surface boundary conditions (2.2.13), bottom boundary condition (2.2.15), and the radiation condition (2.2.17). Then we apply Green's second theorem to  $\phi^s$

$$\int_{\Omega} (\phi^s \nabla^2 G - G \nabla^2 \phi^s) dV_{\xi, \zeta} = \int_{\partial\Omega} \left( \phi^s \frac{\partial G}{\partial z} - G \frac{\partial \phi^s}{\partial z} \right) dS_{\xi},$$

where  $\partial\Omega$  is the boundary surrounding domain  $\Omega$  ([John, 1950], [Sarpkaya & Isaacson, 1981]).

Upon applying the Laplacian (2.2.12) and (2.3.4) to the left hand side and (2.3.1) to the right hand side the equation above becomes

$$\phi^s = \int_{\partial\Omega} \left[ \left( \alpha G \phi - G \frac{\partial \phi}{\partial \zeta} \right) - \left( \alpha G \phi^{In} - G \frac{\partial \phi^{In}}{\partial \zeta} \right) \right] dS_{\xi}.$$

We explain in Appendix B that the calculation of the integral over the boundary is reduced to the calculation of its integrand over the plate-covered area. Using this result we obtain

$$\phi^s = \int_{\Delta} \left( \alpha G \phi - G \frac{\partial \phi}{\partial \zeta} \right) dS,$$

since  $\alpha G \phi^{In} - G \frac{\partial \phi^{In}}{\partial z} = 0$  at  $z = 0$  by (2.2.13) satisfied by  $\phi^{In}$  everywhere on the surface.

Furthermore we can apply the boundary condition (2.2.14)

$$\phi^s(\mathbf{x}, z) = \int_{\Delta} [\alpha G(\mathbf{x}, z; \boldsymbol{\xi}, 0) \phi(\boldsymbol{\xi}, 0) + i\sqrt{\alpha} G(\mathbf{x}, z; \boldsymbol{\xi}, 0) w(\boldsymbol{\xi}, 0)] dS_{\xi}, \quad (2.3.2)$$

where  $G(\mathbf{x}, z; \boldsymbol{\xi}, 0)$  is given by (2.3.11) or (2.3.13).

We substitute (2.3.2) into (2.3.1) to obtain the total potential and assume that the field points  $(\mathbf{x}, z)$  are taken only at the wetted surface of the plate and thus  $z = 0$

$$\phi(\mathbf{x}) = \phi^{In}(\mathbf{x}) + \int_{\Delta} G(\mathbf{x}; \boldsymbol{\xi}) \{ \alpha \phi(\boldsymbol{\xi}) + i\sqrt{\alpha} w(\boldsymbol{\xi}) \} d\boldsymbol{\xi}, \quad (2.3.3)$$

where we have dropped term  $z, \zeta = 0$  from the equation and the area integration now depends on  $\xi$  and  $\eta$ . We refer to equation (2.3.3) as the potential equation for the plate. We now have a complete system of equations to be solved for  $w(\mathbf{x})$  and  $\phi(\mathbf{x})$ . Both equations (2.2.19) and (2.3.3) will be solved numerically. For (2.3.3) we need the free-surface Green's function and this will be explained in the next subsection.

### 2.3.2 The Free-surface Green's function for water of finite and infinite depth

The standard method to solve the boundary value problem described by Laplace equation (2.2.12), surface boundary condition (2.2.13), bottom boundary condition (2.2.15), and radiation condition [Sarpkaya & Isaacson, 1981] is to use a Green's function. Therefore the Green's function satisfies

$$\left. \begin{aligned} \nabla^2 G(\mathbf{x}, z; \xi, \zeta) &= \delta(\mathbf{x} - \xi) \delta(z - \zeta), & (\mathbf{x}, z), (\xi, \zeta) \in \Omega \\ \frac{\partial G}{\partial z} &= \alpha G, & z = 0, \\ \frac{\partial G}{\partial \zeta} &= 0, & z = -H, \\ \lim_{|\mathbf{x}| \rightarrow \infty} \sqrt{|\mathbf{x}|} \left( \frac{\partial}{\partial |\mathbf{x}|} - ik \right) G &= 0, \end{aligned} \right\} \quad (2.3.4)$$

where  $\mathbf{x} = (x, y)$  is the field point and  $\xi = (\xi, \eta)$  is the source point. We call such Green's function a *free-surface Green's function (for water of either finite or infinite depth)*.

For water of finite depth various solutions to (2.3.4) are given by various authors Sarpkaya and Isaacson [Sarpkaya & Isaacson, 1981], Mei [Mei, 1989], and Linton [Linton, 1999]. Mei and Sarpkaya and Isaacson gave the following expression for the free-surface Green's function for water of finite depth

$$\begin{aligned} G(\mathbf{x}, z; \xi, \zeta) &= -\frac{1}{4\pi} \left\{ \frac{1}{\sqrt{|\mathbf{x} - \xi|^2 + (z - \zeta)^2}} + \frac{1}{\sqrt{|\mathbf{x} - \xi|^2 + (z + 2H + \zeta)^2}} \right. \\ &\quad \left. + 2 \int_0^\infty \frac{(k + \alpha) e^{-kH} J_0(k|\mathbf{x} - \xi|)}{k \sinh(kH) - \alpha \cosh(kH)} \cosh k(z + H) \cosh k(\zeta + H) dk \right\}, \end{aligned} \quad (2.3.5)$$

where  $k$  is the wavenumber.

$$\alpha = k \tanh(kH), \quad (2.3.6)$$

$\alpha$  is the frequency square given in (2.2.20), and  $J_0$  is the first kind Bessel function of order zero ([Sarpkaya & Isaacson, 1981] and [Mei, 1989]). Linton gave a series representation of (2.3.5)

$$G(\mathbf{x}, z; \boldsymbol{\xi}, \zeta) = - \sum_{j=0}^{\infty} \frac{K_0(k_j |\mathbf{x} - \boldsymbol{\xi}|)}{2\pi C_j} \cos k_j(z + H) \cos k_j(\zeta + H), \quad (2.3.7)$$

where  $\alpha_0$  is the second kind modified Bessel function of order 0 and  $k_j$  are the positive real roots of the dispersion equation

$$-k_j \tan k_j H = \alpha \quad j \geq 0. \quad (2.3.8)$$

The zeroth root  $k_0$  is related to the wavenumber  $k$  by

$$k_0 = -ik. \quad (2.3.9)$$

The constant  $C_j$  is

$$C_j = \frac{H}{2} \left( 1 + \frac{\sin 2k_j H}{2k_j H} \right). \quad (2.3.10)$$

[Linton, 1999]. Following (2.3.3), where the boundary integral equation is taken over the surface, we set  $z = 0$  and  $\zeta = 0$  in (2.3.7) to get

$$G(\mathbf{x}; \boldsymbol{\xi}) = - \sum_{j=1}^{\infty} \frac{K_0(k_j |\mathbf{x} - \boldsymbol{\xi}|)}{2\pi C_j} \cos^2 k_j(H). \quad (2.3.11)$$

For infinitely deep water the solution of (2.3.4) is given by Wehausen and Laitone [Wehausen & Laitone, 1960]. Such Green's function has the form

$$G(\mathbf{x}, z; \boldsymbol{\xi}, \zeta) = -\frac{1}{4\pi} \left\{ \frac{1}{\sqrt{|\mathbf{x} - \boldsymbol{\xi}|^2 + (z - \zeta)^2}} + \frac{1}{\sqrt{|\mathbf{x} - \boldsymbol{\xi}|^2 + (z + \zeta)^2}} - (\alpha e^{\alpha(z+\zeta)} \pi) \times \right. \\ \left. \left[ \mathbf{H}_0(\alpha |\mathbf{x} - \boldsymbol{\xi}|) + Y_0(\alpha |\mathbf{x} - \boldsymbol{\xi}|) - 2 \int_0^{-\alpha(z+\zeta)} \frac{e^s ds}{\sqrt{\alpha^2 |\mathbf{x} - \boldsymbol{\xi}|^2 + s^2}} \right] \right. \\ \left. + 2\pi i \alpha J_0(\alpha |\mathbf{x} - \boldsymbol{\xi}|) \right\}, \quad (2.3.12)$$

where  $\mathbf{H}_0$  is the Struve function of order zero,  $Y_0$  is the second kind Bessel function of order zero, and  $J_0$  is the first kind Bessel function of order zero. As in the case when the

water depth was finite we also substitute  $z = \zeta = 0$  in (2.3.12) to obtain an expression that will be used by (2.3.3)

$$G(\mathbf{x}; \boldsymbol{\xi}) = \frac{1}{4\pi} \left( \frac{2}{|\mathbf{x} - \boldsymbol{\xi}|} - \pi\alpha [\mathbf{H}_0(\alpha |\mathbf{x} - \boldsymbol{\xi}|) + Y_0(\alpha |\mathbf{x} - \boldsymbol{\xi}|) - 2i J_0(\alpha |\mathbf{x} - \boldsymbol{\xi}|)] \right). \quad (2.3.13)$$

In the next two chapters we will present two numerical schemes to solve (2.2.19) and (2.3.3). Based on this mathematical model in the next two chapters we will present a numerical scheme based on the Finite Element and the Boundary Element Methods to solve the displacement of the plate and the potential of the water.

# Chapter 3

## Solving the Motion of the Plate and the Water

In this chapter we present the method for solving the coupled motion of water and plate. First we solve the displacement of the plate. In the first section we show the discretization of the plate by square plates. In the second section we expand the displacement in terms of the FEM basis functions. In the third section we apply this expansion on the variational equation of the coupled Bernoulli-Euler's equation for a thin plate and the dynamic boundary condition on the interface with water. We refer to this as the direct method.

Next we solve the boundary integral equation for the potential where a free-surface Green's function is involved. There are two approaches to solve the integral equation; the first one is to use the constant panel method which is used by Meylan and the second one is to use the combination of the FEM basis functions and an elementary numerical integration scheme. In the fourth section we show the constant panel method used by Meylan. This yields a matrix containing the Green's function taken at the centre of the panels. Finally Meylan's method to couple the water and the plate is shown. In the fifth section we present a higher order method to solve the plate-water motion directly [Wang & Meylan, 2004]. This simply uses the basis functions of the FEM. This yields a new matrix containing the Green's integral operator acting on the basis functions which cannot be solve analytically. The solution of this integral operations is presented in the fourth section using Gaussian quadrature.

### 3.1 Discretization of the Plate

In this section we discretize the plate of arbitrary geometry using a finite number of rectangular panels. For now we regard the panel as rectangular and later in next chapter we shall use square panels instead of a rectangular ones.

The discretization process is depicted in Figure 3.1.1. The plate of arbitrary geometry  $\Delta$  is discretized by rectangular panels. We note that this discretization only approximates  $\Delta$  in general. However if the plate is rectangular the discretization by rectangular panels cover it exactly. In any plate the discretization yields  $p$  total number of rectangular panels and  $q$  total number of nodes (corners of each panel).

Each panel is of area  $4ab$  and is denoted by  $\Delta_d$  ( $1 < d < p$ ). We number the panels in the following way. We start from the bottom most left one, traverse upwards until the last panel in the column, and then we move to the column on the right. We do this until we meet the top right most panel in the plate. The corners of each panel are numbered locally by  $q_1^{(d)}$ ,  $q_2^{(d)}$ ,  $q_3^{(d)}$ , and  $q_4^{(d)}$ .

## 3.2 The Expansion of the Plate's displacement

In this section we present the solution of the plate displacement using the Finite Element Method. We solve the displacement  $w(x, y)$  locally over a panel  $e$  where  $(x, y) \in \Delta_e$ . We do this by expanding it as the sum of FEM basis functions taken at its nodes. Having done this we obtain an equation describing the displacement for a panel

$$w(x, y) = \mathbf{N}_d(x, y) \hat{\mathbf{w}}_d, \quad (3.2.1)$$

where  $\mathbf{N}_d$  is the vector of the basis functions of the Finite Element Method (subsequently we shall refer this vector as *basis vector*). It is defined as following

$$\mathbf{N}_d(\mathbf{x}) = [ N_{11} \ N_{12} \ N_{13} \ N_{21} \ N_{22} \ N_{23} \ N_{31} \ N_{32} \ N_{33} \ N_{41} \ N_{42} \ N_{43} ] \quad (3.2.2)$$

where  $N_{j1}(\hat{x}, \hat{y})$ ,  $N_{j2}(\hat{x}, \hat{y})$ , and  $N_{j3}(\hat{x}, \hat{y})$  ( $j = 1, 2, 3, 4$ ) are given by

$$\left. \begin{aligned} N_{j1}(\hat{x}, \hat{y}) &= \frac{1}{8} (1 + \hat{x}_j \hat{x}) (1 + \hat{y}_j \hat{y}) (2 + \hat{x}_j \hat{x} + \hat{y}_j \hat{y} - \hat{x}^2 - \hat{y}^2), \\ N_{j2}(\hat{x}, \hat{y}) &= \frac{b}{16} (1 + \hat{x}_j \hat{x}) (\hat{y}_j + \hat{y}) (\hat{y}^2 - 1), \\ N_{j3}(\hat{x}, \hat{y}) &= -\frac{a}{16} (\hat{x}_j + \hat{x}) (\hat{x}^2 - 1) (1 + \hat{y}_j \hat{y}). \end{aligned} \right\} \quad (3.2.3)$$

$(\hat{x}, \hat{y})$  is  $(x/a, y/b)$  in  $\Delta_d$ . The basis vector  $\mathbf{N}_d$  is of dimension  $1 \times 12$ . We only consider square panels by letting  $b = a$ . Vector  $\hat{\mathbf{w}}_d$  is an array of unknown *constants* of the form

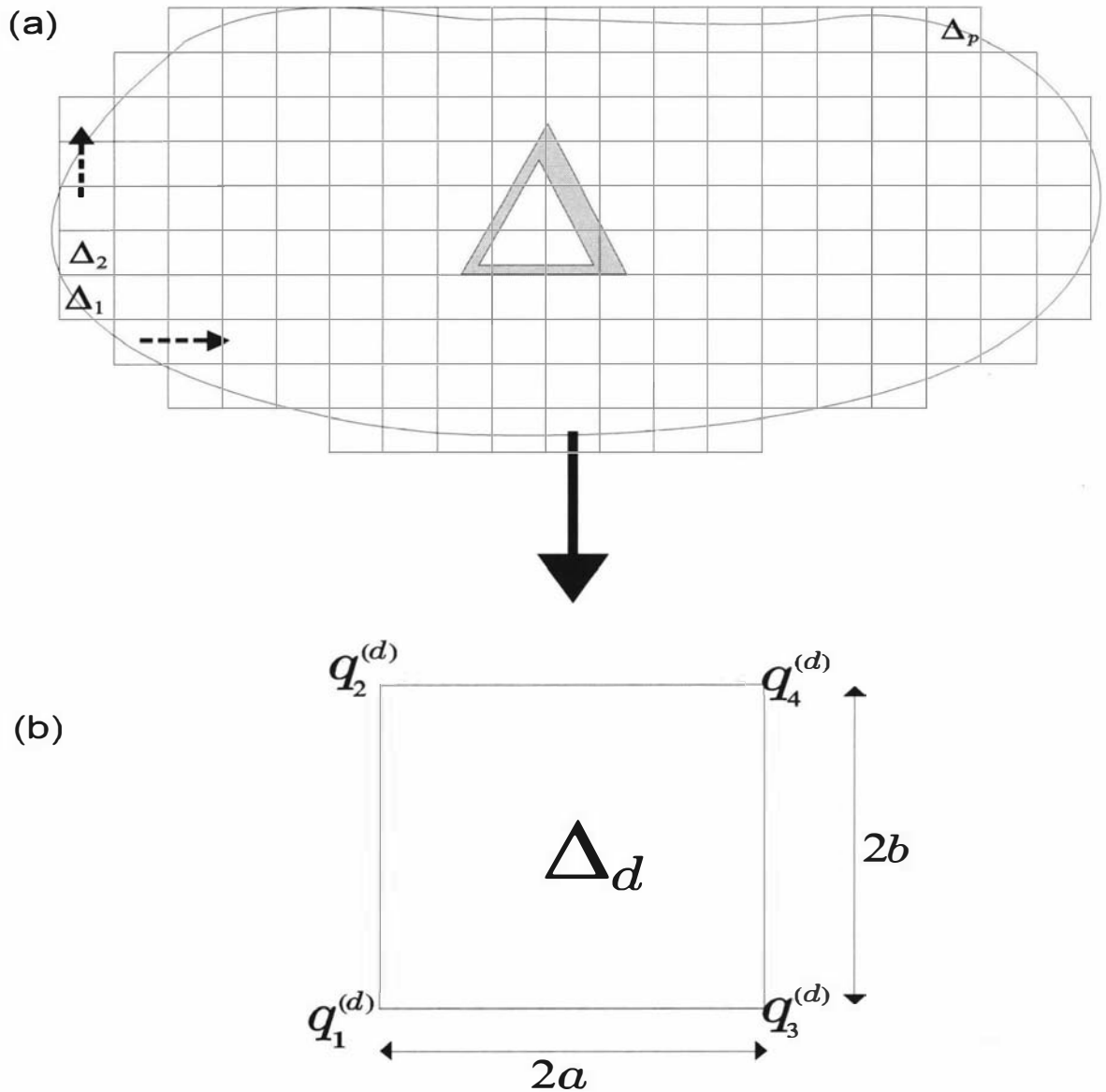


Figure 3.1.1. The discretisation of a plate of arbitrary geometry by rectangular panels. (a) The plate is covered by  $p$  total number of panels where each panel is denoted by  $\Delta_d$  and numbering of  $d = 1, \dots, p$  is directed by the arrows. (b) Each rectangular panel is of area  $4ab$  and its corners are numbered locally by  $q_j^{(d)}$  ( $j = 1, 2, 3, 4$ ). In total a plate has  $q$  nodes which are the corners of the rectangular panels.

$$\hat{\mathbf{w}}_d = \begin{bmatrix} w_{1,d} \\ \frac{\partial w_{1,d}}{\partial x} \\ \frac{\partial w_{1,d}}{\partial y} \\ w_{2,d} \\ \frac{\partial w_{2,d}}{\partial x} \\ \frac{\partial w_{2,d}}{\partial y} \\ w_{3,d} \\ \frac{\partial w_{3,d}}{\partial x} \\ \frac{\partial w_{3,d}}{\partial y} \\ w_{4,d} \\ \frac{\partial w_{4,d}}{\partial x} \\ \frac{\partial w_{4,d}}{\partial y} \end{bmatrix}, \quad (3.2.4)$$

with the elements given by

$$\begin{aligned} w_{j,d} &= w(\mathbf{x}_j^{(d)}), \\ \frac{\partial w_{j,d}}{\partial x} &= \frac{\partial}{\partial x} w(\mathbf{x}_j^{(d)}), \\ \frac{\partial w_{j,d}}{\partial y} &= \frac{\partial}{\partial y} w(\mathbf{x}_j^{(d)}), \end{aligned}$$

where  $\mathbf{x}_j^{(d)}$  is the  $(x, y)$  coordinate of node  $q_j^{(d)}$  and the constant vector  $\hat{\mathbf{w}}_d$  has dimension  $12 \times 1$ .

For any arbitrary  $\Delta_d$  the displacement vector  $\hat{\mathbf{w}}_d$  of the panel is related to the unknown displacement vector  $\hat{\mathbf{w}}$  for the plate by the nodal equation

$$\hat{\mathbf{w}}_d = [o]_d \hat{\mathbf{w}}, \quad (3.2.5)$$



### 3.3.1 The variational form of the displacement equation

In order to obtain the equivalent linear matrix-vector equation to the coupled equation we need to transform the coupled pressure equation (2.2.19) into its variational form by multiplying it with  $\delta w$  and integrating it by parts [Hildebrand, 1965] to obtain [Meylan, 2001]

$$\begin{aligned} & \delta \int_{\Delta} \left\{ \frac{1}{2} \beta \left[ \left( \frac{\partial^2 w}{\partial x^2} \right)^2 + 2\nu \frac{\partial^2 w}{\partial x^2} \frac{\partial^2 w}{\partial y^2} + 2(1-\nu) \left( \frac{\partial^2 w}{\partial x \partial y} \right)^2 + \left( \frac{\partial^2 w}{\partial y^2} \right)^2 \right] \right. \\ & \quad \left. + (1-\alpha\gamma) w^2 \right\} d\mathbf{x} \\ & = i\sqrt{\alpha}\delta \int_{\Delta} \phi w d\mathbf{x}. \end{aligned} \tag{3.3.1}$$

Equation (3.3.1) has to be minimized so that we can obtain the necessary matrices and the vectors. In the next subsection the variational equation (3.3.1) is discretized from the plate  $\Delta$  into panels  $\Delta_d$ . The discretized version is then minimized over the basis in (3.2.1).

### 3.3.2 Minimization of the Discretized Variational Equation

Following the discretization of the plate  $\Delta$  into panels  $\Delta_d$  we write the area integral term in the the variational equation (3.3.1) into the sum of integrals over the panels

$$\begin{aligned} & \delta \sum_{d=1}^p \int_{\Delta_d} \left\{ \frac{1}{2} \beta \left[ \left( \frac{\partial^2 w}{\partial x^2} \right)^2 + 2\nu \frac{\partial^2 w}{\partial x^2} \frac{\partial^2 w}{\partial y^2} + 2(1-\nu) \left( \frac{\partial^2 w}{\partial x \partial y} \right)^2 + \left( \frac{\partial^2 w}{\partial y^2} \right)^2 \right] \right. \\ & \quad \left. + (1-\alpha\gamma) w^2 \right\} d\mathbf{x} \\ & = i\sqrt{\alpha}\delta \sum_{d=1}^p \int_{\Delta_d} \phi w d\mathbf{x}, \end{aligned}$$

and into this we substitute in (3.2.7)

$$\begin{aligned}
& \delta \left[ \sum_{d=1}^p \int_{\Delta_d} \left\{ \left[ \frac{1}{2} \beta \left( \frac{\partial^2 \mathbf{N}_d(\mathbf{x})}{\partial x^2} [o]_d \hat{\mathbf{w}} \right)^2 + 2\nu \left( \frac{\partial^2 \mathbf{N}_d(\mathbf{x})}{\partial x^2} [o]_d \hat{\mathbf{w}} \right) \left( \frac{\partial^2 \mathbf{N}_d(\mathbf{x})}{\partial y^2} [o]_d \hat{\mathbf{w}} \right) \right. \right. \\
& \quad \left. \left. + 2(1-\nu) \left( \frac{\partial^2 \mathbf{N}_d(\mathbf{x})}{\partial x \partial y} [o]_d \hat{\mathbf{w}} \right)^2 + \left( \frac{\partial^2 \mathbf{N}_d(\mathbf{x})}{\partial y^2} [o]_d \hat{\mathbf{w}} \right)^2 \right] \right. \\
& \quad \left. + (1-\alpha\gamma) (\mathbf{N}_d(\mathbf{x}) [o]_d \hat{\mathbf{w}})^2 \right\} d\mathbf{x} \Big] \\
& = i\sqrt{\alpha}\delta \left[ \sum_{d=1}^p \int_{\Delta_d} \phi(\mathbf{x}) \mathbf{N}_d(\mathbf{x}) [o]_d \hat{\mathbf{w}} d\mathbf{x} \right]. \tag{3.3.2}
\end{aligned}$$

Notice that  $[o]_d \hat{\mathbf{w}}$  is independent of  $x$  and  $y$ , and only  $\mathbf{N}_d$  depends on  $x$  and  $y$ . Therefore the derivative operator only applies to  $\mathbf{N}_d$ . We then minimize it with respect to  $\hat{\mathbf{w}}$ . This is done by differentiating (3.3.2) with respect to  $\hat{\mathbf{w}}$ .

To differentiate (3.3.2) with respect to vector  $\hat{\mathbf{w}}$ , we first denote the product  $\mathbf{N}_d [o]_d = \mathbf{u}$  where the dimension of  $\mathbf{u}$  is  $1 \times 3q$ . Then (3.2.7) becomes

$$\begin{aligned}
w & = \mathbf{u} \hat{\mathbf{w}}, \\
& = \sum_i u_i \hat{w}_i,
\end{aligned}$$

where  $u_i$  and  $\hat{w}_i$  are the elements of, respectively,  $\mathbf{u}$  and  $\hat{\mathbf{w}}$ . As we recall from (3.2.5), the dimension of  $\hat{\mathbf{w}}$  is  $3q \times 1$ . Then we find that any differentiation with respect to vector  $\hat{\mathbf{w}}$  leads to a differential operator  $\left[ \frac{d}{d\hat{w}_i} \right]$  which simply is a vector of dimension equal to the dimension of  $\hat{\mathbf{w}}$ . Therefore differentiating scalar  $w$  with respect to vector  $\hat{\mathbf{w}}$  means that we apply the differential operator  $\left[ \frac{d}{d\hat{w}_i} \right]$  to  $w$

$$\begin{aligned}
\left[ \frac{d}{d\hat{w}_i} \right] w & = \left[ \frac{dw}{d\hat{w}_i} \right], \\
& = [u_i],
\end{aligned}$$

where the resulting vector  $[u_i]$  has dimension equal to the dimension of the differential operator, that is  $3q \times 1$ . Since vector  $\mathbf{u}$  has dimension  $1 \times 3q$  then clearly

$$\frac{dw}{d\hat{\mathbf{w}}} = \left[ \frac{dw}{d\hat{w}_i} \right] = \mathbf{u}^T, \tag{3.3.3}$$

and furthermore  $\mathbf{u}^T = (\mathbf{N}_d [o]_d)^T$ .

By applying the method for (3.3.3) to (3.3.2) we obtain

$$\begin{aligned}
& \beta \sum_{d=1}^p [o]_d^T \left\{ \int_{\Delta_d} \left[ \left( \frac{\partial^2 \mathbf{N}_d^T}{\partial x^2} \frac{\partial^2 \mathbf{N}_d}{\partial x^2} \right) + \nu \left( \frac{\partial^2 \mathbf{N}_d^T}{\partial x^2} \frac{\partial^2 \mathbf{N}_d}{\partial y^2} + \frac{\partial^2 \mathbf{N}_d^T}{\partial y^2} \frac{\partial^2 \mathbf{N}_d}{\partial x^2} \right) \right. \right. \\
& \quad \left. \left. + (1 - \nu) \left( \frac{\partial^2 \mathbf{N}_d^T}{\partial x \partial y} \frac{\partial^2 \mathbf{N}_d}{\partial x \partial y} \right) + \left( \frac{\partial^2 \mathbf{N}_d^T}{\partial y^2} \frac{\partial^2 \mathbf{N}_d}{\partial y^2} \right) \right] d\mathbf{x} \right\} \\
& \quad \left. + (1 - \alpha\gamma) \int_{\Delta_d} \mathbf{N}_d^T \mathbf{N}_d d\mathbf{x} \right\} [o]_d \hat{\mathbf{w}} \\
& = i\sqrt{\alpha} \sum_{d=1}^p [o]_d^T \int_{\Delta_d} \mathbf{N}_d^T \phi(\mathbf{x}) d\mathbf{x}. \tag{3.3.4}
\end{aligned}$$

In the notation of the FEM the first integral (within the summation over the panels) on the left hand side of the equation is called the *stiffness matrix of the panel*

$$\begin{aligned}
[k]_d & = \int_{\Delta_d} \left( \frac{\partial^2 \mathbf{N}_d^T}{\partial x^2} \frac{\partial^2 \mathbf{N}_d}{\partial x^2} \right) + \nu \left( \frac{\partial^2 \mathbf{N}_d^T}{\partial x^2} \frac{\partial^2 \mathbf{N}_d}{\partial y^2} + \frac{\partial^2 \mathbf{N}_d^T}{\partial y^2} \frac{\partial^2 \mathbf{N}_d}{\partial x^2} \right) \\
& \quad + 2(1 - \nu) \left( \frac{\partial^2 \mathbf{N}_d^T}{\partial x \partial y} \frac{\partial^2 \mathbf{N}_d}{\partial x \partial y} \right) + \left( \frac{\partial^2 \mathbf{N}_d^T}{\partial y^2} \frac{\partial^2 \mathbf{N}_d}{\partial y^2} \right) d\mathbf{x}, \tag{3.3.5}
\end{aligned}$$

and the second term on the left hand side of the equation is called the *mass matrix of the panel*

$$[m]_d = \int_{\Delta_d} \mathbf{N}_d^T \mathbf{N}_d d\mathbf{x}. \tag{3.3.6}$$

We may express (3.3.4) as a linear matrix-vector equation describing the displacement of the plate as a sum over all panels

$$\left\{ \beta \sum_{d=1}^p [o]_d^T [k]_d [o]_d + (1 - \alpha\gamma) \sum_{d=1}^p [o]_d^T [m]_d [o]_d \right\} \hat{\mathbf{w}} = i\sqrt{\alpha} \sum_{d=1}^p [o]_d^T \int_{\Delta_d} \mathbf{N}_d^T \phi(\mathbf{x}) d\mathbf{x}. \tag{3.3.7}$$

Furthermore we can write (3.3.7) simply as

$$\{\beta \mathbb{K} + (1 - \alpha\gamma) \mathbb{M}\} \hat{\mathbf{w}} = \mathbf{F}, \tag{3.3.8}$$

where matrix  $\mathbb{K}$

$$\mathbb{K} = \sum_{d=1}^p [o]_d^T [k]_d [o]_d, \tag{3.3.9}$$

is the *stiffness matrix of the plate*, matrix  $\mathbb{M}$

$$\mathbb{M} = \sum_{d=1}^p [o]_d^T [m]_d [o]_d, \tag{3.3.10}$$

is the *mass matrix of the plate*, and vector  $\mathbf{F}$

$$\mathbf{F} = i\sqrt{\alpha} \sum_{d=1}^p [o]_d^T \int_{\Delta_d} \mathbf{N}_d^T \phi(\mathbf{x}) \, d\mathbf{x}, \quad (3.3.11)$$

is the *forcing vector of the plate due to the water*. From equation (3.3.9)  $[k]_d$  is the stiffness matrix of the panel that we can write as

$$[k]_d = \int_{\Delta} [\mathbf{N}'' ]_d^T \begin{bmatrix} 1 & \nu & 0 \\ & 1 & 0 \\ \text{sym} & & \frac{1-\nu}{2} \end{bmatrix} [\mathbf{N}'' ]_d \, d\mathbf{x}, \quad (3.3.12)$$

with

$$[\mathbf{N}'' ]_d = \begin{bmatrix} \frac{\partial^2 \mathbf{N}_d}{\partial x^2} \\ \frac{\partial^2 \mathbf{N}_d}{\partial y^2} \\ 2 \frac{\partial^2 \mathbf{N}_d}{\partial x \partial y} \end{bmatrix}.$$

We notice that in equation (3.3.10)  $[m]_d$  is the mass matrix of the panel that is defined in (3.3.6).

Equation (3.3.8) is to be solved for the displacement of the plate  $\hat{\mathbf{w}}$ . Notice that both the stiffness and the mass matrices of the panel have dimension  $12 \times 12$ . Note that we purposely write the term involving the potential of the water using  $\mathbf{F}$  because we will solve this by two different ways, one was done by Meylan using the constant panel method and the other uses the basis functions of the FEM. Each of these methods will be shown in the next section.

### 3.4 Solving the Plate-Water Motion by the Constant Panel Method

In this section we describe Meylan's strategy for solving the boundary integral equation for the potential and to incorporate it into the displacement equation through the forcing vector. First we show the constant panel method that is used to solve the forcing vector

due to the water. Then we show the coupling of the water and the plate. Note that this procedure appeared in [Meylan, 1997].

### 3.4.1 Solving the Potential

The integral equation for the potential can be written as

$$\phi(\mathbf{x}) = \phi^{In}(\mathbf{x}) + \mathbf{G} \{ \alpha \phi(\mathbf{x}) + i\sqrt{\alpha} w(\mathbf{x}) \}, \quad (3.4.1)$$

where the integral  $\mathbf{G}f(\mathbf{x})$  is

$$\mathbf{G}f(\mathbf{x}) = \int_{\Delta} G(\mathbf{x}; \boldsymbol{\xi}) f(\boldsymbol{\xi}) d\boldsymbol{\xi}, \quad (3.4.2)$$

and  $f(\boldsymbol{\xi})$  is an arbitrary function. This integral equation has kernel the free-surface Green's function (2.3.11) or (2.3.13) evaluated at the surface. Equation (3.4.1) can be solved for potential  $\phi(\mathbf{x})$  by relation

$$\phi(\mathbf{x}) = (\mathbf{1} - \alpha \mathbf{G})^{-1} \{ \phi^{In}(\mathbf{x}) + i\sqrt{\alpha} \mathbf{G} w(\mathbf{x}) \}, \quad (3.4.3)$$

where  $\mathbf{1}$  is the identity operator of the same dimension as  $\mathbf{G}$  [Meylan, 2001].

Meylan used the constant panel method (also called first order basis function or piecewise constant basis function method) to integrate the area integral in the equations for the potential (2.3.3). The method approximates a function  $f(\boldsymbol{\xi})$  by its value at the centre of the panel (of the FEM) and is assumed to be constant elsewhere in the panel. Using this notion he approximate integral operator  $\mathbf{G}f$  by expanding it as a finite sum

$$\mathbf{G}f(\mathbf{x}_d) = \sum_{e=1}^p \int_{\Delta_e} G(\mathbf{x}_d; \boldsymbol{\xi}_e) d\boldsymbol{\xi} f_e, \quad d = 1, \dots, p, \quad (3.4.4)$$

where point  $\mathbf{x}_d = (x_d, y_d)$  is the centre of panel  $\Delta_d$ ,  $f_e = f(\boldsymbol{\xi}_e)$ , and  $\boldsymbol{\xi}_e = (\xi_e, \eta_e)$  is the centre of panel  $\Delta_e$ . Then Meylan approximated the area integral of  $G$  over panel  $\Delta_e$  by taking  $G$  to be the value at the centre and constant across the panels. So  $G$  is constant as well as  $\phi$  over the panels

$$\int_{\Delta_e} G(\mathbf{x}_d; \boldsymbol{\xi}_e) d\boldsymbol{\xi} = 4a^2 G(\mathbf{x}_d; \boldsymbol{\xi}_e), \quad (3.4.5)$$

where  $4a^2$  is the area of the square panel. Thus any integral equation of the form  $\mathbb{G}f(\mathbf{x}_d)$  can be written as

$$\mathbb{G}f(\mathbf{x}_d) = \sum_{e=1}^p 4a^2 G(\mathbf{x}_d; \boldsymbol{\xi}_e) f_e.$$

For all  $\Delta_d$ ,  $d = 1, \dots, p$  we have a matrix and vector multiplication  $\mathbb{G}\mathbf{f}$  where matrix  $\mathbb{G}$  is defined as

$$\mathbb{G} = 4a^2 \begin{bmatrix} G(\mathbf{x}_1; \boldsymbol{\xi}_1) & G(\mathbf{x}_1; \boldsymbol{\xi}_2) & \dots & G(\mathbf{x}_1; \boldsymbol{\xi}_p) \\ G(\mathbf{x}_2; \boldsymbol{\xi}_1) & & & G(\mathbf{x}_2; \boldsymbol{\xi}_p) \\ \vdots & & & \vdots \\ G(\mathbf{x}_p; \boldsymbol{\xi}_1) & & & G(\mathbf{x}_p; \boldsymbol{\xi}_p) \end{bmatrix}. \quad (3.4.6)$$

By the definition of the finite and the infinite depth Green's functions (2.3.7) and (2.3.13) singularity occurs whenever  $d = e$  (diagonal terms in (3.4.6)) However this obstacle can be avoided by integrating the special functions in  $G$  exactly.

Then integral equation (3.4.3) becomes

$$\boldsymbol{\phi} = (\mathbb{I} - \alpha \mathbb{G})^{-1} \{ \boldsymbol{\phi}^{In} + i\sqrt{\alpha} \mathbb{G} \mathbb{P}^\Delta \hat{\mathbf{w}} \}, \quad (3.4.7)$$

where

$$\boldsymbol{\phi} = [\phi(\mathbf{x}_d)],$$

$\mathbb{I}$  is the identity matrix of the same size as matrix  $\mathbb{G}$ , and  $\mathbb{P}^\Delta$  is the matrix that maps  $\hat{\mathbf{w}}_j$  from the corners of the panels to the centres of the panels

$$\mathbb{P}^\Delta = \frac{1}{4} \sum_{d=1}^p \mathbb{I}_{12} [o]_d, \quad (3.4.8)$$

where  $[o]_d$  is the assembler matrix (3.2.6). Matrix  $\mathbb{P}^\Delta$  is needed because the displacements  $\hat{\mathbf{w}}$  are taken at the corners of the panels but  $\boldsymbol{\phi}$ ,  $\boldsymbol{\phi}^{In}$ , and  $\mathbb{G}$  are taken at the centre of the panels.

### 3.4.2 Coupling the Water and the Plate

Before we proceed we note that Meylan did not use the term  $\mathbf{N}_d$  in his forcing vector. Instead he used another mapping matrix to combine the potential into the forcing vector. Hence we say that Meylan's forcing vector is equivalent to (but not the same as) ours.

The application of the potential (3.4.7) to the forcing vector (equivalent to (3.3.11)) gives rise to the following equation for  $\tilde{\mathbf{F}}$

$$\tilde{\mathbf{F}} = i\sqrt{\alpha} \mathbb{P}^\Omega (\mathbb{I} - \alpha \mathbb{G})^{-1} \{ \phi^{In} + i\sqrt{\alpha} \mathbb{G} \mathbb{P}^\Delta \hat{\mathbf{w}} \}, \quad (3.4.9)$$

where  $\mathbb{P}^\Omega$  is the matrix that maps the value of  $\phi$  (the bracketed terms) from the centres to the corners of the panels. This is because  $\tilde{\mathbf{F}}$  is defined at all nodes of the panels but the potential  $\phi$  is defined at the centres of the panels. Likewise  $\mathbb{P}^\Delta$  matrix  $\mathbb{P}^\Omega$  is expressed in terms of the assembler matrix (3.2.6)

$$\mathbb{P}^\Omega = 4a^2 \sum_{d=1}^p [o]_d^T \mathbb{I}_{12}. \quad (3.4.10)$$

Substituting  $\tilde{\mathbf{F}}$  (3.4.9) into (3.3.8)

$$\{ \beta \mathbb{K} + (1 - \alpha \gamma) \mathbb{M} \} \hat{\mathbf{w}} = i\sqrt{\alpha} \mathbb{P}^\Omega (\mathbb{I} - \alpha \mathbb{G})^{-1} \{ \phi^{In} + i\sqrt{\alpha} \mathbb{G} \mathbb{P}^\Delta \hat{\mathbf{w}} \}. \quad (3.4.11)$$

By collecting  $\hat{\mathbf{w}}$  on one side of (3.4.11) Meylan obtained the linear equation

$$\{ \beta \mathbb{K} + (1 - \alpha \gamma) \mathbb{M} + \alpha \mathbb{P}^\Omega (\mathbb{I} - \alpha \mathbb{G})^{-1} \mathbb{G} \mathbb{P}^\Delta \} \hat{\mathbf{w}} = i\sqrt{\alpha} \mathbb{P}^\Omega (\mathbb{I} - \alpha \mathbb{G})^{-1} \phi^{In}, \quad (3.4.12)$$

that is to be solved for constant the unknown displacement  $\hat{\mathbf{w}}$ .

Meylan ([Meylan, 1997], [Meylan, 2001], [Meylan, 2002]) has written an extensive library of codes to solve (3.4.12). Hence we will omit the discussion of his implementation method.

### 3.5 A Higher Order method to solve the Plate-water motion.

In this section we present an alternative way to solve the plate-water motion using Meylan's piecewise constants area FEM basis functions. The strategy combines the basis vector with any elementary numerical integration scheme. The proposed method estimates the integral better than the constant panel method used by Meylan. This is because, instead of taking the value of the Green's function at the centre of the panel and assuming it constant across the element, the Green's function is calculated at the specified quadrature points in the panel and, hence, the value varies across the panel. Also the number of unknowns used to

discretize the potential  $\phi$  is the same as that used to discretize the plate. Coupling these solutions yields a new matrix representation of the free-surface Green's function for the water that is equivalent to the mass and the stiffness matrix for the plate.

### 3.5.1 Solving for the Potential

Our aim now is to solve the boundary integral equation using the basis function  $\mathbf{N}_d$  (3.2.2). First we expand  $\phi(\mathbf{x})$  over a panel  $\Delta_d$  where  $\mathbf{x} \in \Delta_d$  and  $0 \leq d \leq p$ . The potential at  $\phi(\mathbf{x})$  is expressed as a product of the basis vector and a constant vector similar to (3.2.4).

$$\phi(\mathbf{x}) = \mathbf{N}_d \hat{\phi}_d, \quad \mathbf{x} \in \Delta_d \quad (3.5.1)$$

where  $\mathbf{N}_d$  is given in (3.2.2) and  $\hat{\phi}_d$  is the vector of constants defined in a similar manner to (3.2.4)

$$\hat{\phi}_d = \begin{bmatrix} \phi_{1,d} \\ \frac{\partial \phi_{1,d}}{\partial x} \\ \frac{\partial \phi_{1,d}}{\partial y} \\ \phi_{2,d} \\ \frac{\partial \phi_{2,d}}{\partial x} \\ \frac{\partial \phi_{2,d}}{\partial y} \\ \phi_{3,d} \\ \frac{\partial \phi_{3,d}}{\partial x} \\ \frac{\partial \phi_{3,d}}{\partial y} \\ \phi_{4,d} \\ \frac{\partial \phi_{4,d}}{\partial x} \\ \frac{\partial \phi_{4,d}}{\partial y} \end{bmatrix}, \quad (3.5.2)$$

and

$$\begin{aligned}\phi_{j,d} &= \phi(\mathbf{x}_j^{(d)}) \\ \frac{\partial \phi_{j,d}}{\partial x} &= \frac{\partial}{\partial x} \phi(\mathbf{x}_j^{(d)}) \\ \frac{\partial \phi_{j,d}}{\partial y} &= \frac{\partial}{\partial y} \phi(\mathbf{x}_j^{(d)}).\end{aligned}$$

The point  $\mathbf{x}_j^{(d)}$  is the coordinate of node  $q_j^{(d)}$ . Similarly  $\phi^{In}(\mathbf{x})$  can be approximated by

$$\phi^{In}(\mathbf{x}) = \mathbf{N}_d \hat{\phi}_d^{In}, \quad (3.5.3)$$

where  $\hat{\phi}_d^{In}$  is defined in the same way as (3.5.2) and  $\phi^{In}$  is the incident wave of the form (A.13). Similar to displacement vector  $\hat{\mathbf{w}}_d$  to  $\hat{\mathbf{w}}$ , the potential vector for the panel  $\hat{\phi}_d$  is related its plate counterpart  $\hat{\phi}$  and the incident potential vector  $\hat{\phi}_d^{In}$  is related to the vector  $\hat{\phi}^{In}$  by

$$\hat{\phi}_d = [o]_d \hat{\phi}, \quad (3.5.4)$$

$$\hat{\phi}_d^{In} = [o]_d \hat{\phi}^{In}. \quad (3.5.5)$$

Both  $\hat{\phi}$  and  $\hat{\phi}^{In}$  have length  $3q$ . For an arbitrary  $\mathbf{x} \in \Delta_d$  we can calculate the potential  $\phi(\mathbf{x})$  using

$$\phi(\mathbf{x}) = \mathbf{N}_d(\mathbf{x}) [o]_d \hat{\phi}, \quad (3.5.6)$$

and approximate the incident potential  $\phi^{In}(\mathbf{x})$  using

$$\phi^{In}(\mathbf{x}) \approx \mathbf{N}_d(\mathbf{x}) [o]_d \hat{\phi}^{In}. \quad (3.5.7)$$

Then we recall the following equation for the potential (2.3.3)

$$\phi(\mathbf{x}) = \phi^{In}(\mathbf{x}) + \mathbf{G} \{ \alpha \phi(\mathbf{x}) + i\sqrt{\alpha} w(\mathbf{x}) \}, \quad (3.5.8)$$

where the integral equation of the form  $\mathbf{G}f$  is given by (3.4.2)

$$\mathbf{G}f(\mathbf{x}) = \int_{\Delta} G(\mathbf{x}; \boldsymbol{\xi}) f(\boldsymbol{\xi}) d\boldsymbol{\xi}.$$

Furthermore we substitute the area integral over the plate in (3.4.2) by the sum of all area integrals over the panels  $\Delta_e$ ,  $1 \leq e \leq p$ .

$$\mathbf{G}f(\mathbf{x}) = \sum_{e=1}^p \mathbf{G}_e f(\mathbf{x}), \quad (3.5.9)$$

where the integral operator  $\mathbf{G}_e$  acting on function  $f$  is

$$\mathbf{G}_e f(\mathbf{x}) = \int_{\Delta_e} G(\mathbf{x}; \boldsymbol{\xi}) f(\boldsymbol{\xi}) d\boldsymbol{\xi},$$

and  $\boldsymbol{\xi} \in \Delta_e$ .

For  $\mathbf{x} \in \Delta_d$  we may expand (2.3.3) as

$$\mathbf{N}_d \hat{\phi}_d = \mathbf{N}_d \hat{\phi}_d^{In} + \alpha \mathbf{G} \phi(\mathbf{x}) + i\sqrt{\alpha} \mathbf{G} w(\mathbf{x}). \quad (3.5.10)$$

Using (3.5.9) equation (3.5.10) becomes

$$\mathbf{N}_d \hat{\phi}_d = \mathbf{N}_d \hat{\phi}_d^{In} + \alpha \sum_{e=1}^p \mathbf{G}_e \phi(\mathbf{x}) + i\sqrt{\alpha} \sum_{e=1}^p \mathbf{G}_e w(\mathbf{x}).$$

We further expand the term  $\mathbf{G}_e \phi(\mathbf{x})$  and  $\mathbf{G}_e w(\mathbf{x})$  by writing  $\phi(\boldsymbol{\xi}) = \mathbf{N}_e \hat{\phi}_e$  (using equation (3.5.1)) and  $w(\boldsymbol{\xi}) = \mathbf{N}_e \hat{w}_e$  (using equation (3.5.3)), where  $\boldsymbol{\xi} \in \Delta_e$  and  $\mathbf{N}_e$  is the basis vector (3.2.2). We obtain

$$\mathbf{N}_d \hat{\phi}_d = \mathbf{N}_d \hat{\phi}_d^{In} + \alpha \sum_{e=1}^p (\mathbf{G}_{de} \mathbf{N}_e) \hat{\phi}_e + i\sqrt{\alpha} \sum_{e=1}^p (\mathbf{G}_{de} \mathbf{N}_e) \hat{w}_e, \quad (3.5.11)$$

where the integral equation  $\mathbf{G}_{de} \mathbf{N}_e$  is defined as

$$\mathbf{G}_{de} \mathbf{N}_e(\mathbf{x}) = \int_{\Delta_e} G(\mathbf{x}; \boldsymbol{\xi}) \mathbf{N}_e(\boldsymbol{\xi}) d\boldsymbol{\xi}_e, \quad (3.5.12)$$

with  $\mathbf{x} \in \Delta_d$  and  $\boldsymbol{\xi} \in \Delta_e$ . We call  $\Delta_d$  the *field panel* and  $\Delta_e$  the *source panel*.

Next we introduce the notion of inner product that will be used to solve (3.5.11). We define an inner product between vector functions  $\mathbf{f}(\mathbf{x})$  and  $\mathbf{g}(\mathbf{x})$ , where  $\mathbf{x} \in \Delta_d$ , to be

$$\langle \mathbf{f}, \mathbf{g} \rangle_d = \int_{\Delta_d} \mathbf{f}^T(\mathbf{x}) \mathbf{g}(\mathbf{x}) d\mathbf{x}_d,$$

where  $T$  denotes the transpose. Thus if we take the inner product of (3.5.11) with  $\mathbf{N}_d(\mathbf{x})$  we obtain

$$\langle \mathbf{N}_d, \mathbf{N}_d \rangle_d \hat{\phi}_d = \langle \mathbf{N}_d, \mathbf{N}_d \rangle_d \hat{\phi}_d^{In} + \alpha \sum_{e=1}^p \langle \mathbf{N}_d, (\mathbf{G}_{de} \mathbf{N}_e) \rangle_d \hat{\phi}_e + i\sqrt{\alpha} \sum_{e=1}^p \langle \mathbf{N}_d, (\mathbf{G}_{de} \mathbf{N}_e) \rangle_d \hat{w}_e. \quad (3.5.13)$$

We notice that

$$\begin{aligned}\langle \mathbf{N}_d, \mathbf{N}_d \rangle_d &= \int_{\Delta_d} \mathbf{N}_d^T(\mathbf{x}) \mathbf{N}_d(\mathbf{x}) d\mathbf{x}_d \\ &= [m]_d.\end{aligned}$$

Following this we present a similar matrix for  $\langle \mathbf{N}_d, (\mathbf{G}_{de} \mathbf{N}_e) \rangle$ . We call this matrix *the Green's matrix* and it is defined in the following way.

$$[g]_{de} = \langle \mathbf{N}_d, (\mathbf{G}_{de} \mathbf{N}_e) \rangle_d \quad (3.5.14)$$

where  $\mathbf{G}_{de}$  is either (2.3.7) or (2.3.13). Substituting (3.3.6) and (3.5.14) into (3.5.13) gives us the matrix representation of the boundary integral equation for the potential over a panel

$$[m]_d \hat{\phi}_d = [m]_d \hat{\phi}_d^{In} + \alpha \sum_{e=1}^p [g]_{de} \hat{\phi}_e + i\sqrt{\alpha} \sum_{e=1}^p [g]_{de} \hat{\mathbf{w}}_e. \quad (3.5.15)$$

Finally we assemble the Green's matrix for a panel  $[g]_{de}$  into the Green's matrix for the entire plate by substituting into (3.5.14)  $\hat{\mathbf{w}}_e$ ,  $\hat{\phi}_e$ , and  $\hat{\phi}_d^{In}$  (these relationships are defined in (3.5.5), (3.5.4), and (3.2.5)).

$$[m]_d [o]_d \hat{\phi} = [m]_d [o]_d \hat{\phi}^{In} + \alpha \sum_{e=1}^p [g]_{de} [o]_e \hat{\phi} + i\sqrt{\alpha} \sum_{e=1}^p [g]_{de} [o]_e \hat{\mathbf{w}}.$$

Multiplying both sides by  $[o]_d^T$  then taking the sum over all  $d$  ( $1 \leq d \leq p$ ) gives us

$$\begin{aligned}\sum_{d=1}^p [o]_d^T [m]_d [o]_d \hat{\phi} &= \sum_{d=1}^p [o]_d^T [m]_d [o]_d \hat{\phi}^{In} + \alpha \sum_{d=1}^p [o]_d^T \sum_{e=1}^p [g]_{de} [o]_e \hat{\phi} \\ &\quad + i\sqrt{\alpha} \sum_{d=1}^p [o]_d^T \sum_{e=1}^p [g]_{de} [o]_e \hat{\mathbf{w}}.\end{aligned} \quad (3.5.16)$$

The terms involving  $[m]_d$  are recognized to be the mass matrix of the plate. We give similar definitions for all the terms involving  $[g]_{de}$  and write (3.5.16) as

$$\mathbf{M} \hat{\phi} = \mathbf{M} \hat{\phi}^{In} + \alpha \mathbf{G} \hat{\phi} + i\sqrt{\alpha} \mathbf{G} \hat{\mathbf{w}}, \quad (3.5.17)$$

where

$$\mathbf{G} = \sum_{d=1}^p [o]_d^T \sum_{e=1}^p [g]_{de} [o]_e, \quad (3.5.18)$$

is the Green's matrix for the plate.

### 3.5.2 Coupling the Plate and the Water

Assuming that  $\mathbf{x}$  is enclosed by panel  $\Delta_d$  we can substitute equation (3.5.1) into the forcing vector (3.3.7) (this is right hand side of (3.3.8)) to give us

$$\begin{aligned} \mathbf{F} &= i\sqrt{\alpha} \sum_{d=1}^p [o]_d^T [m]_d [o]_d \hat{\phi}, \\ &= \mathbf{M} \hat{\phi}. \end{aligned}$$

We substitute  $\mathbf{F}$  into the displacement equation (3.3.8)

$$\{\beta \mathbf{K} + (1 - \alpha\gamma) \mathbf{M}\} \hat{\mathbf{w}} = i\sqrt{\alpha} \mathbf{M} \hat{\phi}. \quad (3.5.19)$$

Together with the plate displacement equation (3.5.19) we have two equations which we solve simultaneously for either the displacement  $\hat{\mathbf{w}}$  or the potential  $\hat{\phi}$ . To solve for  $\hat{\mathbf{w}}$  we write (3.5.17) as

$$\hat{\phi} = (\mathbf{M} - \alpha\mathbf{G})^{-1} \left\{ \mathbf{M} \hat{\phi}^{In} + i\sqrt{\alpha}\mathbf{G} \hat{\mathbf{w}} \right\}. \quad (3.5.20)$$

so that we can substitute this into (3.3.8). This gives us the linear equation

$$\{\beta \mathbf{K} + (1 - \alpha\gamma) \mathbf{M} + \alpha\mathbf{M} (\mathbf{M} - \alpha\mathbf{G})^{-1} \mathbf{G}\} \hat{\mathbf{w}} = i\sqrt{\alpha} \mathbf{M} (\mathbf{M} - \alpha\mathbf{G})^{-1} \mathbf{M} \hat{\phi}^{In}, \quad (3.5.21)$$

which is solvable for  $\hat{\mathbf{w}}$ . To obtain the potential  $\hat{\phi}$  we only need to substitute  $\hat{\mathbf{w}}$  into (3.5.20).

Note that equation (3.5.21) is equivalent to Meylan's equation (3.4.12)

$$\{\beta \mathbf{K} + (1 - \alpha\gamma) \mathbf{M} + \alpha\mathbf{P}^\Omega (\mathbf{I} - \alpha\mathbf{G})^{-1} \mathbf{G} \mathbf{P}^\Delta\} \hat{\mathbf{w}} = i\sqrt{\alpha} \mathbf{P}^\Omega (\mathbf{I} - \alpha\mathbf{G})^{-1} \phi^{In}.$$

Similarly to solve for  $\hat{\phi}$  we write (3.3.8) as

$$\hat{\mathbf{w}} = i\sqrt{\alpha} (\beta \mathbf{K} + (1 - \alpha\gamma) \mathbf{M})^{-1} \mathbf{M} \hat{\phi}. \quad (3.5.22)$$

We then substitute (3.5.22) into (3.5.17) to obtain the following linear equation

$$(\mathbf{M} - \alpha\mathbf{G} + \alpha\mathbf{G} (\beta \mathbf{K} + (1 - \alpha\gamma) \mathbf{M})^{-1} \mathbf{M}) \hat{\phi} = \mathbf{M} \hat{\phi}^{In}. \quad (3.5.23)$$

### 3.5.3 Numerical Scheme to Solve the Green's Integral Equation

The integral equation (3.5.12) and the inner product (3.5.14) will be solved numerically using Gaussian quadrature to approximate integrals.

We approximate the integral in (3.5.12) using the sum in the following form

$$\begin{aligned} \mathbf{G}_{de} \mathbf{N}_e(\mathbf{x}) &= \int_{\Delta_e} G(\mathbf{x}; \boldsymbol{\xi}) \mathbf{N}_e(\boldsymbol{\xi}) d\boldsymbol{\xi} \\ &= \sum_{j=1}^P v_j G(\mathbf{x}; \boldsymbol{\xi}_j) \mathbf{N}_{e,j}, \end{aligned} \quad (3.5.24)$$

where  $\mathbf{N}_{e,j} = \mathbf{N}_e(\boldsymbol{\xi}_j)$ , sets  $\{\boldsymbol{\xi}_j\}$  and  $\{v_j\}$  are, respectively, the sets of  $Q$  integration points over  $\Delta_e$  and their corresponding weights. Similarly the inner product (3.5.14) is calculated using

$$\begin{aligned} [g]_{de} &= \int_{\Delta_d} \mathbf{N}_d(\mathbf{x}) (\mathbf{G}_{de} \mathbf{N}_e) dS_x \\ &= \sum_{i=1}^Q u_i \mathbf{N}_{d,i} \mathbf{G}_{de} \mathbf{N}_e(\mathbf{x}_i), \end{aligned} \quad (3.5.25)$$

where  $\mathbf{N}_{d,i} = \mathbf{N}_d(\mathbf{x}_i)$ ,  $\{\mathbf{x}_i\}$  and  $\{u_i\}$  are sets of  $P$  integration points over  $\Delta_d$  and their corresponding weights. Substituting (3.5.24) into (3.5.25) gives us

$$[g]_{de} = \sum_{i=1}^Q u_i \mathbf{N}_{d,i} \sum_{j=1}^P v_j G_{ij} \mathbf{N}_{e,j}, \quad (3.5.26)$$

where  $G_{ij} = G(\mathbf{x}_i, \boldsymbol{\xi}_j)$ ,  $\mathbf{x}_i \in \Delta_d$ , and  $\boldsymbol{\xi}_j \in \Delta_e$ .

For the case where  $|\mathbf{x} - \boldsymbol{\xi}| = 0$  we have to solve equation (3.5.26) using sets of distinct integration points  $\{\mathbf{x}_i\}$  and  $\{\boldsymbol{\xi}_j\}$  and, hence, distinct  $\{u_i\}$  and  $\{v_j\}$ . This is done to avoid the singularity that occurs whenever  $\mathbf{x}_i$  coincides with  $\boldsymbol{\xi}_j$ . For the case where  $d \neq e$  we employ the same set of integration points and their corresponding weights for (3.5.26).

We summarize the cases of (3.5.26) in vector notation

$$[g]_{de} = \begin{cases} \mathbf{N}_1 \mathbb{G}_1 \mathbf{N}_2, & \text{if } d = e, \\ \mathbf{N}_1 \mathbb{G}_2 \mathbf{N}_1^T, & \text{if } d \neq e, \end{cases} \quad (3.5.27)$$

where  $\mathbb{G}_1$  is a  $Q \times P$  rectangular matrix of the form

$$\mathbb{G}_1 = \begin{bmatrix} G_{11} & G_{12} & \cdot & \cdot & \cdot & G_{1P} \\ G_{21} & G_{22} & & & & \\ & & \cdot & & & \\ & & & \cdot & & \\ & & & & \cdot & \\ G_{Q1} & & & & & G_{QP} \end{bmatrix}, \quad (3.5.28)$$

and  $\mathbb{G}_2$  is a  $Q \times Q$  square matrix of the form

$$\mathbb{G}_2 = \begin{bmatrix} G_{11} & G_{12} & \cdot & \cdot & \cdot & G_{1Q} \\ G_{21} & G_{22} & & & & \\ & & \cdot & & & \\ & & & \cdot & & \\ & & & & \cdot & \\ G_{Q1} & & & & & G_{QQ} \end{bmatrix}. \quad (3.5.29)$$

The matrix  $\mathbb{N}_1$  is a  $12 \times Q$  matrix of the form

$$\mathbb{N}_1 = [ u_1 \mathbf{N}_{d,1}^T \quad u_2 \mathbf{N}_{d,2}^T \quad \dots \quad u_N \mathbf{N}_{d,Q}^T ], \quad (3.5.30)$$

and the matrix  $\mathbb{N}_2$  is a  $P \times 12$  matrix of the form

$$\mathbb{N}_2 = \begin{bmatrix} v_1 \mathbf{N}_{e,1} \\ v_2 \mathbf{N}_{e,2} \\ \cdot \\ \cdot \\ \cdot \\ v_3 \mathbf{N}_{e,P} \end{bmatrix}, \quad (3.5.31)$$

where vector  $\mathbf{N}_d$  are defined in (3.2.2).

Upon solving the Green's matrix for the panel (3.5.27) we can obtain the Green's matrix for the plate by substituting it into (3.5.18). Unlike Meylan's method we apply the Green's matrix  $\mathbb{G}$  directly to the potential equation (3.5.17) without the help of any transformation matrix.

# Chapter 4

## Numerical Implementation and Results of the Higher Order Method

In this chapter we implement the methodology and the matrices of the higher order method. We omit the implementation of Meylan's method because this has been done and results have been presented in [Meylan, 2002]. The first section of this chapter is a recap of the standard FEM matrices that we use. The second section contains an extensive explanation on how we implement the Green's matrix. The third section contains the comparisons with Meylan's results, convergence tests, and results for the displacement.

### 4.1 Implementing the Mass and the Stiffness Matrices

In this section we implement the matrices of the FEM given in Chapter 2. We build the plate's mass matrix  $\mathbb{M}$  and stiffness matrix  $\mathbb{K}$  from the local mass and stiffness matrices (3.3.6) and (3.3.5) that represent the mass and the stiffness of a panel. Both matrices are constants and can be found in Petyt [Petyt, 1990]. However, due to the difference in the numbering of the nodes, we define a slightly different set of matrices.

The mass matrix for panel  $\Delta_d$ ,  $[m]_d$  is

$$[m]_d = \frac{ab}{6300} \begin{bmatrix} m_{11} & m_{12} & m_{13} & m_{14} \\ m_{21} & m_{22} & m_{23} & m_{24} \\ m_{31} & m_{32} & m_{33} & m_{34} \\ m_{41} & m_{42} & m_{43} & m_{44} \end{bmatrix}, \quad (4.1.1)$$

where the diagonal submatrices are

$$\begin{aligned}
 m_{11} &= \begin{bmatrix} 3454 & & Sym \\ \frac{922}{2}b & \frac{320}{4}b^2 & \\ -\frac{922}{2}a & -\frac{252}{4}ab & \frac{320}{4}a^2 \end{bmatrix}, & m_{22} &= \begin{bmatrix} 3454 & & Sym \\ -\frac{922}{2}b & \frac{320}{4}b^2 & \\ -\frac{922}{2}a & \frac{252}{4}ab & \frac{320}{4}a^2 \end{bmatrix}, \\
 m_{33} &= \begin{bmatrix} 3454 & & Sym \\ \frac{922}{2}b & \frac{320}{4}b^2 & \\ \frac{922}{2}a & \frac{252}{4}ab & \frac{320}{4}a^2 \end{bmatrix}, & m_{44} &= \begin{bmatrix} 3454 & & Sym \\ -\frac{922}{2}b & \frac{320}{4}b^2 & \\ \frac{922}{2}a & -\frac{252}{4}ab & \frac{320}{4}a^2 \end{bmatrix},
 \end{aligned}$$

and the symbol *sym* indicates that the matrix is symmetric about the diagonal term. The sub-diagonal submatrices are

$$\begin{aligned}
 m_{21} &= \begin{bmatrix} 1226 & \frac{548}{2}b & -\frac{398}{2}a \\ -\frac{548}{2}b & -\frac{240}{4}b^2 & \frac{168}{4}ab \\ -\frac{398}{2}a & -\frac{168}{4}ab & \frac{160}{4}a^2 \end{bmatrix}, & m_{31} &= \begin{bmatrix} 1226 & \frac{398}{2}b & -\frac{548}{2}a \\ \frac{398}{2}b & \frac{160}{4}b^2 & -\frac{168}{4}ab \\ \frac{548}{2}a & \frac{168}{4}ab & -\frac{240}{4}a^2 \end{bmatrix}, \\
 m_{41} &= \begin{bmatrix} 394 & \frac{232}{2}b & -\frac{232}{2}a \\ -\frac{232}{2}b & -\frac{120}{4}b^2 & \frac{112}{4}ab \\ \frac{232}{2}a & \frac{112}{4}ab & -\frac{120}{4}a^2 \end{bmatrix},
 \end{aligned}$$

$$\begin{aligned}
 m_{32} &= \begin{bmatrix} 394 & -\frac{232}{2}b & -\frac{232}{2}a \\ \frac{232}{2}b & -\frac{120}{4}b^2 & -\frac{112}{4}ab \\ \frac{232}{2}a & -\frac{112}{4}ab & -\frac{120}{4}a^2 \end{bmatrix}, & m_{42} &= \begin{bmatrix} 1226 & -\frac{398}{2}b & -\frac{548}{2}a \\ -\frac{398}{2}b & \frac{160}{4}b^2 & \frac{168}{4}ab \\ \frac{548}{2}a & -\frac{168}{4}ab & -\frac{240}{4}a^2 \end{bmatrix}, \\
 m_{43} &= \begin{bmatrix} 1226 & \frac{548}{2}b & \frac{398}{2}a \\ -\frac{548}{2}b & -\frac{240}{4}b^2 & -\frac{168}{4}ab \\ \frac{398}{2}a & \frac{168}{4}ab & \frac{160}{4}a^2 \end{bmatrix}.
 \end{aligned}$$

The super-diagonal terms of (3.3.6) are the transpose of the sub-diagonal ones

$$\begin{aligned}
 m_{12} &= m_{21}^T, & m_{13} &= m_{31}^T, & m_{14} &= m_{41}^T, \\
 m_{23} &= m_{32}^T, & m_{24} &= m_{42}^T, & m_{34} &= m_{43}^T.
 \end{aligned}$$

Likewise the stiffness matrix for panel  $\Delta_d [k]_d$  is

$$[k]_d = \frac{1}{4(1-\nu^2)ab} \begin{bmatrix} k_{11} & k_{21} & k_{31} & k_{41} \\ k_{21} & k_{22} & k_{23} & k_{24} \\ k_{31} & k_{32} & k_{33} & k_{34} \\ k_{41} & k_{42} & k_{43} & k_{44} \end{bmatrix}, \quad (4.1.2)$$

where the diagonal submatrices are

$$\begin{aligned}
 k_{11} &= \begin{bmatrix} 4 \left( \frac{b^2}{a^2} + \frac{a^2}{b^2} \right) + \frac{2}{5} (7 - 2\nu) & & & \text{Sym} \\ \left[ 2 \frac{a^2}{b^2} + \frac{1}{5} (1 + 4\nu) \right] b & \left[ \frac{4}{3} \frac{a^2}{b^2} + \frac{4}{15} (1 - \nu) \right] b^2 & & \\ - \left[ 2 \frac{b^2}{a^2} + \frac{1}{5} (1 + 4\nu) \right] a & -\nu ab & \left[ \frac{4}{3} \frac{b^2}{a^2} + \frac{4}{15} (1 - \nu) \right] a^2 & \\ k_{22} &= \mathbb{I}_2 k_{11} \mathbb{I}_2, \\ k_{33} &= \mathbb{I}_3 k_{11} \mathbb{I}_3, \\ k_{44} &= \mathbb{I}_4 k_{11} \mathbb{I}_4, \end{bmatrix},
 \end{aligned}$$

and the submatrices corresponding to the first 3 columns are

$$\begin{aligned}
 k_{21} &= \begin{bmatrix} -\left[2\left(\frac{b^2}{a^2} - \frac{a^2}{b^2}\right) + \frac{2}{5}(7-2\nu)\right] & -\left[2\frac{a^2}{b^2} + \frac{1}{5}(1-\nu)\right]b & -\left[\frac{b^2}{a^2} - \frac{1}{5}(1+4\nu)\right]a \\ \left[\frac{a^2}{b^2} - \frac{1}{5}(1+4\nu)\right]b & \left[\frac{2a^2}{3b^2} - \frac{4}{15}(1-\nu)\right]b^2 & 0 \\ -\left[2\frac{b^2}{a^2} + \frac{1}{5}(1-\nu)\right]a & 0 & \left[\frac{2b^2}{3a^2} - \frac{1}{15}(1-\nu)\right]a^2 \end{bmatrix} \\
 k_{31} &= \begin{bmatrix} \left[2\left(\frac{b^2}{a^2} - 2\frac{a^2}{b^2}\right) - \frac{2}{5}(7-2\nu)\right] & -\left[2\frac{a^2}{b^2} + \frac{1}{5}(1-\nu)\right]b & -\left[\frac{b^2}{a^2} - \frac{1}{5}(1+4\nu)\right]a \\ \left[\frac{a^2}{b^2} - \frac{1}{5}(1+4\nu)\right]b & \left[\frac{2a^2}{3b^2} - \frac{4}{15}(1-\nu)\right]b^2 & 0 \\ -\left[2\frac{b^2}{a^2} + \frac{1}{5}(1-\nu)\right]a & 0 & \left[\frac{2b^2}{3a^2} - \frac{1}{15}(1-\nu)\right]a^2 \end{bmatrix} \\
 k_{41} &= \begin{bmatrix} -\left[2\left(\frac{b^2}{a^2} + \frac{a^2}{b^2}\right) - \frac{2}{5}(7-2\nu)\right] & \left[\frac{a^2}{b^2} - \frac{1}{5}(1-\nu)\right]b & -\left[\frac{b^2}{a^2} - \frac{1}{5}(1-\nu)\right]a \\ \left[-\frac{a^2}{b^2} + \frac{1}{5}(1-\nu)\right]b & \left[\frac{1a^2}{3b^2} + \frac{1}{15}(1-\nu)\right]b^2 & 0 \\ \left[\frac{b^2}{a^2} - \frac{1}{5}(1-\nu)\right]a & 0 & \left[\frac{1b^2}{3a^2} + \frac{1}{15}(1-\nu)\right]a^2 \end{bmatrix},
 \end{aligned}$$

with transformation matrices

$$\mathbb{I}_2 = \begin{bmatrix} 1 & & \\ & 1 & \\ & & -1 \end{bmatrix}, \quad \mathbb{I}_3 = \begin{bmatrix} 1 & & \\ & -1 & \\ & & 1 \end{bmatrix}, \quad \mathbb{I}_4 = \begin{bmatrix} -1 & & \\ & 1 & \\ & & 1 \end{bmatrix}.$$

The submatrices of  $[k]_d$  corresponding to the remaining columns on the sub-diagonal side are

$$k_{32} = \mathbb{I}_2 k_{41} \mathbb{I}_2, \quad k_{42} = \mathbb{I}_3 k_{31} \mathbb{I}_3, \quad k_{43} = \mathbb{I}_2 k_{21} \mathbb{I}_2.$$

To assemble both matrices  $[m]_d$  and  $[k]_d$  to form  $\mathbb{K}$  and  $\mathbb{M}$  we use equation (3.3.9) and (3.3.10). However we bypass the process of creating the assembler matrix  $[o]_d$  given in (3.2.6). The procedure to assemble is as follow. We take the elements of the panel matrix in a block of  $6 \times 6$ . Each of these blocks relate two adjacent nodes with plate numbering  $q_j^{(d)}$  and  $q_k^{(d)}$  in  $\Delta_d$ . We then add this block to the plate matrix at row and column positions

given by  $3q_j^{(d)} - 2$  to  $3q_j^{(d)}$  and  $3q_k^{(d)} - 2$  to  $3q_k^{(d)}$ . This assembling procedure is described in Figure 4.1.1.

## 4.2 Implementing the Green's Matrix

In this section we implement the Green's matrix given in subsection 3.5.3. As for the mass and the stiffness matrices we cut short the process of building the Green's matrix in (3.5.18) by excluding the assembler matrix  $[o]_d$  and using the diagram described by Figure 4.1.1. Then we are left to find  $[g]_{de}$  using (3.5.27) and hence  $\mathbb{G}_1$  and  $\mathbb{G}_2$  given by (3.5.28) and (3.5.29).

We generate matrix  $\mathbb{G}_1$  once only and use it for the entire plate. This is because all panels are identical and discretized in the same way. On the other hand  $\mathbb{G}_2$  must be generated individually for each combination of distinct  $\Delta_d$  and  $\Delta_e$ . Therefore the process of generating  $[g]_{de}$  for distinct panels is very costly because we need to compose a new  $\mathbb{G}_2$  for different  $\Delta_d$  and  $\Delta_e$ . In total we generate  $\mathbb{G}_2$   $p^2$  times. In order to cut down the number of times we compose  $\mathbb{G}_2$  we use the following method. For a  $\mathbb{G}_2$  that acts upon field panel  $\Delta_d$  and source panel  $\Delta_e$  we call this  $\mathbb{G}_{2,d,e}$ . Then we notice that

$$\mathbb{G}_{2,e,d} = \mathbb{G}_{2,d,e}^T.$$

Therefore for any combination of field panel  $\Delta_d$  and source panel  $\Delta_e$  we may skip the reverse case (the field panel  $\Delta_e$  and the source panel  $\Delta_d$ ). This enables us to cut the number of computing  $\mathbb{G}_{2,e,d}$  from  $p^2$  to  $\frac{1}{2}(p+1)p$  (obtained from the arithmetic sum of  $p$ ).

In the implemented code we generate a composite matrix that contains all the  $\mathbb{G}_{2,d,e}$  with field panel  $\Delta_d$  and source panel  $\Delta_e$ ,  $d+1 \leq e \leq p$ .

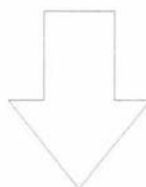
$$\mathbb{G}_{2,d} = [ \mathbb{G}_{2,d,d+1} \quad \mathbb{G}_{2,d,d+2} \quad \dots \quad \mathbb{G}_{2,d,p} ]. \quad (4.2.1)$$

We do this because the computer calculates the Green's function described in (2.3.11) and (2.3.13) more efficiently if the variables supplied are stored in array-form rather than as individual numbers. The column dimension of the composite matrix (4.2.1) shrinks as we

The general format of a panel matrix

$q_1^{(d)} q_1^{(d)}$	$q_1^{(d)} q_2^{(d)}$	$q_1^{(d)} q_3^{(d)}$	$q_1^{(d)} q_4^{(d)}$
$q_2^{(d)} q_1^{(d)}$	$q_2^{(d)} q_2^{(d)}$	$q_2^{(d)} q_3^{(d)}$	$q_2^{(d)} q_4^{(d)}$
$q_3^{(d)} q_1^{(d)}$	$q_3^{(d)} q_2^{(d)}$	$q_3^{(d)} q_3^{(d)}$	$q_3^{(d)} q_4^{(d)}$
$q_4^{(d)} q_1^{(d)}$	$q_4^{(d)} q_2^{(d)}$	$q_4^{(d)} q_3^{(d)}$	$q_4^{(d)} q_4^{(d)}$

A block of 3x3



The general format of a plate matrix

	$3q_1^{(d)} - 2 \rightarrow 3q_1^{(d)}$	$3q_2^{(d)} - 2 \rightarrow 3q_2^{(d)}$		$3q_3^{(d)} - 2 \rightarrow 3q_3^{(d)}$	$3q_4^{(d)} - 2 \rightarrow 3q_4^{(d)}$	
$\dots$			$\dots$			$\dots$
$3q_1^{(d)} - 2 \rightarrow 3q_1^{(d)}$	$q_1^{(d)} q_1^{(d)}$	$q_1^{(d)} q_2^{(d)}$		$q_1^{(d)} q_3^{(d)}$	$q_1^{(d)} q_4^{(d)}$	
$3q_2^{(d)} - 2 \rightarrow 3q_2^{(d)}$	$q_2^{(d)} q_1^{(d)}$	$q_2^{(d)} q_2^{(d)}$		$q_2^{(d)} q_3^{(d)}$	$q_2^{(d)} q_4^{(d)}$	
$\vdots$			$\vdots$			$\vdots$
$3q_3^{(d)} - 2 \rightarrow 3q_3^{(d)}$	$q_3^{(d)} q_1^{(d)}$	$q_3^{(d)} q_2^{(d)}$		$q_3^{(d)} q_3^{(d)}$	$q_3^{(d)} q_4^{(d)}$	
$3q_4^{(d)} - 2 \rightarrow 3q_4^{(d)}$	$q_4^{(d)} q_1^{(d)}$	$q_4^{(d)} q_2^{(d)}$		$q_4^{(d)} q_3^{(d)}$	$q_4^{(d)} q_4^{(d)}$	
$\dots$						$\dots$

Figure 4.1.1. The distribution diagram of a panel matrix into the matrix for the plate.

traverse each  $\Delta_d$  from  $d = 1$  until  $d = p$ . The maximum column dimension is  $p \times Q$  ( $d = 1$ ) and the minimum is  $Q$  ( $d = p$ ). However the row dimension is fixed at  $Q$  (the number of integration points over  $\Delta_d$ ).

## 4.3 Results

In this section we test and present the results of our method. First we compare the solution by Meylan's method (low order) to our results (higher order). Then we present the convergence tests for the method based on the number of integration points and the number of panels. Finally we show the displacement the single floe model computed by the higher order method.

### 4.3.1 The Comparison Between Meylan's Method and the Higher Order Method

First we test the convergence of Meylan's method and the higher order method using different discretization schemes. Separately we also test the convergence of our method using different discretization schemes. To show that the two methods agree and that our method is of higher order than Meylan's method we compare their errors for different discretization. For all these tests this is done by comparing the error in the displacement using different number of panels. The error between the plate with  $n$  panels and one with  $m$  panels is given by the following error measurement

$$E_{nm} = \int_{\Delta} |w_n - w_m|^2 dS_{\mathbf{x}}. \quad (4.3.1)$$

We use a square plate of area 16 with stiffness  $\beta = 0.01$  and mass  $\gamma = 0$ . The wavelength is  $\lambda = 2$  and the direction of propagation is  $\theta = \pi/6$ . The incident amplitude is  $A^{In} = 1$ . The water depth is infinite. Table 4.3.1. shows the error function  $E_{mn}$  for Meylan's method using 100 to 1600 panels compared to 2500 panels.

$n$	$m$	$E_{nm}$
100	2500	$1.7150 \times 10^{-2}$
400	2500	$7.3985 \times 10^{-4}$
900	2500	$6.5394 \times 10^{-5}$
1600	2500	$5.1326 \times 10^{-5}$

Table 4.3.1. The error  $E_{nm}$  in the results by Meylan's method using different number of panels. Column  $n$  represents the varying number of panels and column  $m$  is the reference of 2500 panels. The plate used is a square with area 16, stiffness  $\beta = 0.01$ , and mass  $\gamma = 0$ . The wave parameters are  $\lambda = 2$  and  $\theta = \pi/6$ . The table shows that the result converges as we increase the number of panels used to discretized the plate.

$n$	$m$	$E_{nm}$
100	900	$6.0633 \times 10^{-4}$
225	900	$1.3738 \times 10^{-4}$
400	900	$3.0189 \times 10^{-5}$
625	900	$4.2500 \times 10^{-6}$

Table 4.3.2. The error  $E_{nm}$  in the results produced by the higher order method using different number of panels. Column  $n$  represents the varying number of panels and column  $m$  is the reference of 900 panels. The plate used is a square with area 16, stiffness  $\beta = 0.01$ , and mass  $\gamma = 0$ . The wave parameters are  $\lambda = 2$  and  $\theta = \pi/6$ . The table shows that the result converges as we increase the number of panels used to discretized the plate.

$m$	$n$	$E_{nm}$
100	900	$1.3930 \times 10^{-2}$
400	900	$1.0291 \times 10^{-3}$
900	900	$3.6510 \times 10^{-4}$
1600	900	$2.2061 \times 10^{-4}$
2500	900	$1.5050 \times 10^{-4}$

Table 4.3.3. The error  $E_{nm}$  in the results by Meylan's low order method versus the results by the higher order method. Column  $n$  represents Meylan's method that uses various number of panels and column  $m$  is the reference that is the higher order method with 900 panels. The plate used is a square with area 16, stiffness  $\beta = 0.01$ , and mass  $\gamma = 0$ . The wave parameters are  $\lambda = 2$  and  $\theta = \pi/6$ . The table shows that the accuracy using 2500 panels in Meylan's method is equivalent to the accuracy using 900 panels in the higher order method.

We investigate the accuracy of our method compared to Meylan's method. Table 4.3.3. shows the comparison between the results computed using Meylan's method with 100 to 2500 panels and the higher order method with 900 panels. This is done by taking the absolute error between Meylan's result with the result from the higher order methods with 900 panels. From Table 4.3.3. we see that the higher order method only needs approximately half the number of panels used in Meylan's method to achieve the same accuracy.

Finally we show the plate displacement produced using Meylan's method and the higher order one. Figure 4.3.1. is the comparison in the displacement  $w/A$  of a square plate with area 16 ( $L = 4$ ) computed using the two methods. The stiffness and the mass of the plate are, respectively,  $\beta = 0.01$  and  $\gamma = 0$ . For Meylan's method the plate is discretized using 900 panels. For the higher order method the plate is discretized using 100 panels and the numerical integration in each panel is done using Gauss-Legendre quadrature with  $Q = 16$  and  $P = 16$ , with exception that if  $d = e$  then  $P = 64$ . The parameters for the incident wave are length  $\lambda = 2$  ( $k = \pi$ ) and direction of propagation  $\theta = \pi/6$ . The water is infinitely deep. From the Table 4.3.3. and Figure 4.3.1. we see that our method agrees with Meylan's method.

### 4.3.2 The Convergence of the Higher Order Method

Next we show the effect of the quadrature points and the panels on the accuracy of the solution by the higher order method. We first use different number of quadrature points in the Gauss-Legendre numerical integration scheme. Then we use the Kochin's function to show the effect of panel size on the solution.

The first test for the convergence of the higher order method is done by varying the number of quadrature points used to integrate the area of the panel. We use the error  $E_{QP}$  (4.3.1) where  $w_Q$  and  $w_P$  are the displacement calculated using various number of panels with  $Q$  and  $P$  number of quadrature points. For this test the square plate area is 16 ( $L = 4$ ), its stiffness is  $\beta = 0.01$ , and its mass is  $\gamma = 0$ . The wavelength is  $\lambda = 2$  ( $k = \pi$ ) and the waveangle is  $\theta = \pi/6$ . The incident amplitude is  $A^{In} = 1$ . Table 4.3.4. shows the error

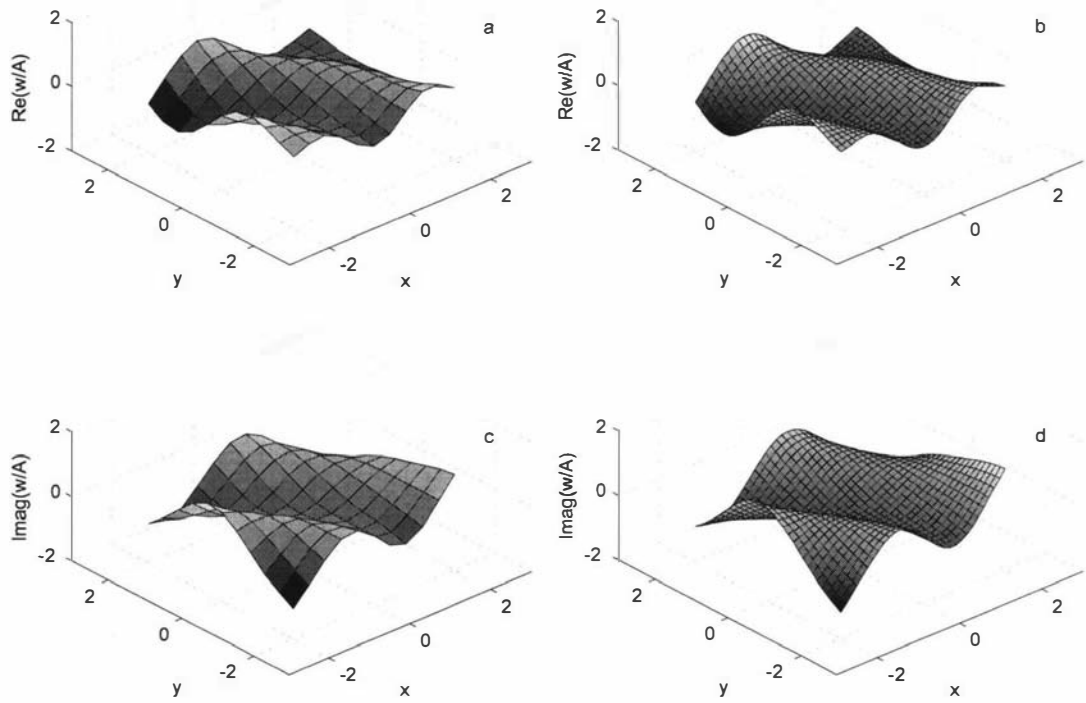


Figure 4.3.1. The comparison of the plate's displacement generated by Meylan's method with 900 panels (right hand side) and the higher order method with 100 panels (left hand side). The plate is of stiffness  $\beta = 0.01$  and mass  $\gamma = 0$ . The incident wave has length  $\lambda = 2$  and propagates at waveangle  $\theta = \pi/6$ . The water is infinitely deep.

$E_{QP}$  versus the number of panels. From this table we see that increasing the number of Gaussian quadrature points does not significantly increase the accuracy of the solution.

The second convergence test is performed using five different shapes. Figure 4.3.2. shows the geometries of the plate used for this test and for later results. We notice that except for the square plate the discretization by square panels only approximates the plates. For shapes that are not square the size of the panels affects the shapes greatly. An example is shown in Figure 4.3.3. where an isosceles triangle is discretized using panels of different sizes. We can clearly see that the composition of panels in Figure 4.3.3. (a) and (b) produce different shapes though both approximate the same triangle.

We intend to investigate the effect of discretization of the shapes by square panels since we can only approximate a shape, such as a triangle, by square panels. We use the Kochin's function defined as

$$H(\tau) = \int_{\Delta} \left\{ k\phi(\mathbf{x}) + i\sqrt{k}w(\mathbf{x}) \right\} \exp(ik(x \cos \tau + y \sin \tau)) dS_{\mathbf{x}}, \quad (4.3.2)$$

[Wehausen & Laitone, 1960]. The scattered energy is found by multiplying the absolute value squared of the Kochin's function  $H(\tau)$  with a constant. We show  $|H(\tau)|$  for a square, a triangular, a circular, a parallelogram, and a trapezoidal plate using different number of panels. Four different stiffness parameters are used to show the effect of  $\beta = 0.0025, 0.005, 0.01, \text{ and } 0.02$ . For this test all plates have uniform area of 16 and mass  $\gamma = 0$ . The incident wave of amplitude  $A^{In} = 1$  propagates at direction  $\theta = \pi/6$  and the wavelength is  $\lambda = 2$ .

Figure 4.3.4., Figure 4.3.5., Figure 4.3.6., Figure 4.3.7., and Figure 4.3.8. contain the plots of the absolute value of Kochin's function for, respectively, a square, a triangle, a circle, a parallelogram, and a trapezoid shape plate with stiffness specified by  $\beta$ . We see that as we increase the number of panels we achieve convergence. Moreover we find that for shapes other than the squares the discretization using 32 panels is insufficient to produce accurate result. This is shown in Figure 4.3.5. to Figure 4.3.8. and the last shows the clearest.

number of panels	$E_{QP}$				
	$Q, P = 16$	$Q, P = 25$	$Q, P = 36$	$Q, P = 49$	$Q, P = 64$
100	$6.0633 \times 10^{-4}$	$5.7995 \times 10^{-4}$	$4.3308 \times 10^{-4}$	$3.4487 \times 10^{-4}$	$3.2671 \times 10^{-4}$
400	$3.0189 \times 10^{-5}$	$3.0101 \times 10^{-5}$	$2.1483 \times 10^{-5}$	$1.7296 \times 10^{-5}$	$1.6292 \times 10^{-5}$
900	$2.8856 \times 10^{-8}$	$9.7444 \times 10^{-8}$	$1.5016 \times 10^{-8}$	$4.3800 \times 10^{-10}$	0

Table 4.3.4. The error  $E_{QP}$  showing the convergence of the higher order method using various number of panels versus number of quadrature points. The referencing result uses 900 panels and 64 quadrature points. The area of the square plate is 16, its stiffness is  $\beta = 0.01$ , and its mass is  $\gamma = 0$ . The wavelength is  $\lambda = 2$  and the waveangle is  $\gamma = 0$ .

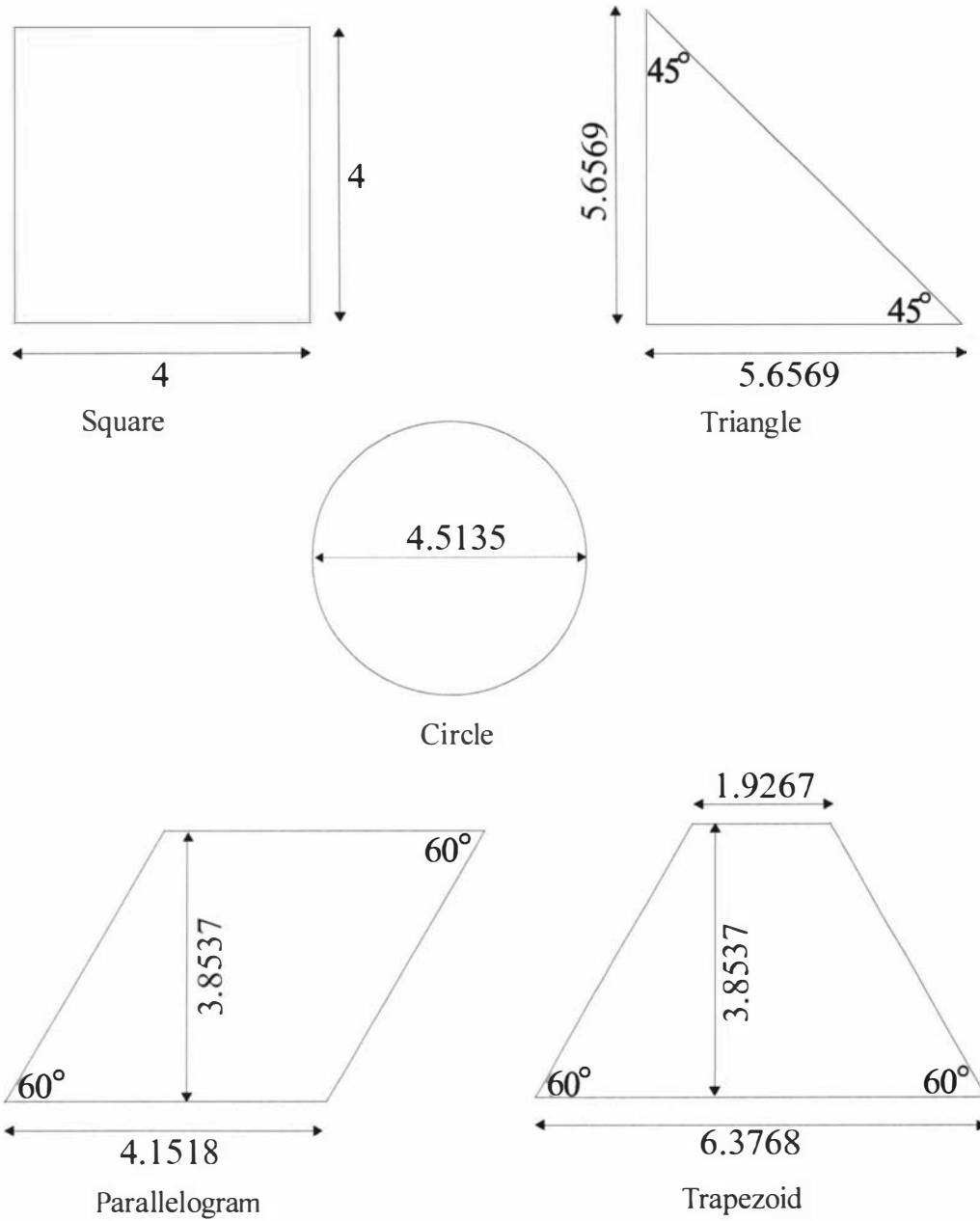


Figure 4.3.2. The diagram showing the five geometries of the plate shapes that will be used to illustrate the subsequent examples using the higher order method. The direction of the incident wave is shown in Figure 2.1.1.

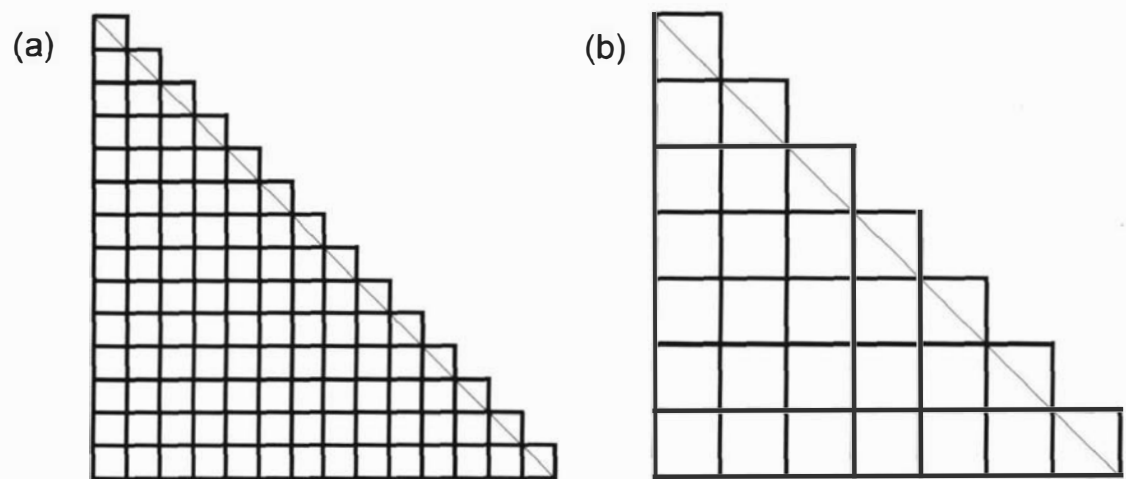


Figure 4.3.3. An illustration of the effect of panel size on approximating an isosceles triangle. The size of the panels in (b) are double from the ones in (a).

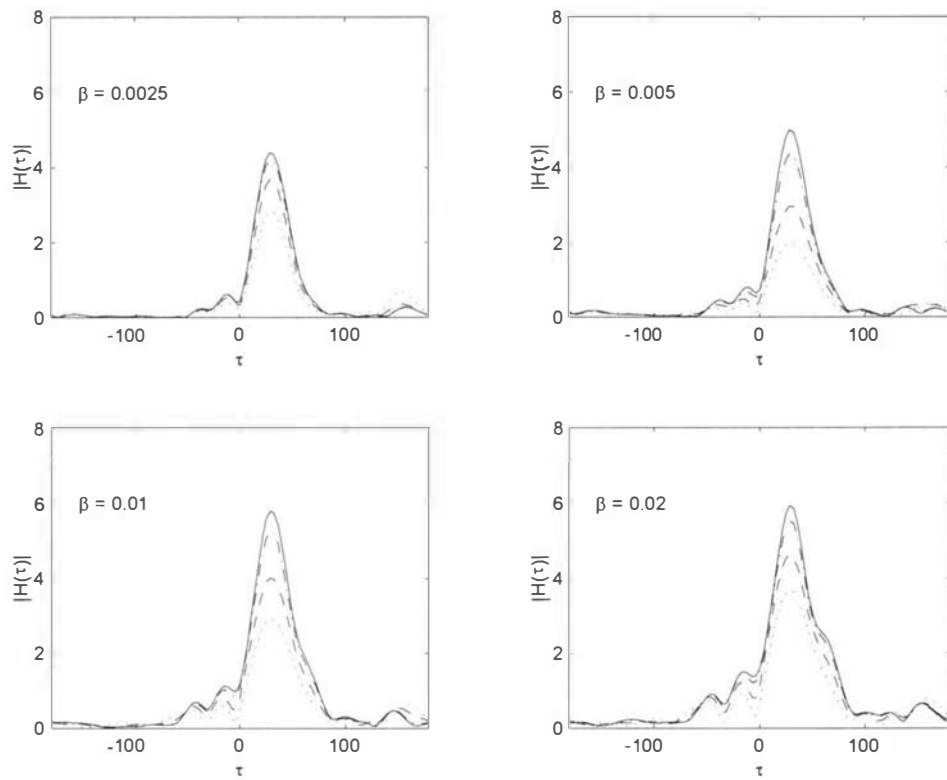


Figure 4.3.4. The absolute value of the Kochin's function  $H(\tau)$  as a function of the angle  $\tau$  for a square plate of area 16, mass  $\gamma = 0$ , and given stiffness. The number of panels used are 32 (dotted line), 64 (broken line), 128 (chained line), and 256 (solid line). The incident wave of unit amplitude has wavelength  $\lambda = 2$  and waveangle  $\theta = \pi/6$ . The figures show the energy scattering around the square plate for given stiffness constants  $\beta$ .

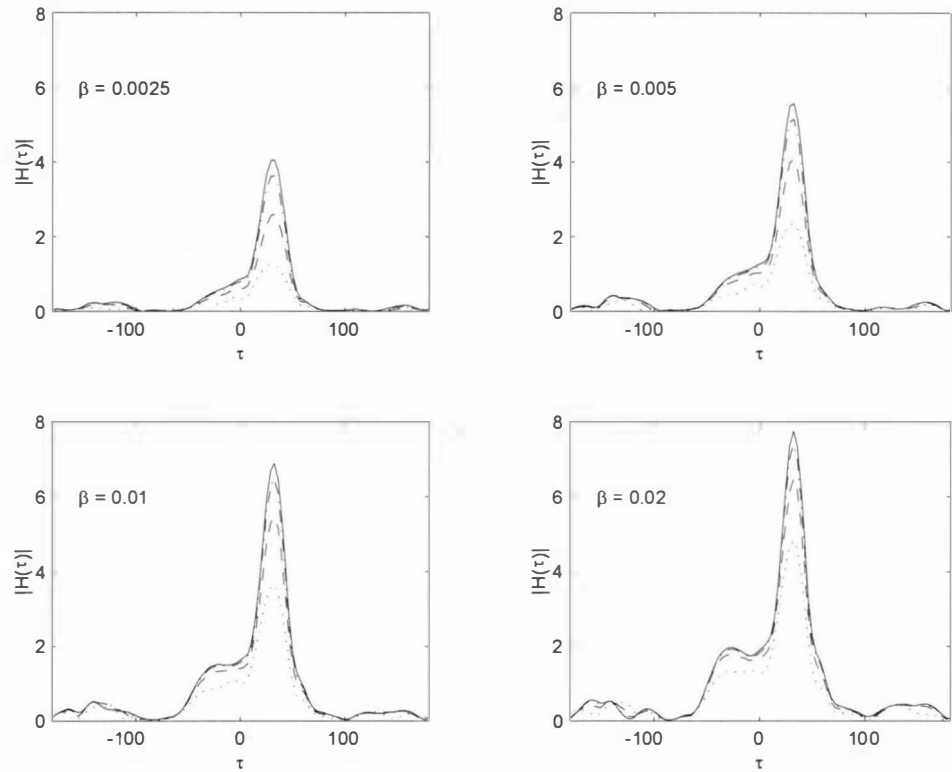


Figure 4.3.5. The absolute value of the Kochin's function  $H(\tau)$  as a function of the angle  $\tau$  for a triangular plate of area 16, mass  $\gamma = 0$ , and given stiffness. The number of panels used are approximately 32 (dotted line), 64 (broken line), 128 (chained line), and 256 (solid line). The incident wave of unit amplitude has wavelength  $\lambda = 2$  and waveangle  $\theta = \pi/6$ . The figures show the energy scattering around the triangular plate for given stiffness constants  $\beta$ .

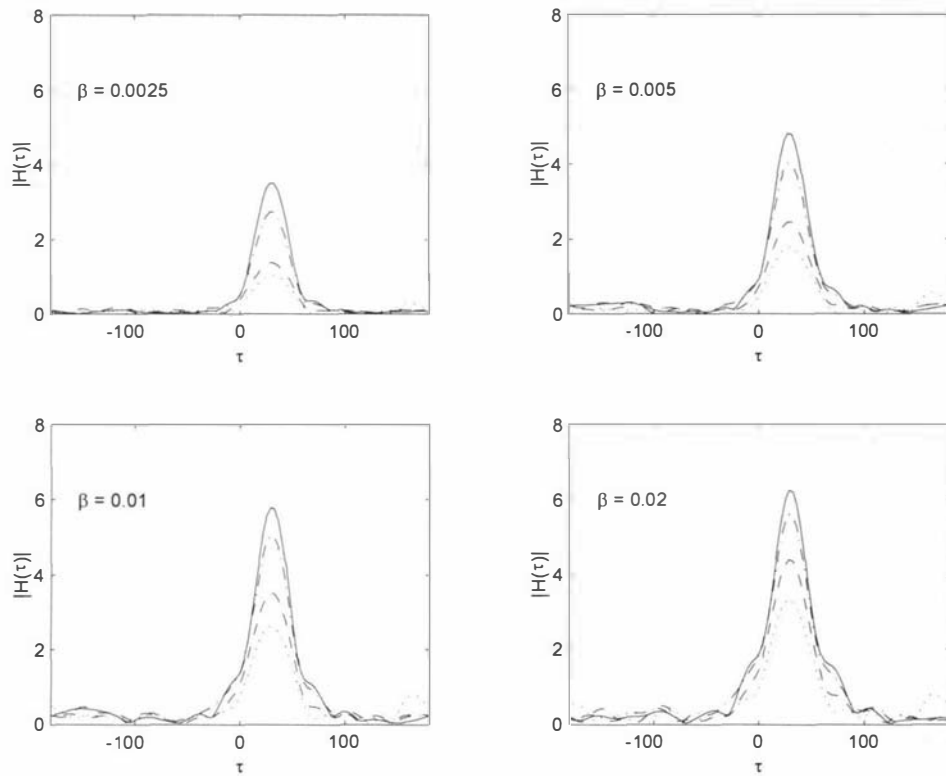


Figure 4.3.6. The absolute value of the Kochin's function  $H(\tau)$  as a function of the angle  $\tau$  for a circular plate of area 16, mass  $\gamma = 0$ , and given stiffness. The number of panels used are approximately 32 (dotted line), 64 (broken line), 128 (chained line), and 256 (solid line). The incident wave of unit amplitude has wavelength  $\lambda = 2$  and waveangle  $\theta = \pi/6$ . The figures show the energy scattering around the circle plate for given stiffness constants  $\beta$ .

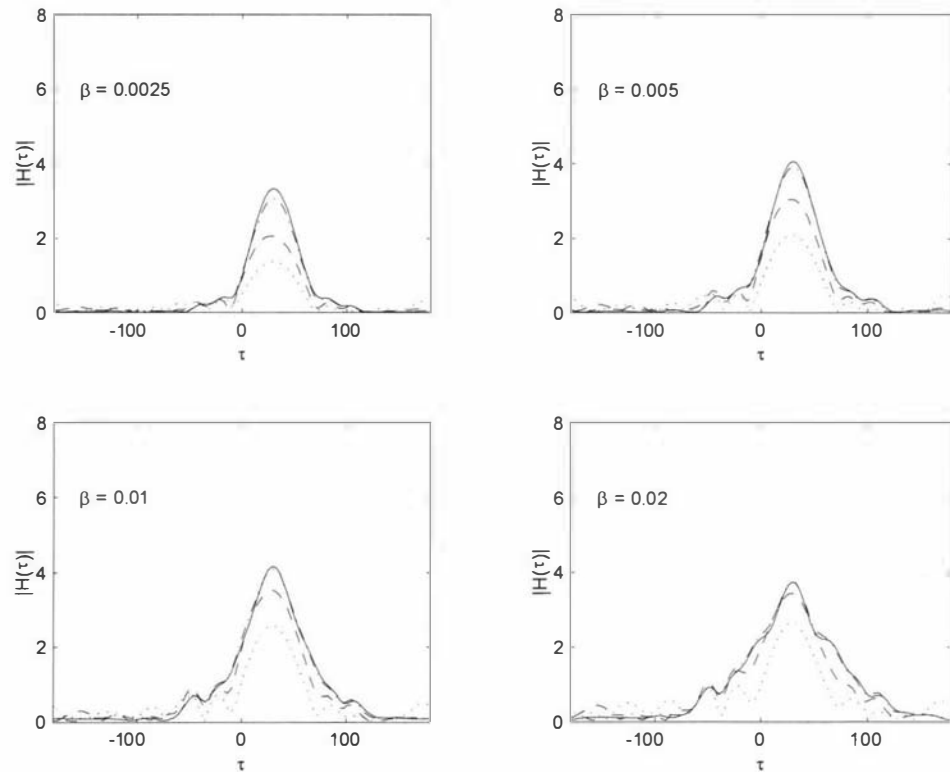


Figure 4.3.7. The absolute value of the Kochin's function  $H(\tau)$  as a function of the angle  $\tau$  for a parallelogram plate of area 16, mass  $\gamma = 0$ , and given stiffness. The number of panels used are approximately 32 (dotted line), 64 (broken line), 128 (chained line), and 256 (solid line). The incident wave of unit amplitude has wavelength  $\lambda = 2$  and waveangle  $\theta = \pi/6$ . The figures show the energy scattering around the parallelogram plate for given stiffness constants  $\beta$ .

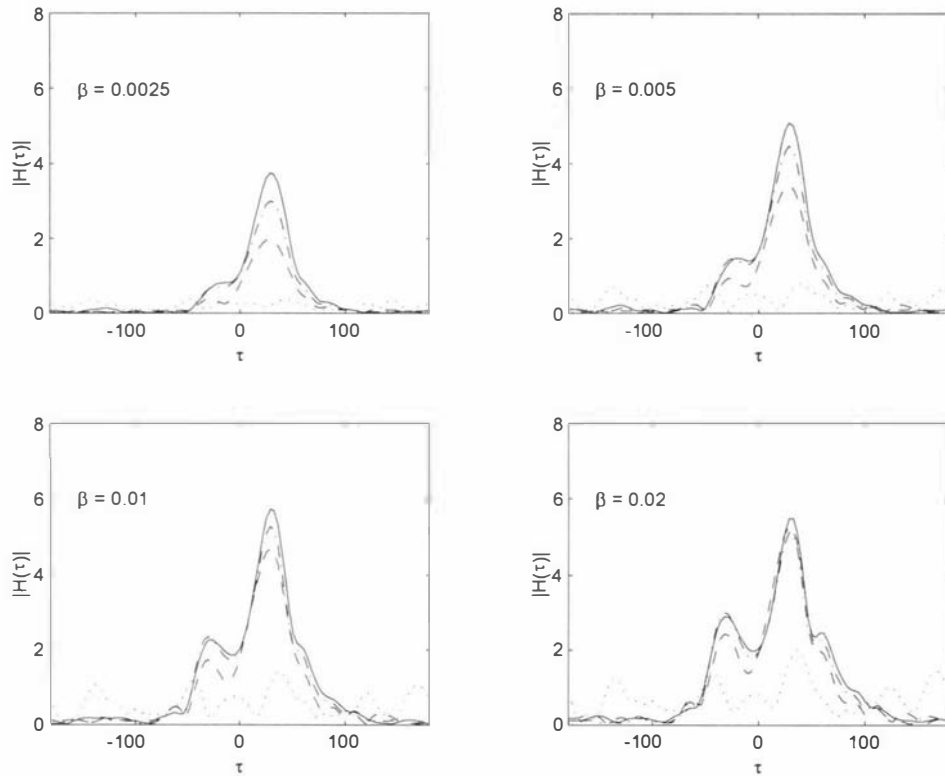


Figure 4.3.8. The absolute value of the Kochin's function  $H(\tau)$  as a function of the angle  $\tau$  for a trapezoidal plate of area 16, mass  $\gamma = 0$ , and given stiffness. The number of panels used are approximately 32 (dotted line), 64 (broken line), 128 (chained line), and 256 (solid line). The incident wave of unit amplitude has wavelength  $\lambda = 2$  and waveangle  $\theta = \pi/6$ . The figures show the energy scattering around the trapezoidal plate for given stiffness constants  $\beta$ .

### 4.3.3 The Displacement of the Plate

Finally we present the results from applying the higher order method to calculate the response of the plate due to the water wave forcing. The results are based on five plate shapes floating on water of depth  $H = 1/64$ ,  $H = 1/16$ ,  $H = 1/4$ , and  $H \rightarrow \infty$ . Uniformly all plates have area 16 ( $L = 4$ ), stiffness  $\beta = 0.01$ , and mass  $\gamma = 0$ . Each is discretized with approximately 100 panels. The integration over a panel is done using 16 Gauss-Legendre quadrature points. The incident wave has fixed amplitude  $A^{In} = 1$ , wavelength  $\lambda = 2$  (i.e. the depth of water does not affect the wavelength), and waveangle is  $\theta = \pi/6$ . We do these so that we can clearly see the affect of varying the water depth.

We choose to plot the result in terms of the plate displacement because the interaction between the water and the plate can be observed easily this way. Clearly the potential can be obtained in the same way as the displacement. Figure 4.3.9., Figure 4.3.10., Figure 4.3.11., Figure 4.3.12., and Figure 4.3.13. show the real part of the displacement of, respectively, a square, a triangle, a circle, a parallelogram, and a trapezoid. All are calculated using the specified water depth.

We see from Figure 4.3.9., 4.3.10., 4.3.11., 4.3.12., and 4.3.13 that the depth of the water influences the wave frequency and also the wavelength. We find that the deeper the water the higher the frequency of the wave and therefore the shorter the wavelength. Notice that waves with short wavelength ‘notice’ the plate and hence, as shown in the figures, the displacements of the plates vary significantly for deep water.

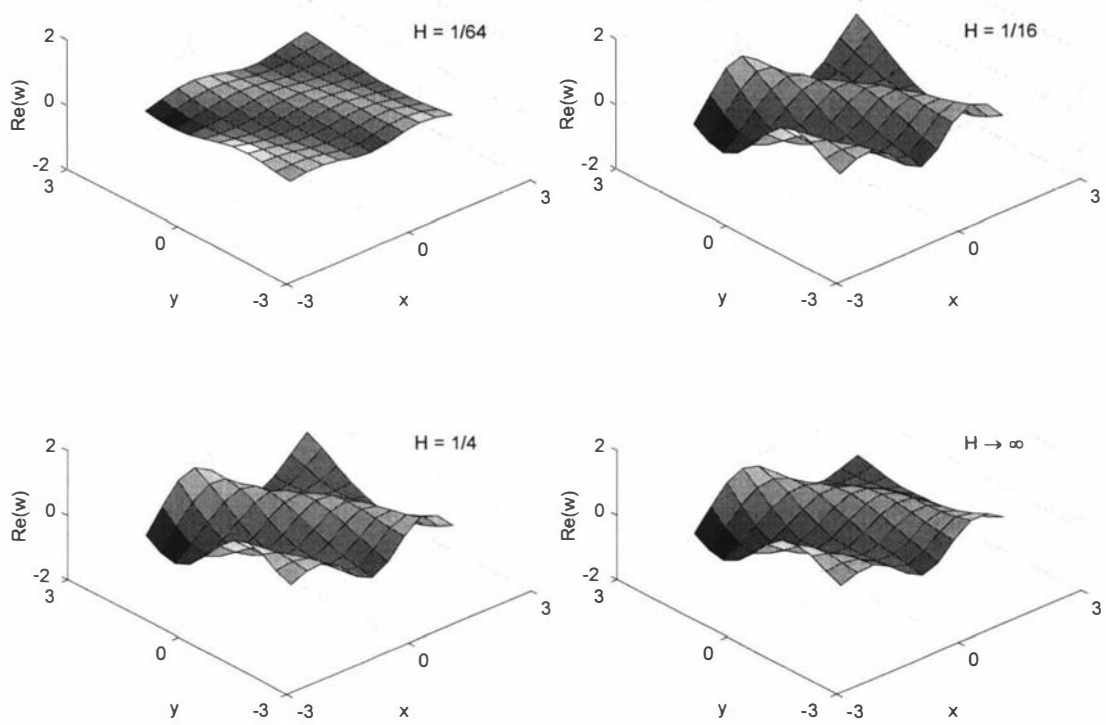


Figure 4.3.9. The displacement of a square plate with area 16, stiffness  $\beta = 0.01$ , and mass  $\gamma = 0$  floating on water of given depth. The plate is discretized using 100 panels. The area integral over the panel uses 16 quadrature points. The incident wave of unit amplitude and length  $\lambda = 2$  propagates at angle  $\theta = \pi/6$ . The figures show that waves with higher frequency (deeper water) affect the plate's displacement more than waves with lower frequency (shallower water).

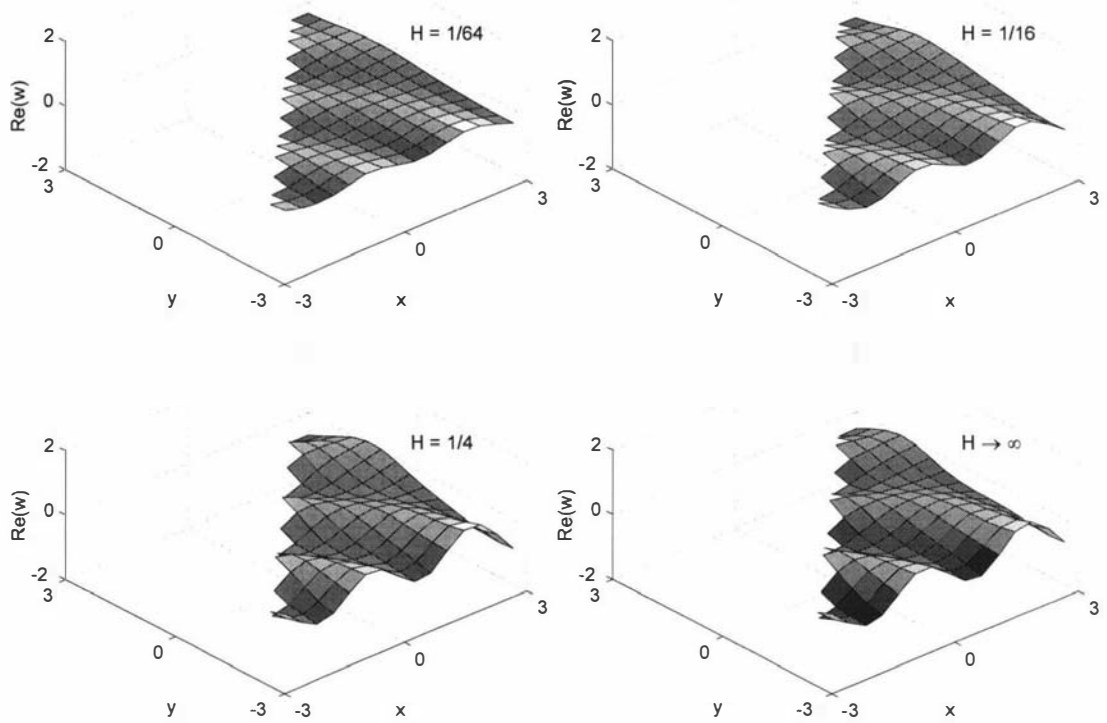


Figure 4.3.10. The displacement of a triangular plate with area 16, stiffness  $\beta = 0.01$ , and mass  $\gamma = 0$  floating on water of given depth. The plate is discretized using 105 panels. The area integral over the panel uses 16 quadrature points. The incident wave of unit amplitude and length  $\lambda = 2$  propagates at angle  $\theta = \pi/6$ . The figures show that waves with higher frequency (deeper water) affect the plate's displacement more than waves with lower frequency (shallower water).

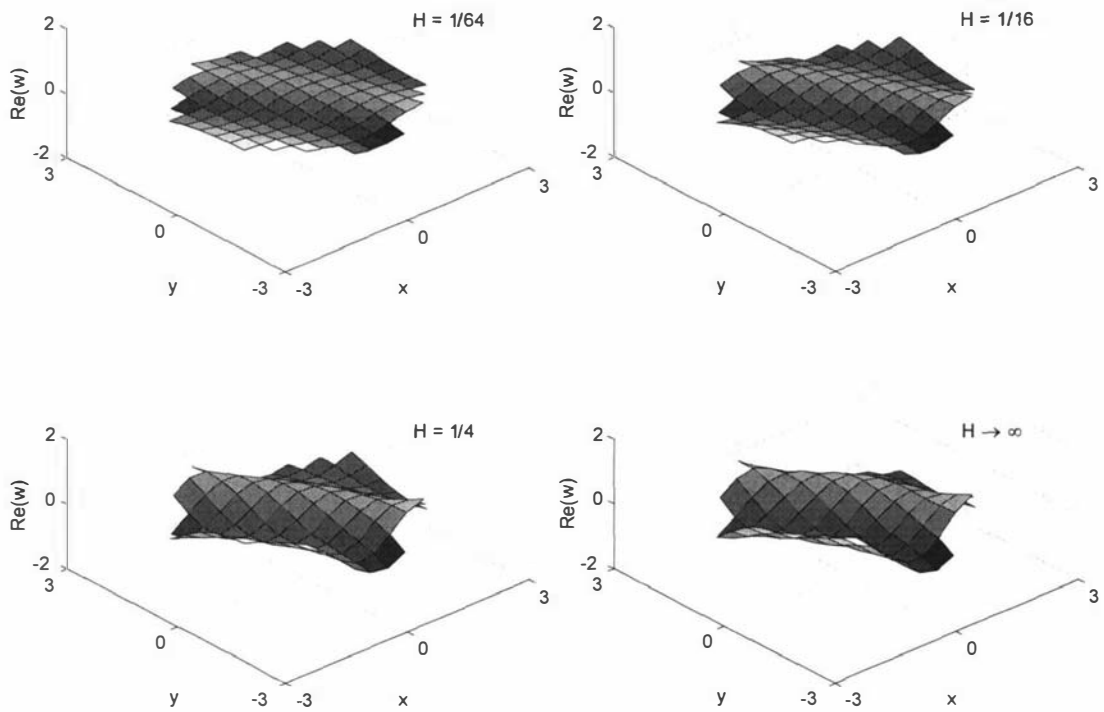


Figure 4.3.11. The displacement of a circular plate with area 16, stiffness  $\beta = 0.01$ , and mass  $\gamma = 0$  floating on water of given depth. The plate is discretized using 93 panels. The area integral over the panel uses 16 quadrature points. The incident wave of unit amplitude and length  $\lambda = 2$  propagates at angle  $\theta = \pi/6$ . The figures show that waves with higher frequency (deeper water) affect the plate's displacement more than waves with lower frequency (shallower water).

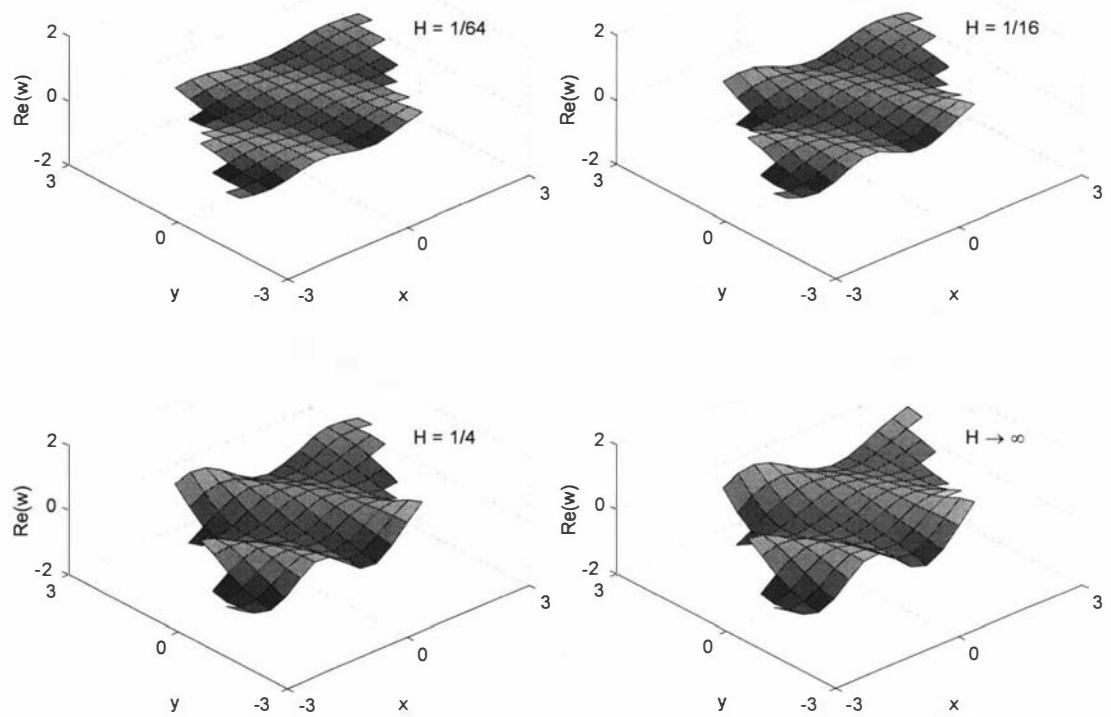


Figure 4.3.12. The displacement of a parallelogram plate with area 16, stiffness  $\beta = 0.01$ , and mass  $\gamma = 0$  floating on water of given depth. The plate is discretized using 110 panels. The area integral over the panel uses 16 quadrature points. The incident wave of unit amplitude and length  $\lambda = 2$  propagates at angle  $\theta = \pi/6$ . The figures show that waves with higher frequency (deeper water) affect the plate's displacement more than waves with lower frequency (shallower water).

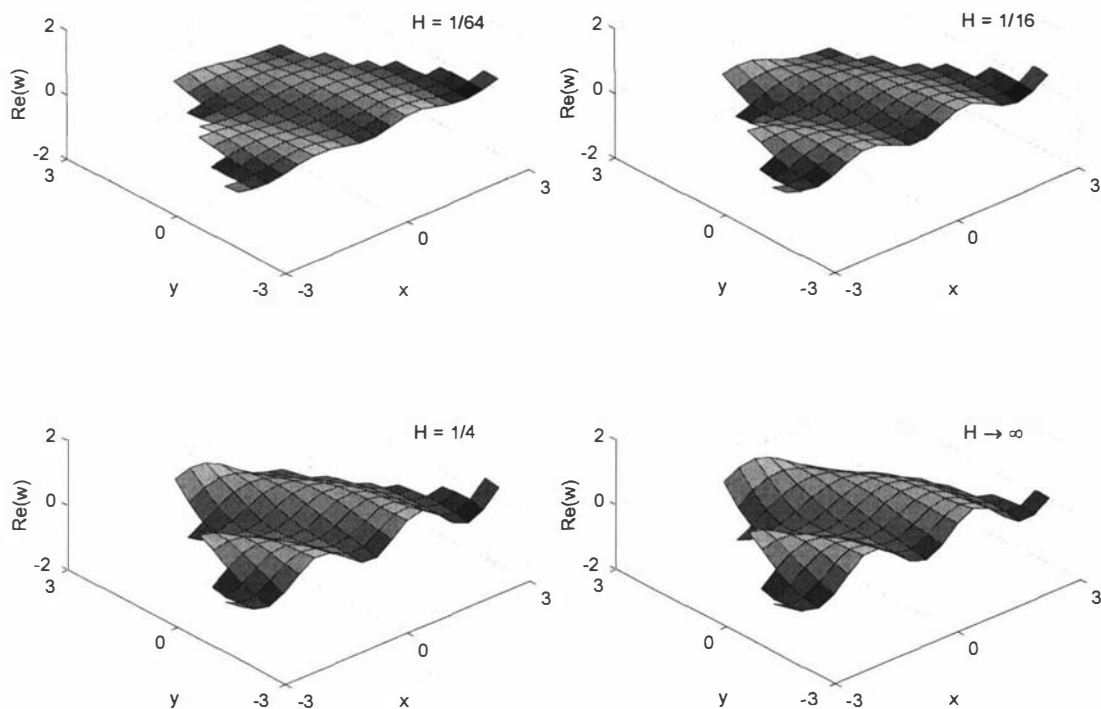


Figure 4.3.13. The displacement of a trapezoidal plate with area 16, stiffness  $\beta = 0.01$ , and mass  $\gamma = 0$  that floats on water of given depth. The plate is discretized using 116 panels. The area integral over the panel uses 16 quadrature points. The incident wave of unit amplitude and length  $\lambda = 2$  propagates at angle  $\theta = \pi/6$ . The figures show that waves with higher frequency (deeper water) affect the plate's displacement more than waves with lower frequency (shallower water).

# Chapter 5

## An Infinite Line-Array of Periodically-Arranged Identical Plates

In this chapter we explain the method to calculate the hydroelastic response of an infinite line-array of periodically-arranged identical plates on infinitely deep water. We are motivated by the scattering of waves by ice floes. The description of the line-array and its resemblance to the diffraction grating from optics are given in the first section. The second section contains the application of diffraction theory (Floquet's theorem) to the coupled line-array of plates and water motion. This yields a new free-surface Green's function, which later we will call the periodic Green's function. The third section contains the far-field representation of the periodic Green's function. We give two representations, one in the spatial domain and one in the spectral domain. The last section provides the recipe to accelerate the convergence of this Green's function.

### 5.1 The Application of Diffraction Grating

In this section we explain the physical meaning of an infinite line-array of periodically-arranged identical plates. We will relate this line-array to the diffraction gratings in optics.

We introduce an infinite line-array of identical plates that spans across the  $y$ -axis from  $-\infty$  to  $\infty$ . This composition of plates is depicted by Figure 5.1.1. The plates are separated at a uniform distance. We choose arbitrarily a plate  $\Delta_0$  and confining it between a pair of artificial partitions at  $y = -l/2$  and  $y = l/2$ . We repeat this for each plate. Thus for plates with centres located respectively at  $(0, y + (m - 1)l)$  and  $(0, y + ml)$  they are separated by partition at  $y = (2m - 1)l/2$ ,  $m = \dots - 2, -1, 0, 1, 2, \dots$ . We call the region

between a pair of partitions a *channel* and the empty region unoccupied by the plates a *gap* (denoted by  $b$ ).

We refer to the plates other than  $\Delta_0$  as the images of  $\Delta_0$ . Each of them is labelled by  $\Delta_m$ . We have an *infinite number of images*. Note that such arrangement of plates is analogous to the diffraction grating in optics, in particular a two-dimensional periodic (surface) grating. However since the grating is only periodic along the  $y$ -axis from  $-\infty$  to  $\infty$  and is not periodic in the  $x$  direction this simplifies our problem to a one dimensional periodic grating. Moreover each of the plates are confined within a channel of width  $l$ .

## 5.2 The Application of the Floquet's Theorem to the Periodic Grating

In this section we apply the theory from the diffraction gratings to the infinite line-array of periodic plates. We use the Floquet's theorem to describe the scattering by the periodic grating. Floquet's theorem states that: for a given incident wave whose direction is inclined at angle  $\theta$  from the  $x$ -axis the waves scattered by such grating are periodic with periodicity equal to the width of the channel  $l$  [Scott, 1998]. Thus the potential and the displacement from one plate to another differ only by a phase factor.

We suppose the potential under an arbitrary plate  $\Delta_0$  is given by  $\phi(\mathbf{x}_0)$ ,  $\mathbf{x}_0 \in \Delta_0$ . Using the Floquet's theorem the plate  $\Delta_1$  in the channel next to the one that confined  $\Delta_0$  has potential

$$\phi(\mathbf{x}_1) = \phi(\mathbf{x}_0) e^{i\sigma l},$$

and displacement

$$w(\mathbf{x}_1) = w(\mathbf{x}_0) e^{i\sigma l}$$

where  $\mathbf{x}_1 \in \Delta_1$ ,

$$\sigma = k \sin \theta, \tag{5.2.1}$$

and  $\theta$  is the angle of incidence. Clearly the phase difference is  $\sigma l = kl \sin \theta$ . The phase difference reaches the minimum when  $\theta = -\pi/2$  (i.e.  $\sin \theta = -1$ ) and it reaches the

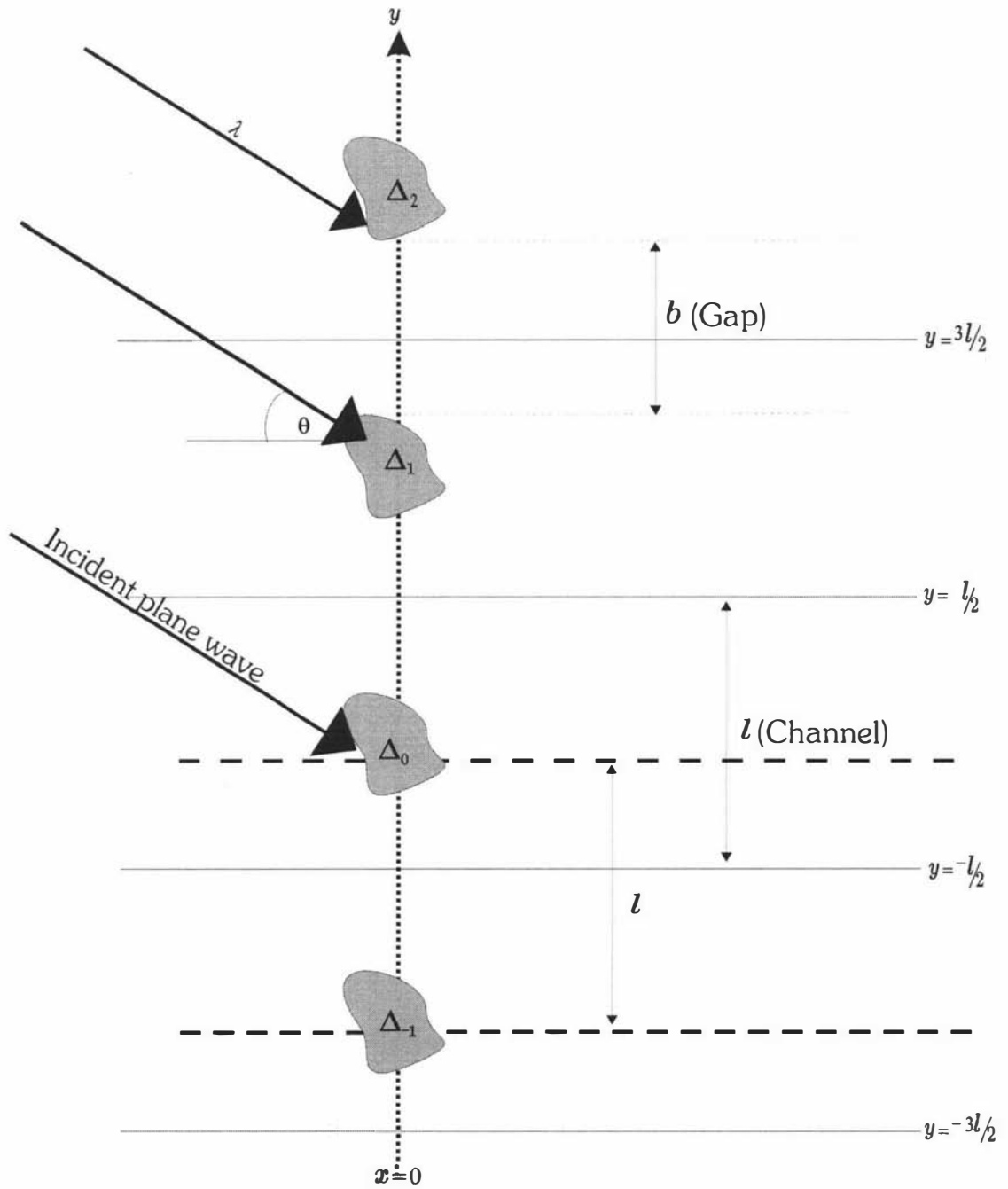


Figure 5.1.1. The depiction of the periodic surface grating that represents the array of identical floes.

maximum when  $\theta = \pi/2$  (i.e.  $\sin \theta = 1$ ). This implies the phase difference must be

$$-kl < \sigma l < kl,$$

and thus [Linton, 1998]

$$-k < \sigma < k.$$

Hence, regardless of the direction, the potential for  $\mathbf{x}_m \in \Delta_m$  is

$$\phi(\mathbf{x}_m) = \phi(\mathbf{x}_0) e^{im\sigma l}, \quad (5.2.2)$$

and similarly the displacement is

$$w(\mathbf{x}_m) = w(\mathbf{x}_0) e^{im\sigma l}, \quad (5.2.3)$$

where  $\mathbf{x}_0 \in \Delta_0$  and  $\mathbf{x}_m \in \Delta_m$ . We aim to solve the periodic functions  $\phi(\mathbf{x}_j)$  and  $w(\mathbf{x}_j)$ ,  $\mathbf{x}_j \in \Delta_j$ . We apply the same BEM scheme to solve for  $\phi(\mathbf{x}_j)$ . This is done by writing it into a boundary integral equation similar to (2.3.3).

$$\phi(\mathbf{x}_j) = \phi^{In}(\mathbf{x}_j) + \sum_{m=-\infty}^{\infty} \int_{\Delta_m} G(\mathbf{x}_j; \boldsymbol{\xi}_m) \left[ k\phi(\boldsymbol{\xi}_m) + i\sqrt{k}w(\boldsymbol{\xi}_m) \right] d\boldsymbol{\xi}_m \quad (5.2.4)$$

where  $G(\mathbf{x}_j; \boldsymbol{\xi}_m)$  is the free-surface Green's function (2.3.13) with the source point  $\boldsymbol{\xi}_m = (\xi_0, \eta_0 + ml)$  and  $(\xi_0, \eta_0) \in \Delta_0$ . Using (5.2.2) and (5.2.3) the following is true

$$\int_{\Delta_m} G(\mathbf{x}_j; \boldsymbol{\xi}_m) f(\boldsymbol{\xi}_m) d\boldsymbol{\xi}_m = \int_{\Delta_m} G(\mathbf{x}_j; \boldsymbol{\xi}_m) f(\boldsymbol{\xi}_0) d\boldsymbol{\xi}_m e^{im\sigma l}.$$

Thus by writing  $\phi(\mathbf{x}_j) = \phi(\mathbf{x}_0) e^{ij\sigma l}$  (5.2.4) becomes

$$\phi(\mathbf{x}_0) e^{ij\sigma l} = \phi^{In}(\mathbf{x}_0) e^{ij\sigma l} + \sum_{m=-\infty}^{\infty} \mathbf{G} \left[ k\phi(\mathbf{x}_j) + i\sqrt{k}w(\mathbf{x}_j) \right] e^{im\sigma l}, \quad (5.2.5)$$

where

$$\mathbf{G}f(\mathbf{x}_j) = \int_{\Delta_m} G(\mathbf{x}_j; \boldsymbol{\xi}_m) f(\boldsymbol{\xi}_0) d\boldsymbol{\xi}_m e^{im\sigma l}.$$

Note that (5.2.5) is a Fourier series that represents the spectrum of the scattered waves. Moreover the subscript  $m$  (or  $j$ ) indicates the *order of the diffraction*. For the time being our periodic line-array has an infinite diffraction order. Later we will show that we can truncate the order into a finite one in order to find the diffracted waves. The diffraction orders are crucial to determine these waves.

We are interested in the terms corresponding to  $\Delta_0$  because the scattering due to this order dominates the scattered wave spectrum (5.2.5) [Scott, 1998]. We let  $j = 0$  and drop the subscript 0 altogether to give us the boundary integral equation for the potential of the water under the periodic line-array of plates

$$\phi(\mathbf{x}) = \phi^{In}(\mathbf{x}) + k\mathbf{G}_P\phi(\mathbf{x}) + i\sqrt{k}\mathbf{G}_Pw(\mathbf{x}), \quad (5.2.6)$$

where the integral operator  $\mathbf{G}_P$  acting on function  $f(\mathbf{x})$  is

$$\mathbf{G}_P f(\mathbf{x}) = \int_{\Delta} G_P(\mathbf{x}; \boldsymbol{\xi}) f(\boldsymbol{\xi}) d\xi, \quad (5.2.7)$$

with kernel

$$G_P(\mathbf{x}; \boldsymbol{\xi}) = \sum_{m=-\infty}^{\infty} G(\mathbf{x}; \boldsymbol{\xi}_m) e^{im\sigma l}, \quad (5.2.8)$$

where  $G(\mathbf{x}; \boldsymbol{\xi}_m)$  is the free-surface green's function. We call (5.2.7) the periodic Green's integral equation with the kernel (5.2.8) the *near-field periodic Green's function*.

### 5.3 The Far-field Approximation of the Periodic Green's function

Unlike the single plate problem where the response of the plate is the interest, for the periodic line-array problem we are interested in calculating the scattering by the line-array. Hence in this section we present the approximation of the Green's function at the far field. This is particularly useful to calculate the scattered waves.

At large distance from the infinite line-array of plates, the field point can only 'vary' in the  $x$ -direction (this is because the  $y$ -direction has been covered by the infinitely long string-like array of plates). When  $|x - \xi| \rightarrow \infty$  we may use the asymptotic approximation of the Green's function

$$G(\mathbf{x}; \boldsymbol{\xi}) = -\frac{ik}{2} H_0(k|\mathbf{x} - \boldsymbol{\xi}|), \quad (5.3.1)$$

([Abramowitz & Stegun, 1964], [Linton, 1998], [Jorgenson & Mitra, 1990]). The details of (5.3.1) is given in Appendix D.

Substituting (5.3.1) into (5.2.8) gives us the *far-field periodic Green's function*

$$G_{\mathbf{P}}(\mathbf{x}; \boldsymbol{\xi}) = -\frac{ik}{2} \sum_{m=-\infty}^{\infty} H_0 \left( k [X^2 + Y_m^2]^{\frac{1}{2}} \right) e^{im\sigma l}, \quad (5.3.2)$$

where

$$\begin{aligned} X &= x - \xi, \\ Y_m &= Y - ml = (y - \eta) - ml. \end{aligned}$$

Both expressions (5.2.8) and (5.3.2) are also known as the *spatial representation of the periodic Green's function*.

We transform the periodic function (5.3.2) in the spatial domain into its equivalent function in the spectral domain using the Fourier transform plus the Poisson transformation ([Linton, 1998], [Jorgenson & Mittra, 1990], [Singh et al., 1990]). The procedure is described in Appendix D. The result is the *spectral representation of the periodic Green's function*

$$G_{\mathbf{P}}(\mathbf{x}; \boldsymbol{\xi}) = -\frac{k}{l} \sum_{m=-\infty}^{\infty} \frac{e^{-U_m |X|} e^{i\sigma_m Y}}{U_m}, \quad (5.3.3)$$

where

$$\sigma_m = \sigma + \frac{2\pi m}{l}, \quad (5.3.4)$$

and

$$\begin{aligned} U_m &= [\sigma_m^2 - k^2]^{\frac{1}{2}} \\ &= -i [k^2 - \sigma_m^2]^{\frac{1}{2}}. \end{aligned} \quad (5.3.5)$$

We call  $\sigma_m$  the *propagation constant in the y-direction* and  $iU_m$  the *propagation constant in the x-direction*. Expression (5.3.3) is also known as the Fourier Transform of (5.3.2).

## 5.4 Accelerating the periodic Green's function

In this section we present a method to accelerate the convergence of the periodic Green's function. We recap the discussion of the periodic Green's function by recalling the three

crucial representations of the Green's function. The first one is equation (5.2.8), the spatial representation of the periodic Green's function in the near field. For  $|X| \rightarrow \infty$  we have the second spatial representation for the periodic Green's function (5.3.1) which now is in the far field. Finally (5.3.3) is the spectral representation of the periodic Green's function.

The near-field periodic Green's function (5.2.8) converges very slowly for any combination of source and field points [Jorgenson & Mittra, 1990]. The spatial representation of the far-field periodic Green's function (5.3.1) converges slightly better than the near-field one for  $|X| \rightarrow \infty$  but becomes slow-convergent like (5.2.8) as it approaches  $|X| = 0$  [Linton, 1998]. On the other hand the spectral representation of the periodic Green's function (5.3.3) is rapidly converging as we increase  $m$  provided that  $|X| \neq 0$ . However the spectral form becomes slow-convergent as it approaches  $|X| = 0$  and, in some cases, it fails to converge [Jorgenson & Mittra, 1990]. Not that, for  $|X| \sim 0$ , the far-field periodic Green's function is not a valid approximation. Nevertheless this does not imply the invalidity of the accelerated Green's function.

The reason why the two domain representations of the periodic Green's function behave in such a way is because the convergence of the spatial domain representation depends on the convergence of its asymptotic form while the spectral domain representation depends on its singularity in the spatial domain. We notice that the asymptotic form of the spatial domain representation of  $G_p$  is our far-field periodic Green's function (5.3.1). Therefore, to achieve faster convergence, we must remove this asymptotic behaviour [Jorgenson & Mittra, 1990]. This is done by the Kummer's transformation [Singh et al., 1990].

We also observe that the spectral representation of the periodic Green's function (5.3.3) is singular for  $U_m = 0$ . Yet this is inevitable in the spatial representation of the far-field periodic Green's function (5.3.1), where this spectral form originated. This is why the far-field  $G_p$  (5.3.1) is slow-convergent everywhere in the spatial domain. Conversely the far-field  $G_p$  is singular at  $|X| = 0$  (with the understanding that  $|Y + ml| \rightarrow \infty$  since the line-array is infinite). This implies that its spectral representation (5.3.3) is slow-convergent at this point. However this slow-convergent problem can be avoided by slightly moving the field points. This will be shown as we work through the accelerating process.

We now apply the Kummer's transformation [Singh et al., 1990] to accelerate the periodic Green's function. The transformation is performed in the following way. Symbolically we represent the slowly convergent near-field periodic Green's function (5.2.8) by a function that depends on the number of terms in the summation  $m$

$$G_{\mathbf{P}}(\mathbf{x}; \boldsymbol{\xi}) = \sum_{m=-\infty}^{\infty} s(m). \quad (5.4.1)$$

Then we remove its asymptotic behaviour by subtracting it from the summation and add it back as a different summation. An asymptotically equivalent function for  $s(m)$  is denoted by  $\hat{s}(m)$ . The result of extracting and adding back the asymptotic part is

$$G_{\mathbf{P}}(\mathbf{x}; \boldsymbol{\xi}) = \sum_{m=-\infty}^{\infty} [s(m) - \hat{s}(m)] + \sum_{n=-\infty}^{\infty} \hat{s}(n).$$

The first summation now converges faster everywhere in the spatial domain since we have removed the asymptotic behaviour. The second summation is accelerated by replacing the function  $\hat{s}(n)$  with its spectral representation which is highly convergent

$$G_{\mathbf{P}}(\mathbf{x}; \boldsymbol{\xi}) = \sum_{m=-\infty}^{\infty} [s(m) - \hat{s}(m)] + \sum_{n=-\infty}^{\infty} \hat{S}(n), \quad (5.4.2)$$

where  $\hat{S}(n)$  is the Fourier transform of  $\hat{s}(n)$  ([Singh et al., 1990], [Jorgenson & Mittra, 1990]).

As we mentioned above, the problem that arises from (5.4.2) is the fact that the second summation converges very slowly when  $|X| = 0$ . In order for  $\hat{S}(n)$  to converge rapidly we must avoid  $|X| = 0$ . This is done by moving the field point by a small distance, say  $cl$ . This implies that we must also move the field point in the corresponding asymptotic form  $\hat{s}(m)$  by distance  $cl$ . The application of this step yields

$$G_{\mathbf{P}}(\mathbf{x}; \boldsymbol{\xi}) = \sum_{m=-\infty}^{\infty} [s(m) - \tilde{s}(m)] + \sum_{n=-\infty}^{\infty} \tilde{S}(n),$$

where  $\tilde{s}(m)$  is function  $\hat{s}(m)$  with argument  $|X + cl|$  and  $\tilde{S}(n)$  is likewise to  $\hat{S}(n)$ .

We now replace the symbolical notations  $s$ ,  $\tilde{s}$ , and  $\tilde{S}$  with our periodic Green's function. The asymptotic form of  $G(\mathbf{x}; \boldsymbol{\xi})$  is given by the Hankel function representation in the summation of the far-field  $G_{\mathbf{P}}$  (5.3.1). Using argument the  $X + cl$  we have

$$\tilde{s}(m) = -\frac{ik}{2} H_0 \left( k \left[ (X + cl)^2 + Y_m^2 \right]^{\frac{1}{2}} \right) e^{im\sigma l}. \quad (5.4.3)$$

Then the spectral representation of the far-field  $G_{\mathbf{P}}$  gives rise to

$$\tilde{S}(m) = -\frac{k e^{-U_m|X+cl|} e^{i\sigma_m Y}}{l U_m} \quad (5.4.4)$$

Finally we substitute (5.4.1), (5.4.3), and (5.4.4) into (5.4.2) to obtain the explicit formula of the accelerated periodic Green's function

$$G_{\mathbf{P}}(\mathbf{x}; \xi) = \sum_{m=-\infty}^{\infty} \left[ G(X, Y_m) + \frac{ik}{2} H_0((X + cl), Y_m) \right] e^{im\sigma l} - \frac{k}{l} \sum_{n=-\infty}^{\infty} \frac{e^{-U_n|X+cl|} e^{i\sigma_n Y}}{U_n}, \quad (5.4.5)$$

where  $G(X, Y_m)$  is given in (2.3.13). Notice that (5.4.5) is a combination of the spatial and the spectral representation of the periodic Green's function in the near and far-fields. The factor  $cl$  is the constant that 'weighs' each domain. It determines how far off we move a field point from the source (in this case the plate covered area). The free parameter  $c$  is sometimes called the smoothing factor ([Singh et al., 1990], [Jorgenson & Mittra, 1990]). This is because, apart from moving the field point, it also removes the singularity from the far-field  $G_{\mathbf{P}}$  and causes it to become a smooth function.

Note that some special combinations of wavelength  $\lambda$ , angle of incidence  $\theta$ , and length of channel  $l$  may cause the periodic Green's function to diverge ([Jorgenson & Mittra, 1990], [Scott, 1998]). An example of this case is the use of  $\lambda = l$  when the direction of propagation  $\theta = 0$ . The reason for this will be explained in the next chapter when we discuss the scattered waves.

# Chapter 6

## The Scattering of Waves by the Periodic

### Line-Array of Plates

In this chapter we observe the scattering of waves by the periodic line-array of plates. In the first section we explain the modes of scattered waves and the way to extract the travelling waves out of these modes. We then classify the scattered waves in the second section. In the third section the energy balance is calculated.

#### 6.1 The Modes of the Scattered Waves

In this section we give the modes of the scattered wave as  $|X| \rightarrow \infty$ . We are interested in the problem as  $|X| \rightarrow \infty$  therefore we extract the exponential terms from (5.3.3)

$$e^{-U_m |X|} e^{i\sigma_m Y},$$

and consider only  $\exp(i(iU_m)|X|)$ . We purposely write the term corresponding to  $U_m$  in this way so that it matches the term  $\exp(i\sigma_m Y)$ . From equation (5.3.5) if  $U_m$  is a real number then this term decays as  $|X| \rightarrow \infty$  (we shall refer this as the *evanescent modes*). Otherwise for purely imaginary  $U_m$  the term  $\exp(U_m |X|)$  yields the *propagating modes*.

To determine the propagating modes for (5.3.3) we rewrite equation (5.3.5) as

$$U_m = -ik \left[ 1 - \left( \frac{\sigma_m}{k} \right)^2 \right]^{1/2},$$

and notice that

$$U_0 = -ik \cos \theta, \tag{6.1.1}$$

since  $\sigma_0 = k \sin \theta$ . The term  $\exp(i(iU_0)|X|)$  clearly represents a traveling wave in the  $x$ -direction. This implies that at large  $|X|$  there is at least one propagating mode corresponding to the propagation constant  $\sigma_0 = \sigma$ .

Our objective in this section is to seek other propagation modes apart from the one corresponding to order 0. To do this we need to obtain  $iU_m$  that are real numbers, i.e.  $U_m$  must be purely imaginary numbers. We seek for the non-negative integers (orders)  $M$  and  $N$  such that  $U_{-M}$  and  $U_N$  are purely imaginary numbers (corresponding to the propagating modes) and  $U_{-M-1}$  and  $U_{N+1}$  are real numbers (corresponding to the evanescent modes). This way we may truncate the spectral domain representation of the periodic Green's function (5.3.3) to a finite sum

$$G_P(\mathbf{x}; \boldsymbol{\xi}) = -\frac{i}{l} \sum_{m=-M}^N \frac{e^{ik\mu_m|X|} e^{i\sigma_m Y}}{\mu_m}, \quad (6.1.2)$$

where

$$\mu_m = \left[ 1 - \left( \frac{\sigma_m}{k} \right)^2 \right]^{1/2}. \quad (6.1.3)$$

Notice that we can relate the propagation constant in the  $x$ -direction  $iU_m$  to  $\mu_m$  by

$$iU_m = k\mu_m, \quad (6.1.4)$$

and  $\mu_m > 0$ .

Such integers  $M$  and  $N$  are found to be ones that satisfy the following inequalities

$$\left. \begin{array}{l} \sigma_{-M-1} < -k < \sigma_{-M}, \\ \sigma_N < k < \sigma_{N+1}. \end{array} \right\} \quad (6.1.5)$$

An algebraic simplification of (6.1.5) gives the lower limit  $M$  to be in the range

$$\frac{l}{2\pi} \left( \sigma + k - \frac{2\pi}{l} \right) < M < \frac{l}{2\pi} (\sigma + k), \quad (6.1.6)$$

and the upper limit  $N$  to be in the range

$$\frac{l}{2\pi} (k - \sigma) > N > \frac{l}{2\pi} \left( k - \sigma - \frac{2\pi}{l} \right), \quad (6.1.7)$$

[Linton, 1998]. We call the limits  $M$  the *lower diffraction order* and  $N$  the *upper diffraction order* because of the location where the waves are 'generated' (with respect to  $\Delta_0$ ). Note that the total number of the scattered waves is equal to the diffracted waves plus one

propagating wave corresponding to mode 0. Therefore we have reduced the order of diffraction from an infinite order to a finite one.

Moreover we can now explain the phenomenon in the periodic Green's function that diverges for  $l = \lambda$  and  $\theta = 0$ . From (6.1.2) we notice that the periodic Green's function becomes singular whenever  $\mu_m = 0$ ,  $m \in \mathbb{Z}$ . For  $m = 0$ , the periodic Green's function becomes convergent if the combination of  $\lambda$ ,  $l$ , and  $\theta$  satisfies either one or both of the following equalities

$$\lambda = l(1 + \sin \theta), \quad (6.1.8)$$

and

$$\lambda = l(1 - \sin \theta). \quad (6.1.9)$$

For  $m \neq 0$  the combination of  $l$ ,  $\lambda$ ,  $\theta$ , and  $m$  that satisfies either of these equations

$$m\lambda = -l(1 + \sin \theta), \quad (6.1.10)$$

and

$$ml = l(1 - \sin \theta),$$

cause (6.1.2) to diverge. Clearly we see that for  $\theta = 0$  and  $l = \lambda$  both equalities (6.1.8) and (6.1.9) are satisfied and this explains why the periodic Green's function fails to converge. In general the Green's function is divergent if any of equation (6.1.8), (6.1.9), (6.1.10), and (??) is satisfied.

## 6.2 The Diffracted, Reflected, and Transmitted Waves

In this section we derive the diffracted waves that arise from the application of the finite diffraction order to the potential of the periodic line-array with infinite plates.

### 6.2.1 The Diffracted Waves

We substitute the spectral representation of the periodic Green's function with finite diffraction order (6.1.2) into the boundary integral equation for the potential (5.2.6)

$$\phi(\mathbf{x}) = \phi^{In}(\mathbf{x}) - \frac{i}{l} \int_{\Delta} \sum_{m=-M}^N \frac{e^{ik\mu_m|X|} e^{i\sigma_m Y}}{\mu_m} \left[ k\phi(\boldsymbol{\xi}) + i\sqrt{k}w(\boldsymbol{\xi}) \right] d\boldsymbol{\xi}, \quad (6.2.1)$$

where

$$\phi^{In}(\mathbf{x}) = A^{In} e^{ik(x \cos \theta + y \sin \theta)},$$

is the incident wave with amplitude  $A^{In}$ . To simplify the problem we set  $A^{In}$  to be unity. We subtract the incident wave so that we can observe the scattered wave only. The scattered wave is

$$\phi^s(\mathbf{x}) = -\frac{i}{l} \sum_{m=-M}^N \int_{\Delta} \frac{e^{ik\mu_m|X|} e^{i\sigma_m Y}}{\mu_m} \left[ k\phi(\boldsymbol{\xi}) + i\sqrt{k}w(\boldsymbol{\xi}) \right] d\boldsymbol{\xi}. \quad (6.2.2)$$

Equation (6.2.2) represents the scattered wave that remains propagating at the far-field. The scattered wave is composed of a finite spectrum of plane waves that are the results of the diffraction of finite order (with infinite number of images). Moreover the scattered waves travel in the direction opposite as well as along the direction of the incident wave. Thus we may write the scattered wave (6.2.2) in terms of its spectrum

$$\phi^s(\mathbf{x}) = \sum_{m=-M}^N \hat{\phi}_m^{\mp}(\mathbf{x}; \boldsymbol{\xi}), \quad (6.2.3)$$

where

$$\hat{\phi}_m^{\mp}(\mathbf{x}; \boldsymbol{\xi}) = -\frac{i}{l\mu_m} \int_{\Delta} e^{ik\mu_m|X|} e^{i\sigma_m Y} \left[ k\phi(\boldsymbol{\xi}) + i\sqrt{k}w(\boldsymbol{\xi}) \right] d\boldsymbol{\xi}, \quad (6.2.4)$$

represents the *diffracted waves* and the  $\mp$  sign indicates the direction of the scattered waves.

For diffracted waves that travel in the direction of  $x \rightarrow -\infty$  ( $x \ll \xi$ ) where  $|X| = |x - \xi| = \xi - x$  these are

$$\hat{\phi}_m^{-}(\mathbf{x}; \boldsymbol{\xi}) = -\frac{i}{l\mu_m} \int_{\Delta} e^{ik\mu_m\xi} e^{-i\sigma_m\eta} \left[ k\phi(\boldsymbol{\xi}) + i\sqrt{k}w(\boldsymbol{\xi}) \right] d\boldsymbol{\xi} e^{-ik\mu_m x} e^{i\sigma_m y}. \quad (6.2.5)$$

For diffracted waves that travel in the direction of  $x \rightarrow +\infty$  ( $x \gg \xi$ ) where  $|X| = |x - \xi| = x - \xi$  these are

$$\hat{\phi}_m^{+}(\mathbf{x}; \boldsymbol{\xi}) = -\frac{i}{l\mu_m} \int_{\Delta} e^{-ik\mu_m\xi} e^{-i\sigma_m\eta} \left[ k\phi(\boldsymbol{\xi}) + i\sqrt{k}w(\boldsymbol{\xi}) \right] d\boldsymbol{\xi} e^{ik\mu_m x} e^{i\sigma_m y}. \quad (6.2.6)$$

We can generalize the diffracted wave to be

$$\hat{\phi}_m^\mp(\mathbf{x}; \boldsymbol{\xi}) = A_m^\mp e^{\mp ik\mu_m x} e^{i\sigma_m y},$$

where the diffraction coefficient (the diffracted amplitude)  $A_m^\mp$  is

$$A_m^\mp = -\frac{i}{l} \frac{1}{\mu_m} \int_{\Delta} e^{\pm ik\mu_m \xi} e^{-i\sigma_m \eta} \left[ k\phi(\boldsymbol{\xi}) + i\sqrt{k}w(\boldsymbol{\xi}) \right] d\xi. \quad (6.2.7)$$

The diffracted waves propagate at various angles with respect to the normal direction of the line-array. The angle of diffraction depends on the ratio of the  $y$ -directed propagation constant  $\sigma_m$  and the  $x$ -directed propagation constant  $iU_m$

$$\psi_m^\mp = \tan^{-1} \left( \frac{\sigma_m}{\mp k\mu_m} \right), \quad (6.2.8)$$

where  $\psi_m^\mp$  is the angle of diffraction and relation (6.1.4) has been used. Notice that for  $m = 0$  we have

$$\psi_0^\mp = \mp\theta, \quad (6.2.9)$$

where  $\theta$  is the incident angle.

Figure 6.2.1. depicts the diffracted waves and their angles. The diffracted waves are generated in either the positive or the negative  $y$  region. The  $y$  regions are indicated by  $m$ . For  $m < 0$  we say that they are generated in the negative  $y$  region ( $y < 0$ ) and for  $m > 0$  they are generated in the positive  $y$  region ( $y > 0$ ). Hence the lower diffraction order  $M$  may be regarded as the number of diffracted waves generated in the negative  $y$  region and the upper diffraction order  $N$  the number of diffracted waves generated in the positive  $y$  region. Each diffracted wave is directed to either to the negative  $x$  ( $x < 0$ ) or positive  $x$  ( $x > 0$ ) direction. We say  $\phi_m^+$  is in the positive  $x$  direction and  $\phi_m^-$  is in the negative  $x$  direction.

## 6.2.2 The Reflected and the Transmitted Waves

From Section 6.1 we know that there is at least one set of propagating waves corresponding to order 0. This is because it is guaranteed that there exists at least one purely imaginary  $y$ -propagation constant  $U_0$  and its corresponding  $x$ -propagation constant  $\sigma_0$ . We use the diffraction order 0 to deduce the reflected and the transmitted waves. This is done by

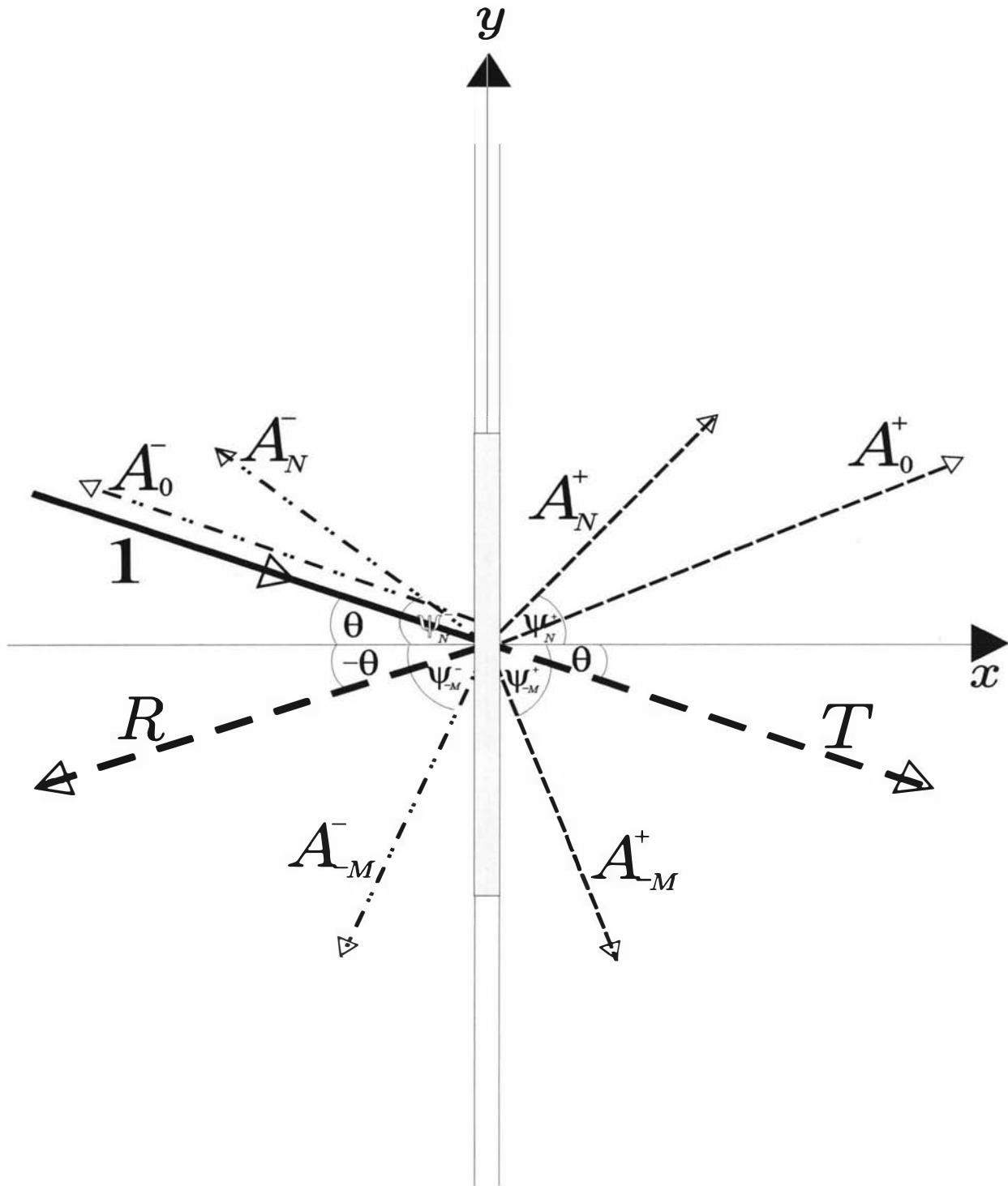


Figure 6.2.1. The diagram showing the diffracted waves and the angles of diffraction.

taking  $m = 0$  in (6.2.4)

$$\hat{\phi}_0^\mp(\mathbf{x}; \boldsymbol{\xi}) = A_0^\mp e^{\mp ik\mu_0 x} e^{i\sigma_0 y}, \quad (6.2.10)$$

where the zero order diffraction coefficient is

$$A_0^\mp = -\frac{i}{l} \frac{1}{\mu_0} \int_{\Delta} e^{\pm ik\mu_0 \xi} e^{-i\sigma_0 \eta} \left[ k\phi(\boldsymbol{\xi}) + i\sqrt{k}w(\boldsymbol{\xi}) \right] d\boldsymbol{\xi}, \quad (6.2.11)$$

and the corresponding propagation constants are

$$\sigma_0 = k \sin \theta,$$

$$\mu_0 = \cos \theta.$$

The diffraction coefficient may be further separated into

$$A_0^- = -\frac{i}{l} \frac{1}{\cos \theta} \int_{\Delta} e^{ik\xi \cos \theta} e^{-ik\eta \sin \theta} \left[ k\phi(\boldsymbol{\xi}) + i\sqrt{k}w(\boldsymbol{\xi}) \right] d\boldsymbol{\xi},$$

which is the diffraction coefficient for the wave travelling in the negative  $x$  direction ( $x < 0$ ) and

$$A_0^+ = -\frac{i}{l} \frac{1}{\cos \theta} \int_{\Delta} e^{-ik\xi \cos \theta} e^{-ik\eta \sin \theta} \left[ k\phi(\boldsymbol{\xi}) + i\sqrt{k}w(\boldsymbol{\xi}) \right] d\boldsymbol{\xi},$$

which is the diffraction coefficient for the wave travelling in the positive  $x$  direction ( $x \geq 0$ ).

The reflected wave is the diffracted wave that travels in the opposite direction to the incident wave and thus it can be written as

$$\phi^R(\mathbf{x}) = R e^{-ikx \cos \theta} e^{iky \sin \theta}, \quad (6.2.12)$$

where  $R$  is the reflection coefficient and given in terms of the diffraction coefficient which is negative  $x$ -directed

$$\begin{aligned} R &= A_0^- \\ &= -\frac{i}{l} \frac{1}{\mu_0} \int_{\Delta} e^{ik(\xi \cos \theta - \eta \sin \theta)} \left[ k\phi(\boldsymbol{\xi}) + i\sqrt{k}w(\boldsymbol{\xi}) \right] d\boldsymbol{\xi}. \end{aligned} \quad (6.2.13)$$

The transmitted wave is composed of the diffracted wave that travels in the same direction as the incident wave plus the incident wave itself

$$\begin{aligned} \phi^T(\mathbf{x}) &= \phi^{In}(\mathbf{x}) + \hat{\phi}_0^+(\mathbf{x}; \boldsymbol{\xi}) \\ &= T e^{ik(x \cos \theta + y \sin \theta)} \end{aligned} \quad (6.2.14)$$

where  $T$  is the transmission coefficient and it is given in terms of the diffraction coefficient which is positive  $x$ -directed

$$\begin{aligned} T &= 1 + A_0^+ \\ &= 1 - \frac{i}{l} \frac{1}{\mu_0} \int_{\Delta} e^{-ik(\xi \cos \theta + \eta \sin \theta)} \left[ k\phi(\xi) + i\sqrt{k}w(\xi) \right] d\xi. \end{aligned} \quad (6.2.15)$$

### 6.3 The Energy Balance

In this section we derive the energy balance yield by the diffracted, the reflected, and the transmitted waves. The diffraction, the reflection, and the transmission coefficients must satisfy the energy flux equation which simply says that the energy of the incoming wave must equal to the energy of the outgoing waves.

To derive the energy balance equation first we ‘project’ all waves in Figure 6.2.1. onto the  $x$ -axis. This gives us the projected incident coefficient  $\cos \theta$  (where the amplitude of the incident wave is 1), the reflection coefficient  $|R|^2 \cos(-\theta)$ , and the transmission coefficient  $|T|^2 \cos \theta$ . Moreover the diffraction coefficients are  $|A_m^-|^2 \cos(-\psi_m)$  and  $|A_m^+|^2 \cos \psi_m$ . The total energy is taken as the sum of the coefficients of the reflected, the transmitted, and the diffracted waves generated in both  $y$  regions

$$E = (|R|^2 + |T|^2) \cos \theta + \sum_{m=-M}^{-1} \left( |A_m^-|^2 + |A_m^+|^2 \right) \cos \psi_m + \sum_{m=1}^N \left( |A_m^-|^2 + |A_m^+|^2 \right) \cos \psi_m \quad (6.3.1)$$

The total energy must be equal to the incoming energy due to the incident wave of unit amplitude that is incident at angle  $\theta$

$$E = \cos \theta. \quad (6.3.2)$$

Energy balance equation (6.3.2) is used to check any error that can occur in the computation of the amplitudes. In the next chapter, using this idea, we will perform this check to verify the diffraction theory that we derived in this chapter.

# Chapter 7

## Results for the Multiple Plates Model

In this chapter we present the results from the infinite line-array of periodic plates. First we test the accuracy of the results using different representation of the periodic Green's function. We do this to show that the accelerated periodic Green's function is the way to compute the subsequent results. This also enables us to choose the appropriate value of the smoothing parameter and the number of terms in the spectral and the spatial terms of the accelerated periodic Green's function. Next we test the validity of our method using a periodic line-array of joined, stiff, and unmovable plate and compare it with the two-dimensional beam whose results are known to be true. We also test the convergence of the results using different fineness of discretization in the plates. Moreover we investigate the effect of the line-array on the angular spread of the scattered waves by varying the waveangle and attenuating the wave. Then we use elastic and discrete plates to study the relationship between the wavelength, the width of the channel, and the waveangle on the diffracted waves. Finally we present plots of the plates' displacement.

### 7.1 The Convergence of the Periodic Green's Function

In this section we investigate the effect of the number of images used to represent the infinite sum in the periodic Green's function. The slow-convergent near-field, the far-field, and the accelerated periodic Green's functions are observed while we omit the test for the spectral representations of the periodic Green's function. This is because both are derived from the near-field one. The convergence of the far-field and the spectral representations are given in [Linton & Evans, 1992].

The first test is performed on the slow-convergent near- and far-field periodic Green's functions (5.2.8) and 5.3.2. We set the field point  $(x, y) = (0, 0)$  and the source point

$(\xi, \eta) = (0, 0.1)$ . The length of the channel is  $l = 1$  and the wavelength is  $\lambda = 2$  with angle of propagation  $\theta = \pi/4$ . The relative errors are given by

$$\hat{E}_{12} = \left| \frac{G_{\mathbf{P}}^{(1)} - G_{\mathbf{P}}^{(2)}}{G_{\mathbf{P}}^{(1)}} \right| \quad \text{and} \quad \hat{E}_{13} = \left| \frac{G_{\mathbf{P}}^{(1)} - G_{\mathbf{P}}^{(3)}}{G_{\mathbf{P}}^{(1)}} \right|$$

where  $G_{\mathbf{P}}^{(1)}$  is the referencing result,  $G_{\mathbf{P}}^{(2)}$  is its approximation using the near-field Green's function (5.2.8), and  $G_{\mathbf{P}}^{(3)}$  is the approximation using the far-field periodic Green's function 5.3.2. Both  $G_{\mathbf{P}}^{(2)}$  and  $G_{\mathbf{P}}^{(3)}$  are taken at various number of images while the referencing result  $G_{\mathbf{P}}^{(1)}$  is the near-field  $G_{\mathbf{P}}$  with  $10^6$  images. We choose the number of images  $10^6$  as a point of reference following a series of calculations in (5.2.8) that shows the value approaches the result using this number. Figure 7.1.1. is the loglog plot of the relative errors for both the near- and the far-field periodic Green's function. The near straight lines that represent the error for both functions indicate that the error decays exponentially as we increase the number of terms in either summation. We notice that to achieve such accuracy we need to use over  $10^4$  terms in the summation and this is ineffective in practice. Moreover the far-field periodic Green's function is actually an approximation to the near-field one and the error increases as we increase the number of terms in the summation.

Next we test the convergence of the accelerated periodic Green's function given by (5.4.5). The same parameters and the referencing results are used to calculate the relative error

$$\hat{E}_{14} = \left| \frac{G_{\mathbf{P}}^{(1)} - G_{\mathbf{P}}^{(4)}}{G_{\mathbf{P}}^{(1)}} \right|,$$

where  $G_{\mathbf{P}}^{(4)}$  is the accelerated periodic Green's function. We choose the smoothing factor  $c = 0.05$ . Later we show that this choice of  $c$  is sufficient to produce accurate answers. Figure 7.1.2. is the loglog plot of the relative errors versus the number of summation terms for the accelerated  $G_{\mathbf{P}}$ . Note that we set the number of summation terms used to calculate the spatial and the spectral part to be equal. We see that error line is sloping steeply prior to 10 terms (in each part of (5.4.5)). The error line then remains flat below  $10^{-4}$  as we increase the number of terms. This is caused by the accumulation of round-off error.

Finally we study the effect of the smoothing parameter  $c$  on the number of terms in the summations needed for convergence in both, the spatial and the spectral part of the

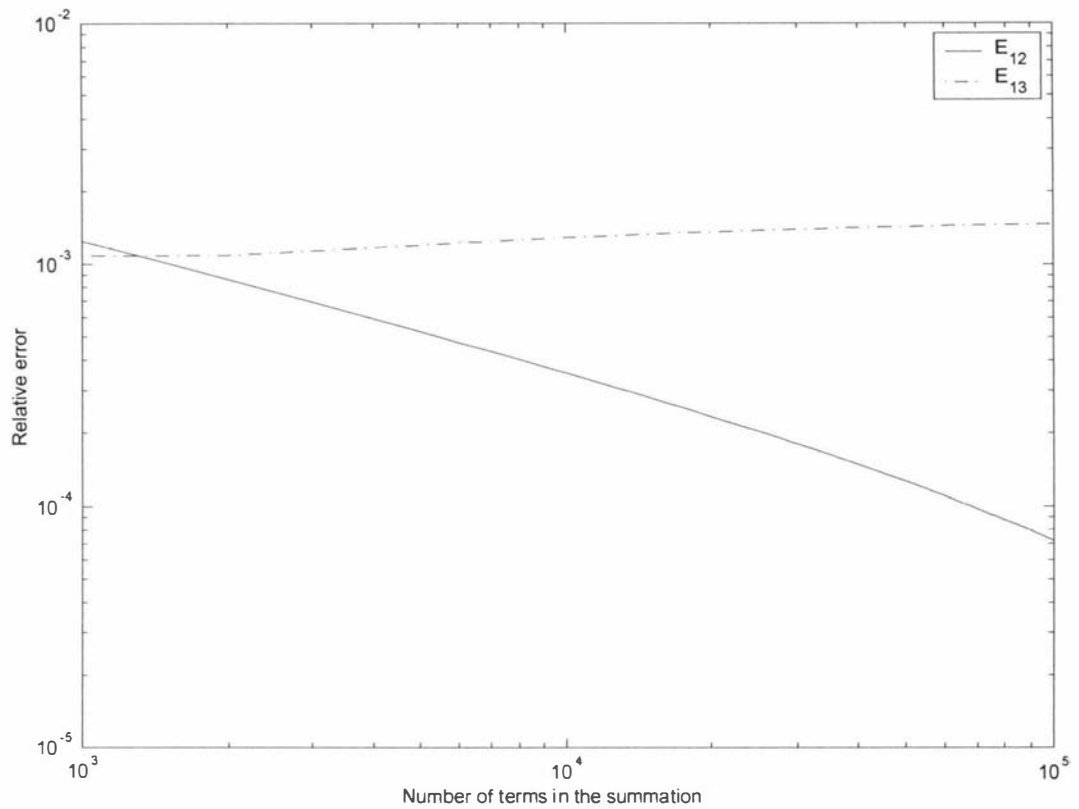


Figure 7.1.1. The loglog plot of the relative errors  $\hat{E}_{12}$  (solid line) and  $\hat{E}_{13}$  (chained line) between the near-field periodic Green's function with  $10^6$  terms  $G_{\mathbf{P}}^{(1)}$  and, respectively, the near-field  $G_{\mathbf{P}}^{(2)}$  and the far-field  $G_{\mathbf{P}}^{(3)}$  with the given number of terms. The parameters used are  $X = 0$ ,  $Y = 0.01$ , channel width  $l = 1$ , wavelength  $\lambda = 2$ , and waveangle  $\theta = \pi/4$ .

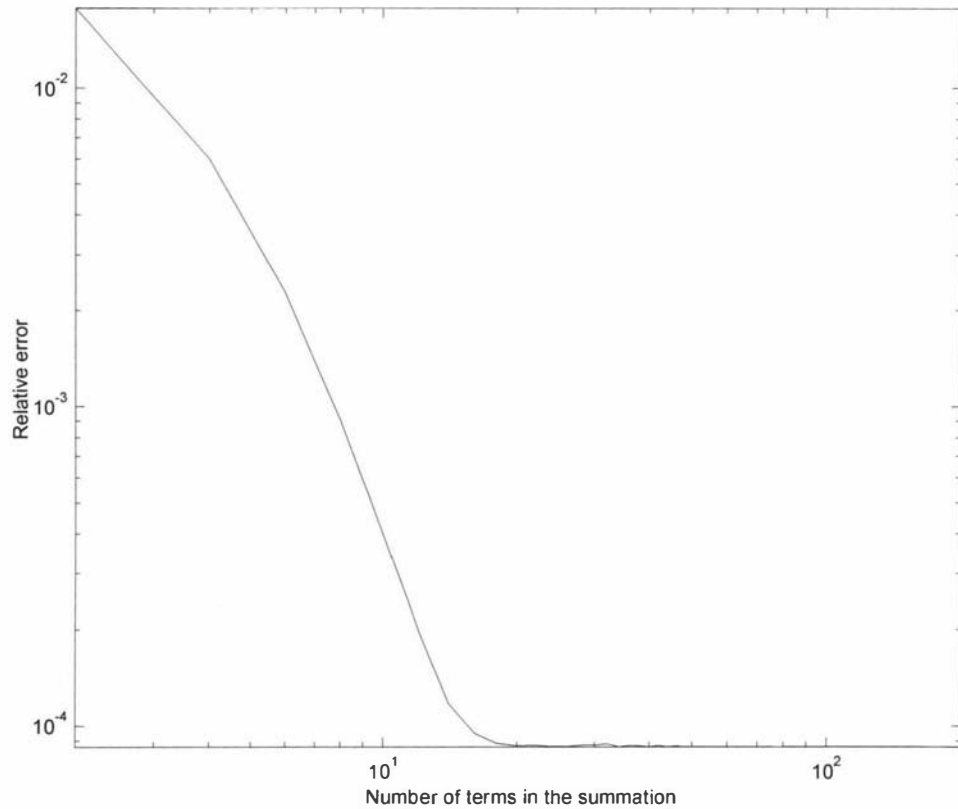


Figure 7.1.2. The loglog plot of the relative error  $\hat{E}_{14}$  between the slow convergent near-field periodic Green's function with  $10^6$  terms  $G_{\mathbf{P}}^{(1)}$  and the fast convergent  $G_{\mathbf{P}}^{(4)}$  calculated using the given number of terms. The number of spatial terms ( $m$ ) is equal to the number of the spectral terms ( $n$ ) in the summation. The smoothing factor is  $c = 0.05$ . Other parameters used are  $X = 0$ ,  $Y = 0.01$ , channel width  $l = 1$ , wavelength  $\lambda = 2$ , and waveangle  $\theta = \pi/4$ .

accelerated periodic Green's function (5.4.5). To do this we take the referencing result to be the slow-convergent periodic Green's function (5.2.8) with  $10^6$  terms. We use the same parameters as from the previous two tests. Figure 7.1.3. shows the number of terms needed by the two summations involved in the accelerated  $G_{\mathbf{P}}$  (5.4.5) versus parameter  $c$ . We set the relative error maximum at  $10^{-5}$  compared to the referencing result. We also set the absolute error between results from different combinations of parameters ( $c$ ,  $m$ , and  $n$ ) to be of maximum  $10^{-4}$ .

As shown in the plot we can obtain an accurate approximation to the infinite sum in the slow-convergent near-field  $G_{\mathbf{P}}$  using a significantly smaller number of terms in the accelerated  $G_{\mathbf{P}}$ . We also see that for a small  $c$  parameter the spectral part of the accelerated  $G_{\mathbf{P}}$  requires more summation terms than the spatial part (i.e. the spectral domain is 'heavier' than the spatial domain). Conversely for large  $c$  parameter  $G_{\mathbf{P}}$  requires more terms in the spatial part than the spectral part as the field point becomes further away from the source point and resembles a point at a far.

Note that the accelerated  $G_{\mathbf{P}}$  is not as accurate as the slow-convergent one. The function is highly accurate for small  $c$  ( $c < 0.01$ ). However, since it is 'heavier' on the spatial domain, this causes it to become slow-convergent. For large  $c$  the function is 'heavier' on its spectral part and hence it converges rapidly. Yet this gives relatively inaccurate results because, as we know, the spectral representation of the periodic Green's function is only an approximation to the desired (5.2.8).

Therefore we need to choose a  $c$  parameter where the spatial and the spectral domains weigh relatively equal. We notice that when  $c$  is approximately 0.05 then both the spatial and the spectral parts have the same 'weight'. To be precise, there are 44 terms in the spatial part and 46 terms in the spectral part of the accelerated  $G_{\mathbf{P}}$  (5.4.5) for  $c = 0.05$ . This combination of  $c$ ,  $m$ , and  $n$  will be used subsequently.

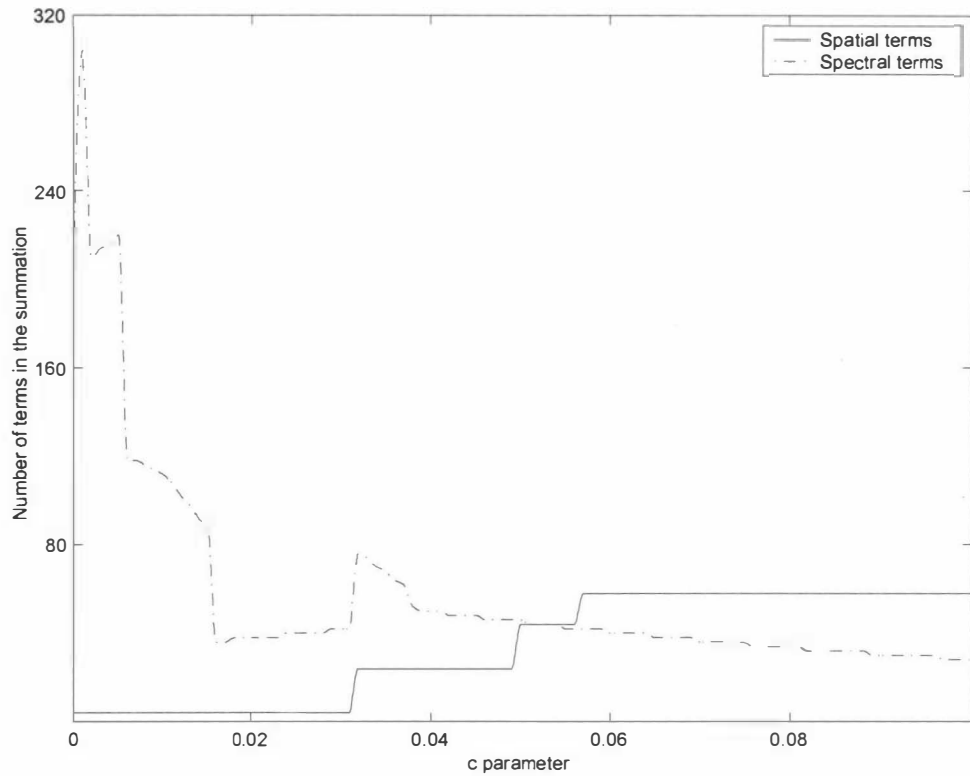


Figure 7.1.3. The plot of the number of terms used in the summation representing the spatial and the spectral parts in the accelerated periodic Green's function versus the smoothing parameter  $c$ . The result from each combination is compared with the one from slow convergent  $G_P$  with  $10^6$  terms. The relative error is set to be of maximum  $10^{-5}$ . The absolute error between results from different combination of parameters is set to be  $10^{-4}$ . The parameters used are  $X = 0$ ,  $Y = 0.01$ , channel width  $l = 1$ , wavelength  $\lambda = 2$ , and waveangle  $\theta = \pi/4$ .

## 7.2 A Periodic Line-Array of Stiff and Unmovable Plates

This section contains the testing of the periodic line-array solution. First we compare the result of a periodic line-array of joined, stiff, and unmovable plates with the result of a stiff and unmovable beam. Next we test the convergence of the solution for the energy equation (6.3.1). Finally we show the angular spread of the diffracted waves.

### 7.2.1 The Case of Joined Square Plates

In this subsection we aim to validate our results for the periodic line-array of plates. We first compare the reflection and transmission coefficients arising from the scattering problem by a line-array of stiff, unmovable, and joined (i.e. we allow no gap between) plates in three-dimensional domain to the ones yield from the problem of a stiff and unmovable beam in two-dimensional domain. The joined plates are taken to be squares of uniform area 1 ( $L = 1$ ) and this implies that the length of the channel must be  $l = 1$  and  $b = 0$ . Such arrangement of plates resembles a beam in two-dimensional domain whose length is 1. This problem was solved by Meylan ([Meylan & Squire, 1994], [Meylan, 1994]). Hence we may compare the scattered (the reflection and the transmission) coefficients due to the line-array with the ones due to a beam with length 1. We need to set the waveangle  $\theta = 0$  in the three-dimensional domain so that it resembles the incident wave in the two-dimensional domain because the two-dimensional code does not solve for waves incident at an angle. Figure.7.2.1. contains overlapping plots of the reflection and transmission coefficients from the two sets of problems. As we expect the results from both agree to the scale of the plate.

### 7.2.2 The Case of Periodical Square Plates with Gaps

We now test for the convergence of the diffracted, reflected, and transmitted waves. In the case where the length of the channel is greater than the wavelength diffraction occurs. Therefore we can calculate the diffracted waves as well as the reflected and the transmitted ones. For the following test we aim to calculate the diffraction, the reflection, and the

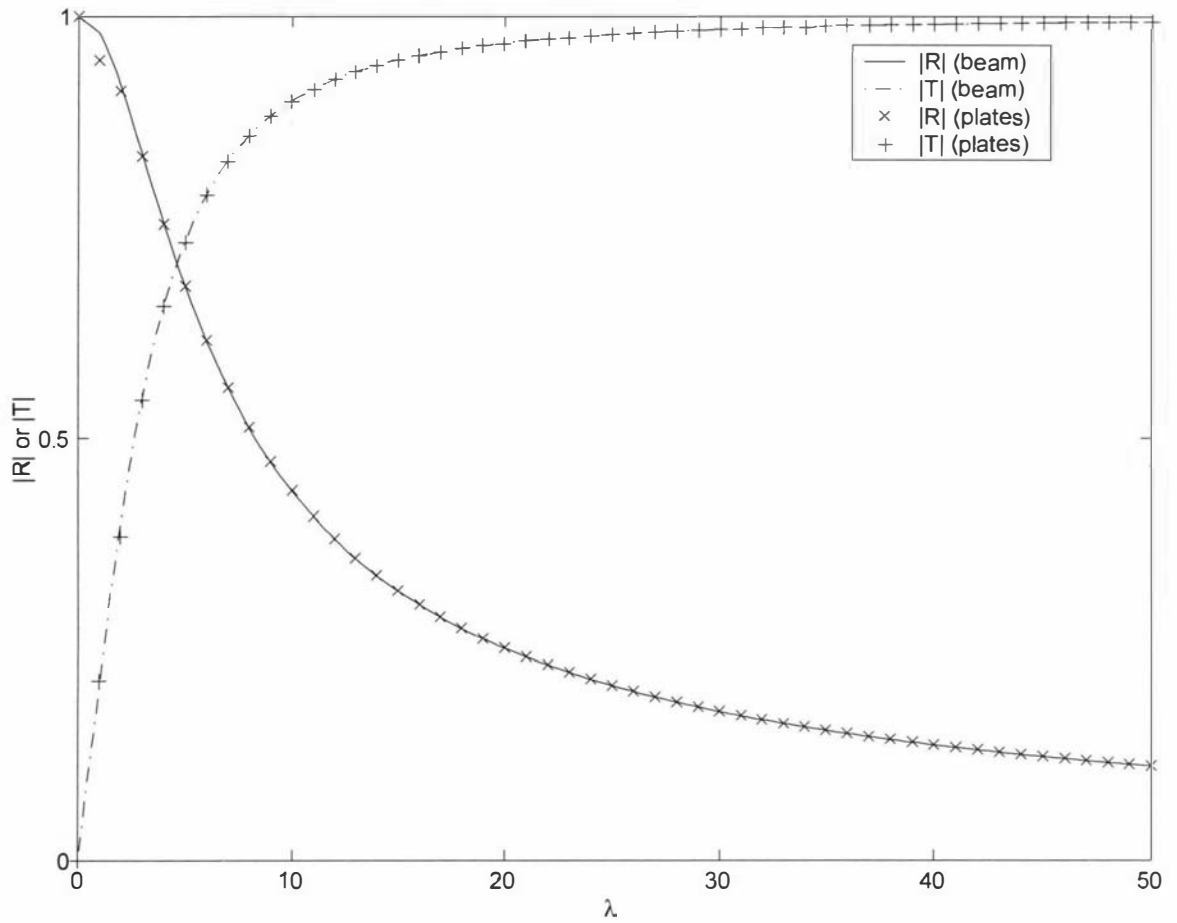


Figure 7.2.1. The comparison plot of various wavelengths versus the scattered coefficients due to a periodic array of stiff, unmovable, and joined plates in three dimensional domain and a stiff and unmovable beam in two dimensional. In the three dimensional domain the plates are squares of area 1 (side length of 1), the length of the channel is  $l = 1$  ( $b = 0$ ), and the waveangle is  $\theta = 0$ . In the two dimensional the length of the beam is 1. This figure shows the agreement in the results for the stiff, unmovable, and joined three-dimensional plates with the two-dimensional beam.

transmission coefficients. The waveangle is set to be  $\theta = 0$  so that we have symmetric diffracted waves ( $M = N$ ). The wavelength is set to be smaller than the width of the channel but not equal (to avoid the singularity that occurs at the Green's function) and greater than half  $l$ . This is done because we want to limit the number of diffracted waves on each hemisphere to be 1 pair only (or 2 by symmetry). Hence we set the ratio of the wavelength and the width of the channel to be  $\frac{\lambda}{l} = \frac{2}{3}$ . The square plates have area 16 ( $L = 4$ ), the width of the channel  $l = \frac{3}{2} \times 2L = 12$ , the length of the gap  $b = \frac{1}{8}L = 0.5$ , and the wavelength  $\lambda = 2L = 8$ . The smoothing parameter  $c = 0.05$  with 44 terms in the spatial part and 46 terms in the spectral part of  $G_{\mathbf{P}}$ . Table 7.2.1. shows the convergence of the total energy  $E$ . As stated in equation (6.3.2) the total energy must equal to  $\cos \theta$  which in this case is 1. We can see from Table 7.2.1. that indeed the total energy converges to 1 as we increase the number of panels.

### 7.2.3 The Case of Oblique Incident Wave

Next we show the spreading of the reflected, the transmitted, and the diffracted waves for a stiff square plate using various angles. We use the same plate as the previous test. The ratio of the wavelength and the width of the channel is kept at  $\frac{\lambda}{l} = \frac{2}{3}$ . However we now shorten the wavelength to be  $\lambda = L = 4$  and the width to be  $l = 6$ . This is because we want to show the effect of the plates on the angular scattering. We vary the angle using  $\theta = -\pi/3$ ,  $-\pi/6$ ,  $0$ , and  $\pi/4$ . In all cases the total diffracted waves are two pairs plus the pair of the transmitted-reflected ones. We use  $c = 0.05$  with corresponding 44 terms in the spatial part and 46 terms in the spectral part of  $G_{\mathbf{P}}$ . Figure 7.2.2 to 7.2.5 shows the angular spread of the diffracted waves while the amplitudes are explained in Table 7.2.2. to Table 7.2.5. As we expected the diffracted waves (including the reflected and the transmitted ones) come in pairs and each pair is reflected about the  $y$ -axis. We notice that the diffracted waves do not necessarily travel in the same region as where they were generated. For example, in the case of angle  $\theta = -\pi/3$  we have a diffracted wave that travels toward the negative  $y$  region despite the fact that all the waves are generated on the positive  $y$  region. The opposite

number of panels per plate	$E$
25	0.977553722824
100	0.994179825283
225	0.997487917349
400	0.999058250825

Table 7.2.1. The convergence of the total energy for identical plates with area 16. Each plate is discretized using the specified number of panels. The width of the channel is  $l = 12$ . The parameters for the incident wave are  $\lambda = 8$  and  $\theta = 0$ . The incoming energy is 1.

occurs for  $\theta = \pi/3$ . Moreover the amplitude of each of the pair differs except for the case of normal incidence. Though in these examples all incident angles produce an equal numbers of diffracted waves, in general these vary with  $\theta$ . This because the diffraction order is governed by equations (6.1.6) and (6.1.7) and hence it depends on  $\lambda$ ,  $l$ , and  $\theta$ . We will show the variation of the number of diffracted waves in the next section.

### 7.3 A Periodic Line-Array of Elastic and Separated Plates

In this section we present the results for a periodic line-array of elastic plates of five different shapes that are depicted by Figure 4.3.2. First we want to understand the relationship between the number of diffracted waves to the wavelength, the channel width, and the incident angle. Therefore we tabulate them for combinations of the three entities. Then we demonstrate the reflected, the transmitted, and the diffracted waves for various incident angles. Next we calculate the scattering of waves for different wavelength. Finally we show the displacement of the plates.

#### 7.3.1 The Dependency of the Scattered Waves to the Wavelength, the Channel Width, and the Incident Angle

In this part we show the number of diffracted waves generated by several combinations of wavelength  $\lambda$ , channel width  $l$ , and incident angle  $\theta$ . We choose to calculate  $\lambda$ ,  $l$  as the multiples of the length parameter where  $L = 4$ . Table 7.3.1. and Table 7.3.2. show the number of diffracted waves using varying  $\lambda$  and  $l$  while the incident angle is kept constant at  $\theta = 0$ . Table 7.3.3. and Table 7.3.4. show the number of diffracted waves for  $\lambda = 8$  and varying  $\lambda$  and  $\theta$  ( $\theta$  is in radians). The number of diffracted waves generated in the positive  $y$  region is shown in Table 7.3.1. for different  $l$  and  $\lambda$  and Table 7.3.3. for different  $l$  and  $\theta$ . Similarly the number of the diffracted waves generated in the negative  $y$  region is shown in Table 7.3.2. for different  $l$  and  $\lambda$  and Table 7.3.4. for different  $l$  and  $\theta$ . We note that for constant  $\lambda$  and  $l$  the number of diffracted waves varies with the magnitude of the angle.

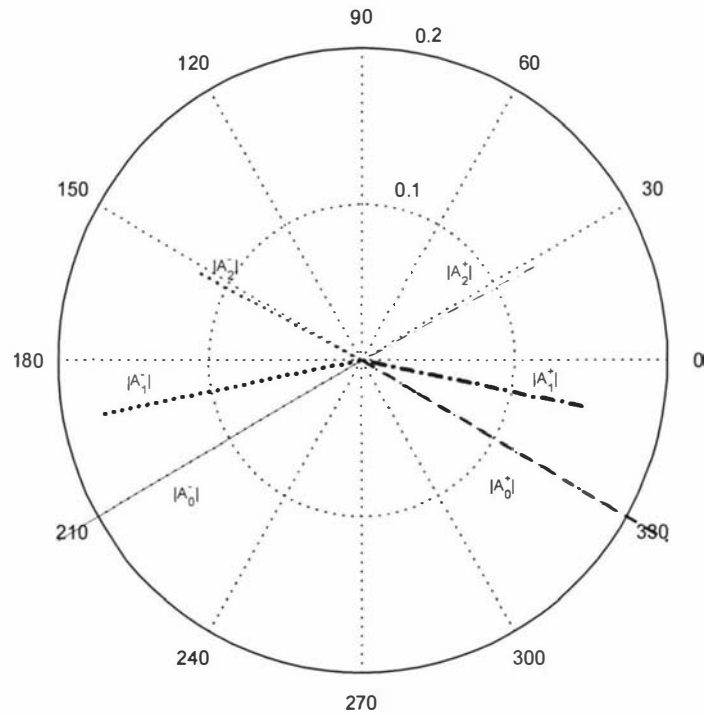


Figure 7.2.2. The scattering of waves by a periodic array of stiff and unmovable square plates where each has area 16 and is confined by channel of length  $l = 6$ . The incident wave of length  $\lambda = 4$  is oblique at angle  $\theta = -\pi/3$ . There are 3 pairs of diffracted waves of order from 0 to 4 (all are generated in the positive  $y$  region). The amplitude  $|A_m^\pm|$  of the scattered wave is shown in Table 7.2.2.

$m$	$ A_m^- $	$ A_m^+ $
0	0.878693530707	0.952919039618
1	0.176389747108	0.150918440525
2	0.123902822121	0.131191721174

Table 7.2.2. Table of the scattered amplitude  $A_m^-$  and  $A_m^+$  ( $0 \leq m \leq 2$ ) depicted by Figure 7.2.2. due to a periodic array of plates of area 16. The incident wave is oblique at angle  $\theta = -\pi/3$ . The scattered amplitudes of diffraction order  $m = 0$  represents the reflected amplitude  $R = A_0^-$  and the transmitted amplitude  $T = 1 - A_0^+$ .

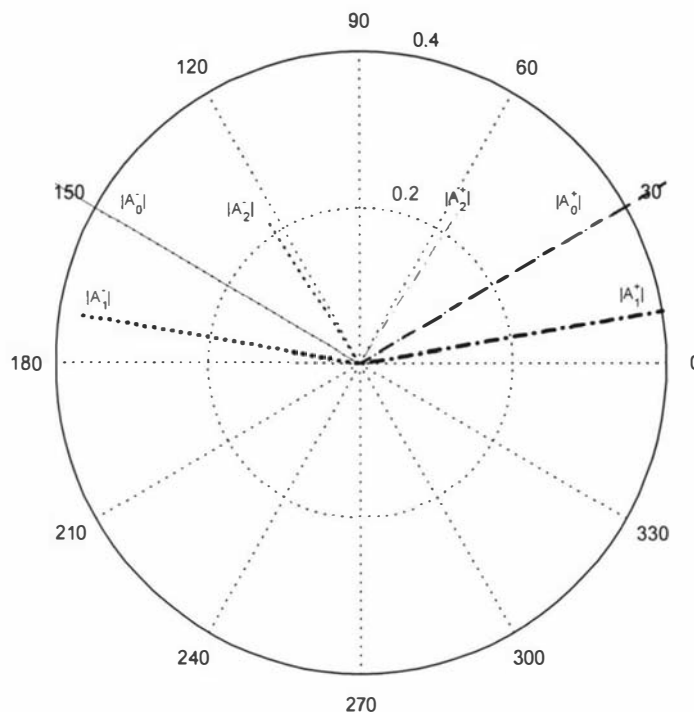


Figure 7.2.3. The scattering of waves by a periodic array of stiff and unmovable square plates where each has area 16 and is confined by channel of length  $l = 6$ . The incident wave of length  $\lambda = 4$  is oblique at angle  $\theta = -\pi/6$ . There are 3 pairs of diffracted waves of order from  $M = -1$  (one originated from the negative  $y$  region) to  $N = 3$  (three originated from the positive  $y$  region). The amplitude  $|A_m^\pm|$  of the scattered wave is shown in Table 7.2.3.

$m$	$ A_m^- $	$ A_m^+ $
0	0.666615883407	0.719311829359
1	0.376673463690	0.400750422341
2	0.217505554638	0.229435392631

Table 7.2.3. Table of the scattered amplitude  $A_m^-$  and  $A_m^+$  ( $-1 \leq m \leq 2$ ) depicted by Figure 7.2.3. due to a periodic array of plates of area 16. The incident wave is oblique at angle  $\theta = -\pi/6$ . The scattered amplitudes of diffraction order  $m = 0$  represents the reflected amplitude  $R = A_0^-$  and the transmitted amplitude  $T = 1 - A_0^+$ .

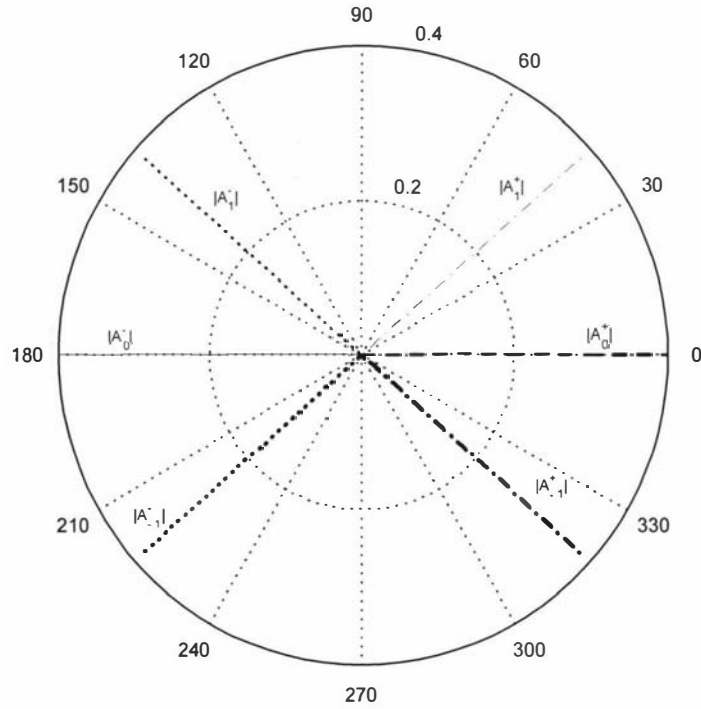


Figure 7.2.4. The scattering of waves by a periodic array of stiff and unmovable square plates where each has area 16 and is confined by channel of length  $l = 6$ . The incident wave of length  $\lambda = 4$  is oblique at angle  $\theta = 0$ . There are 3 pairs of diffracted waves of order from  $M = -2$  to  $N = 2$  (both positive and negative  $y$  regions generate two). The amplitude  $|A_m^\pm|$  of the scattered wave is shown in Table 7.2.4.

$m$	$ A_m^- $	$ A_m^+ $
-1	0.387712757032	0.386427632616
0	0.397528969357	1.025953455086
1	0.386051701291	0.386055708686

Table 7.2.4. Table of the scattered amplitude  $A_m^-$  and  $A_m^+$  ( $-1 \leq m \leq 1$ ) depicted by Figure 7.2.4. due to a periodic array of plates of area 16. The incident wave is oblique at angle  $\theta = 0$ . The scattered amplitudes of diffraction order  $m = 0$  represents the reflected amplitude  $R = A_0^-$  and the transmitted amplitude  $T = 1 - A_0^+$ .

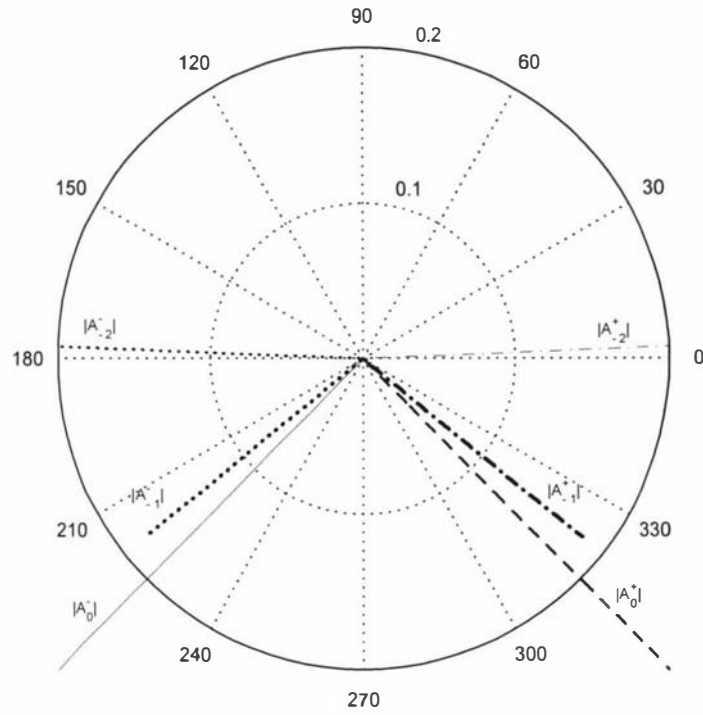


Figure 7.2.5. The scattering of waves by a periodic array of stiff and unmovable square plates where each has area 16 and is confined by channel of length  $l = 6$ . The incident wave of length  $\lambda = 4$  is oblique at angle  $\theta = \pi/4$ . There are 3 pairs of diffracted waves of order from  $M = -3$  to  $N = 0$  (all generated in the negative  $y$  region). The amplitude  $|A_m^\pm|$  of the scattered wave is shown in Table 7.2.5.

$m$	$ A_m^- $	$ A_m^+ $
-2	0.181416554036	0.182976607757
-1	0.267160755486	0.262408935043
0	0.798561389792	0.809815961605

Table 7.2.5. Table of the scattered amplitude  $A_m^-$  and  $A_m^+$  ( $-2 \leq m \leq 0$ ) depicted by Figure 7.2.5. due to a periodic array of plates of area 16. The incident wave is oblique at angle  $\theta = \pi/4$ . The scattered amplitudes of diffraction order  $m = 0$  represents the reflected amplitude  $R = A_0^-$  and the transmitted amplitude  $T = 1 - A_0^+$ .

Notice from Tables 7.3.1., 7.3.2., 7.3.3., and 7.3.4. that the number of diffracted waves generated in the positive  $y$  region is not always the ones generated in the negative  $y$  region.

### 7.3.2 The Scattering of Wave with Various Incident Angles

We calculate the scattered waves due to the line-array when the incident angle  $\theta$  varies from  $-\pi/3$  to  $\pi/3$ . The range of angle is chosen such that we are sufficiently far from the singularities at  $\theta = -\pi/2$  and  $\theta = \pi/2$ . Figures 7.3.1., 7.3.2., 7.3.3., 7.3.4., and 7.3.5. show the reflected (a), the transmitted (b), and the diffracted ((c) and (d)) amplitudes for periodic line-arrays of the shape, respectively, square, triangle, circle, parallelogram, and trapezoid. All the plates have area 16 ( $L = 4$ ), stiffness  $\beta = 0.1$ , and mass  $\gamma = 0$ . Each plate is discretized using approximately 100 panels with an exception on the square plate. The wavelength is  $\lambda = 4$  and the width of the channel is  $l = 6$  (their ratio is  $\frac{\lambda}{l} = \frac{2}{3}$ ). We use uniform  $c = 0.005$  with corresponding 44 terms in the spatial and 46 terms in the spectral part of  $G_P$ .

First we notice there are 3 pairs of diffracted waves (including the reflected-transmitted pair) for any angle and any shapes. The number of diffracted waves generated in both  $y$  regions are unsymmetric except for  $-\frac{\pi}{10} \leq \theta \leq \frac{\pi}{10}$  where  $M = N = 1$ . Then for shapes that are symmetrical about the  $y$ -axis (such as the square, the circle, and the trapezoid) the diffracted waves travelling to the negative  $x$  are equal in magnitude to the ones travelling to the positive  $x$ . We can see this by comparing the solid line (directed towards positive  $x$ , from the negative  $y$  region) to the chained line (directed towards negative  $x$ , from the negative  $y$  region) and the dotted (directed towards positive  $x$ , from the positive  $y$  region) to the dashed (directed towards negative  $x$ , from the positive  $y$  region) in part (c) and (d) of Figure 7.3.1., 7.3.3., and 7.3.5. However this is not true for the triangle (Figure 7.3.2.) and the parallelogram (Figure 7.3.4.). The reason for this is because the triangle plates and the parallelogram plates are not symmetric about  $\theta = 0$  while the square, circle, and trapezoid plates are symmetric.

		$\lambda$				
$l$		4	8	16	32	64
4		0	0	0	0	0
6		1	0	0	0	0
8		1	0	0	0	0
10		2	1	0	0	0
20		4	2	1	0	0
40		9	4	2	1	0

Table 7.3.1. The number of diffracted waves  $M$  generated in the negative  $y$  region for various  $\lambda$  and  $l$  while  $\theta = 0$ .

		$\lambda$				
$l$		4	8	16	32	64
4		0	0	0	0	0
6		1	0	0	0	0
8		1	0	0	0	0
10		2	1	0	0	0
20		4	2	1	0	0
40		9	4	2	1	0

Table 7.3.2. The number of diffracted waves  $N$  generated in the positive  $y$  region for various  $\lambda$  and  $l$  while  $\theta = 0$ . Adding the value of this table to its counter part in Table 7.3.1. gives the total number of diffracted waves for the specified  $\lambda$  and  $l$ . Both this table and Table 7.3.1. show that the variability of the diffraction waves number depends greatly on  $\lambda$  and  $l$ .

		$\theta$										
$l$		-60	-48	-36	-24	-12	0	12	24	36	48	60
4		0	0	0	0	0	0	0	0	0	0	0
6		0	0	0	0	0	0	0	1	1	1	1
8		0	0	0	0	0	0	1	1	1	1	1
10		0	0	0	0	0	1	1	1	1	2	2
20		0	0	1	1	1	2	3	3	3	4	4
40		0	1	2	2	3	4	6	7	7	8	9

Table 7.3.3. The number of diffracted waves generated in the negative  $y$  region for varying  $\theta$  and  $l$  while  $\lambda = 8$  is constant.

		$\theta$									
$l$	-60	-48	-36	-24	-12	0	12	24	36	48	60
4	0	0	0	0	0	0	0	0	0	0	0
6	1	1	1	1	0	0	0	0	0	0	0
8	1	1	1	1	1	0	0	0	0	0	0
10	2	2	1	1	1	1	0	0	0	0	0
20	4	4	3	3	3	2	1	1	1	0	0
40	9	8	7	7	6	4	3	2	2	1	0

Table 7.3.4. The number of diffracted waves generated in the positive  $y$  region for varying  $\theta$  and  $l$  while  $\lambda = 8$  is constant. Adding the values in this table to its counterpart in Table 7.3.3. gives the total number of diffracted waves for the specified  $\theta$  and  $l$ . This table and Table 7.3.3. show that the varying angle causes the number of diffracted waves to vary as well. Nevertheless the number of the diffracted waves in the opposite  $y$  regions 'moves' with the angle as it traverses about  $\theta = 0$ .

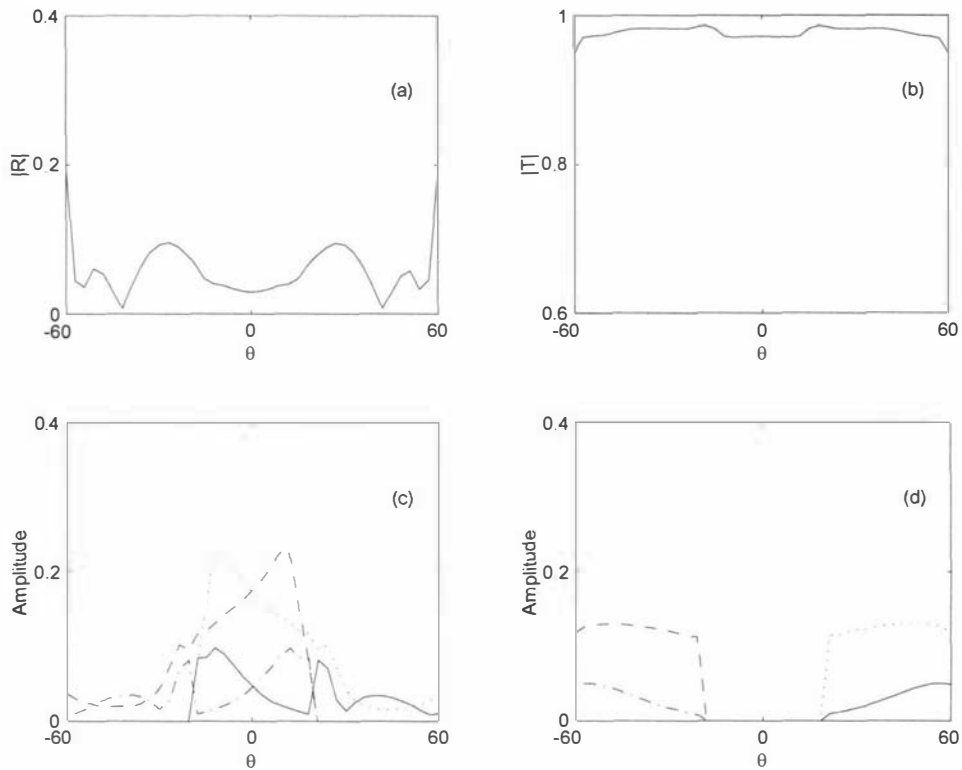


Figure 7.3.1. The scattering of waves of wavelength  $\lambda = 4$  by a periodic array of square plates of area 16, stiffness  $\beta = 0.1$ , and mass  $\gamma = 0$ . Each plate is confined by a channel of width  $l = 6$ . (a) The reflection amplitude  $|R|$  versus the incident angle  $\theta$ . (b) The transmission amplitude  $|T|$  versus the incident angle  $\theta$ . (c) The overlapping plot of the diffracted wave of order 1. (d) The overlapping plot of the diffracted wave of order 2. The waves are directed towards positive  $x$  (solid line) and negative  $x$  (chained line) in the negative  $y$  region and directed towards positive  $x$  (dotted line) and negative  $x$  (dashed line) in the positive  $y$  region. The figures show symmetry about angle  $\theta = 0$  in all the scattered waves and this is due to the symmetry of the shape of the plates and the periodic gratings.

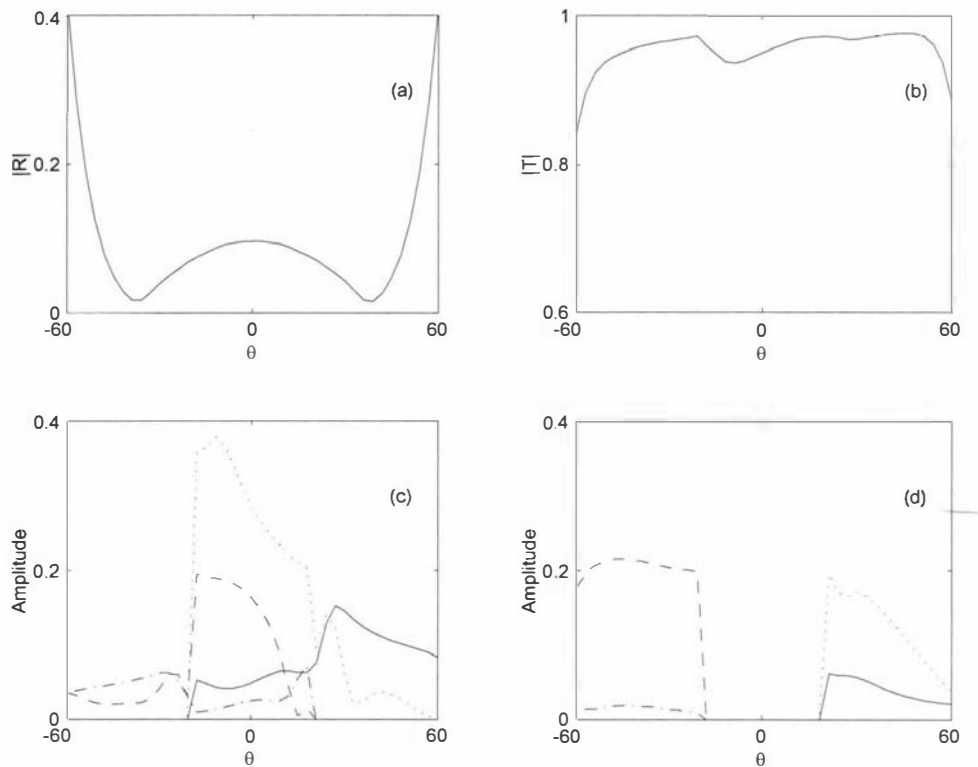


Figure 7.3.2. The scattering of waves of wavelength  $\lambda = 4$  by a periodic array of triangular plates of area 16, stiffness  $\beta = 0.1$ , and mass  $\gamma = 0$ . Each plate is confined by a channel of width  $l = 6$ . (a) The reflection amplitude  $|R|$  versus the incident angle  $\theta$ . (b) The transmission amplitude  $|T|$  versus the incident angle  $\theta$ . (c) The overlapping plot of the diffracted wave of order 1. (d) The overlapping plot of the diffracted wave of order 2. The waves are directed towards positive  $x$  (solid line) and negative  $x$  (chained line) in the negative  $y$  region and directed towards positive  $x$  (dotted line) and negative  $x$  (dashed line) in the positive  $y$  region. The scattered waves are not symmetric about  $\theta = 0$  because the shape of the plates are not symmetric.

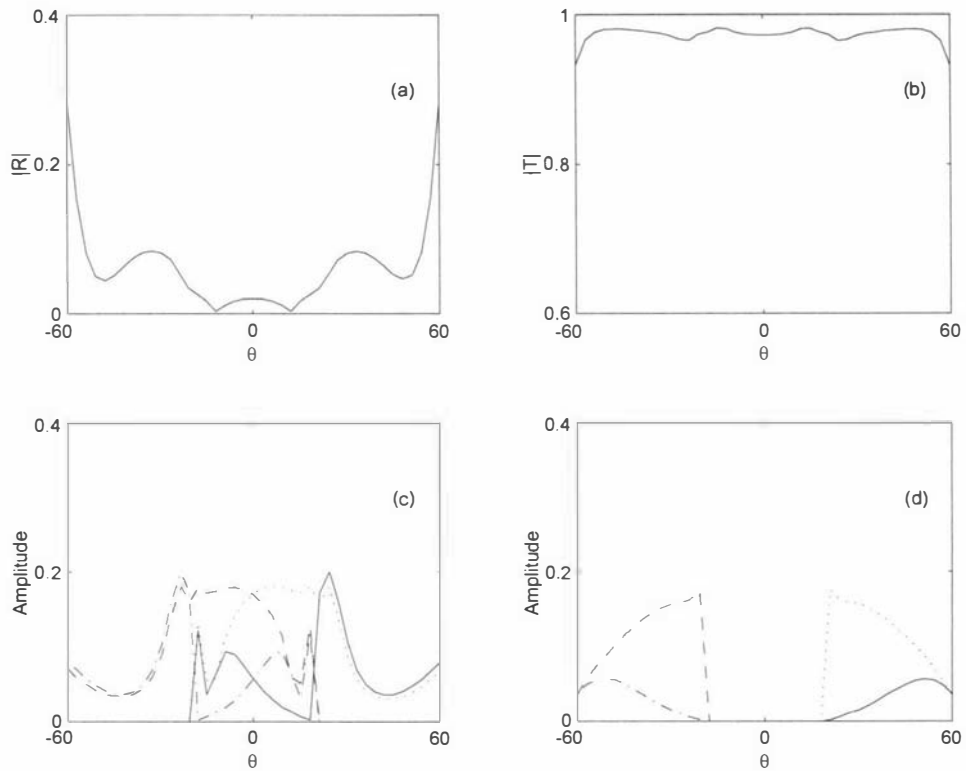


Figure 7.3.3. The scattering of waves of wavelength  $\lambda = 4$  by a periodic array of circle plates of area 16, stiffness  $\beta = 0.1$ , and mass  $\gamma = 0$ . Each plate is confined by a channel of width  $l = 6$ . (a) The reflection amplitude  $|R|$  versus the incident angle  $\theta$ . (b) The transmission amplitude  $|T|$  versus the incident angle  $\theta$ . (c) The overlapping plot of the diffracted wave of order 1. (d) The overlapping plot of the diffracted wave of order 2. The waves are directed towards positive  $x$  (solid line) and negative  $x$  (chained line) in the negative  $y$  region and directed towards positive  $x$  (dotted line) and negative  $x$  (dashed line) in the positive  $y$  region. The figures show symmetry about angle  $\theta = 0$  in all the scattered waves and this is due to the symmetry of the shape of the plates and the periodic gratings.

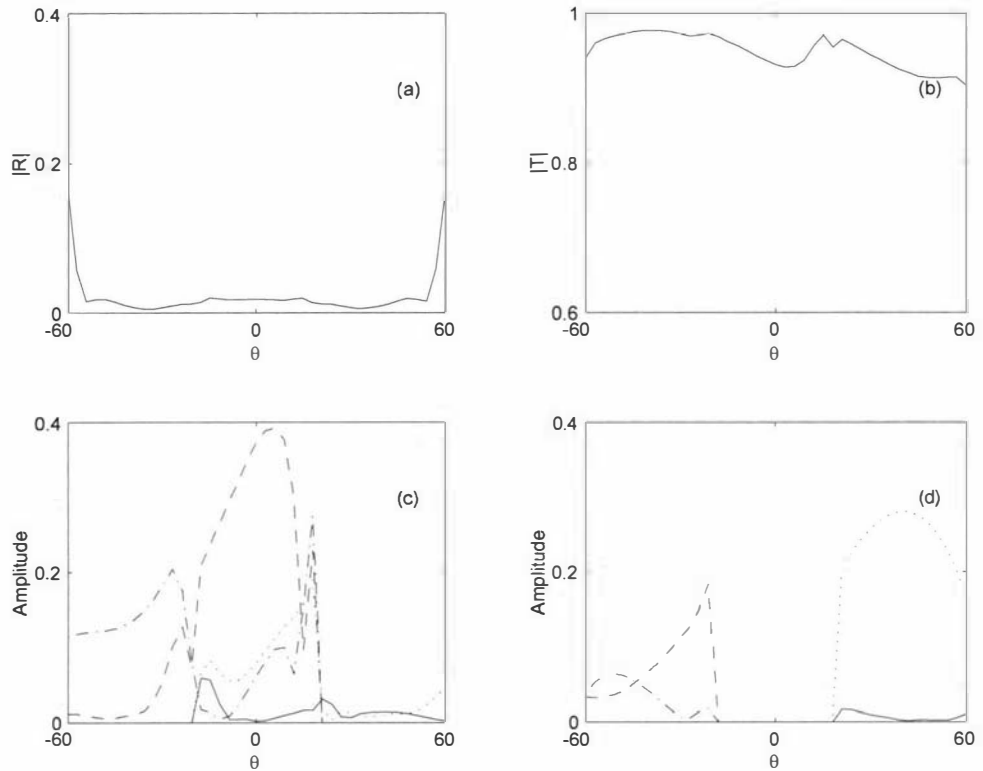


Figure 7.3.4. The scattering of waves of wavelength  $\lambda = 4$  by a periodic array of parallelogram plates of area 16, stiffness  $\beta = 0.1$ , and mass  $\gamma = 0$ . Each plate is confined by a channel of width  $l = 6$ . (a) The reflection amplitude  $|R|$  versus the incident angle  $\theta$ . (b) The transmission amplitude  $|T|$  versus the incident angle  $\theta$ . (c) The overlapping plot of the diffracted wave of order 1. (d) The overlapping plot of the diffracted wave of order 2. The waves are directed towards positive  $x$  (solid line) and negative  $x$  (chained line) in the negative  $y$  region and directed towards positive  $x$  (dotted line) and negative  $x$  (dashed line) in the positive  $y$  region. The scattered waves are not symmetric about  $\theta = 0$  because the shape of the plates are not symmetric.

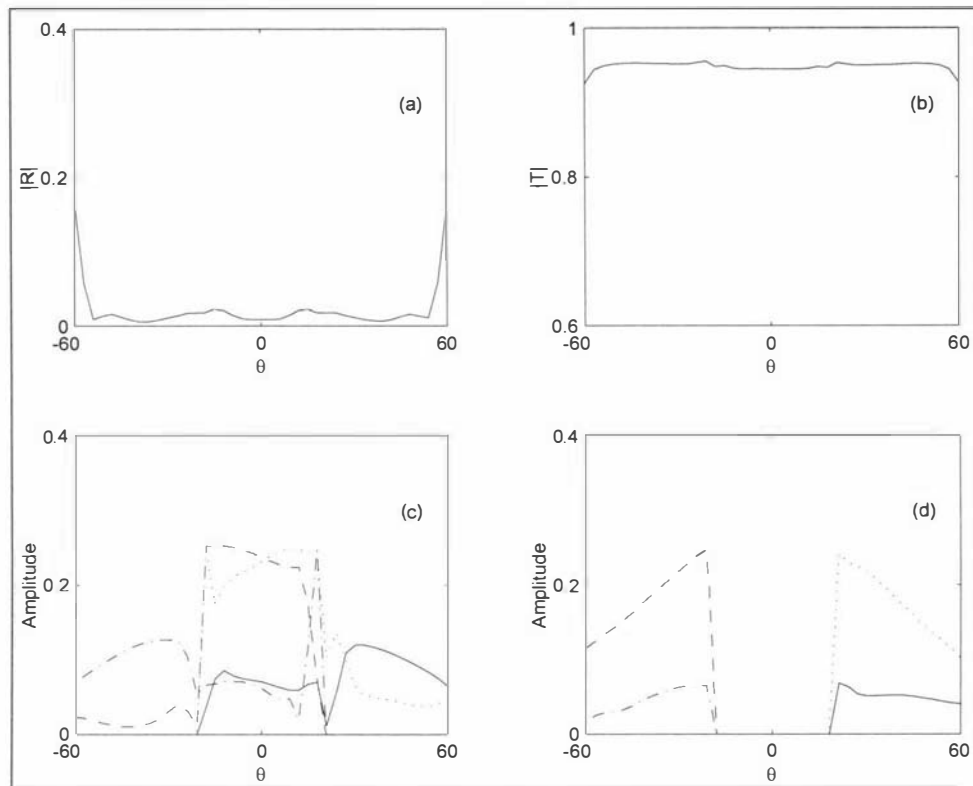


Figure 7.3.5. The scattering of waves of wavelength  $\lambda = 4$  by a periodic array of trapezoidal plates of area 16, stiffness  $\beta = 0.1$ , and mass  $\gamma = 0$ . Each plate is confined by a channel of width  $l = 6$ . (a) The reflection amplitude  $|R|$  versus the incident angle  $\theta$ . (b) The transmission amplitude  $|T|$  versus the incident angle  $\theta$ . (c) The overlapping plot of the diffracted wave of order 1. (d) The overlapping plot of the diffracted wave of order 2. The waves are directed towards positive  $x$  (solid line) and negative  $x$  (chained line) in the negative  $y$  region and directed towards positive  $x$  (dotted line) and negative  $x$  (dashed line) in the positive  $y$  region. The figures show symmetry about angle  $\theta = 0$  in all the scattered waves and this is due to the symmetry of the shape of the plates and the periodic gratings.

### 7.3.3 The Displacement of the Plates

We now show the displacement of the plates of various shapes that are part of the periodic line-array. We only use five plates ( $\Delta_j$ ,  $j = -2, -1, 0, 1, 2$ ) to represent the line-array in the plot, where each has area 16 ( $L = 4$ ), stiffness  $\beta = 0.1$ , and  $\gamma = 0$ . The width of the channel is  $l = 6$ . We expose the line-array to an incident wave that is oblique at angle  $\theta = \pi/6$ . Figures 7.3.6. to 7.3.10. show the displacement of, respectively, squares, triangles, circles, parallelograms, and trapezoids. First we use wavelength  $\lambda = 4$  (a) and then we double it to  $\lambda = 8$  (b). For  $\lambda = 4$  we have, uniformly for all shapes, 3 diffracted waves generated in the negative  $y$  region ( $M = -3$ ) and 1 generated in the positive  $y$  region ( $N = 1$ ). For  $\lambda = 8$  we have uniformly 1 diffracted waves from the negative  $y$  region ( $M = -1$ ) and none from the positive  $y$  region ( $N = 0$ ).

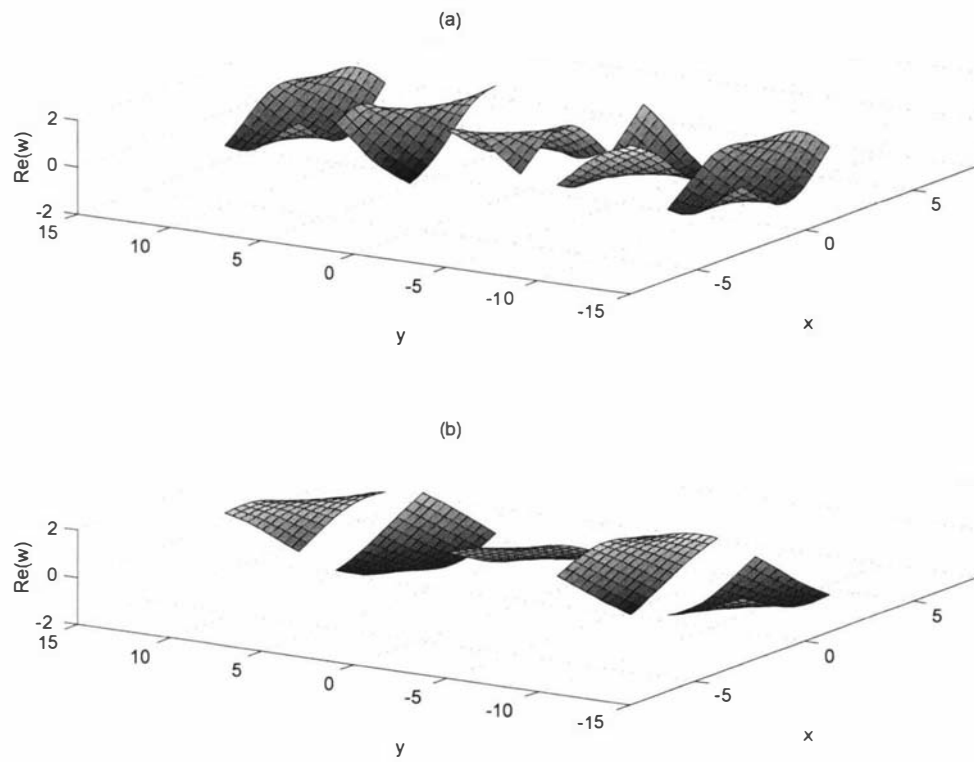


Figure 7.3.6. The displacement plot of five square plates as part of the periodic array. Each plate has area 16, stiffness  $\beta = 0.1$ , mass  $\gamma = 0$ , and is confined by a channel of width  $l = 6$ . The array is subjected to incident wave of wavelength (a)  $\lambda = 4$  and (b)  $\lambda = 8$ . The incident angle is  $\theta = \pi/6$ .

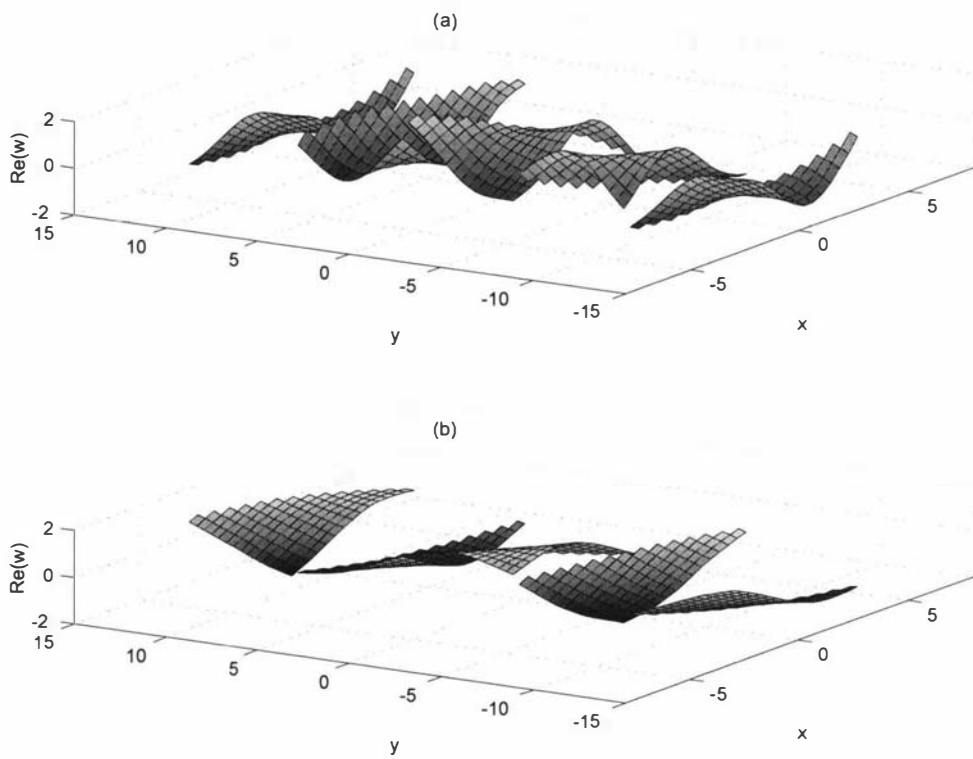


Figure 7.3.7. The displacement plot of five triangular plates as part of the periodic array. Each plate has area 16, stiffness  $\beta = 0.1$ , mass  $\gamma = 0$ , and is confined by a channel of width  $l = 6$ . The array is subjected to incident wave of wavelength (a)  $\lambda = 4$  and (b)  $\lambda = 8$ . The incident angle is  $\theta = \pi/6$ .

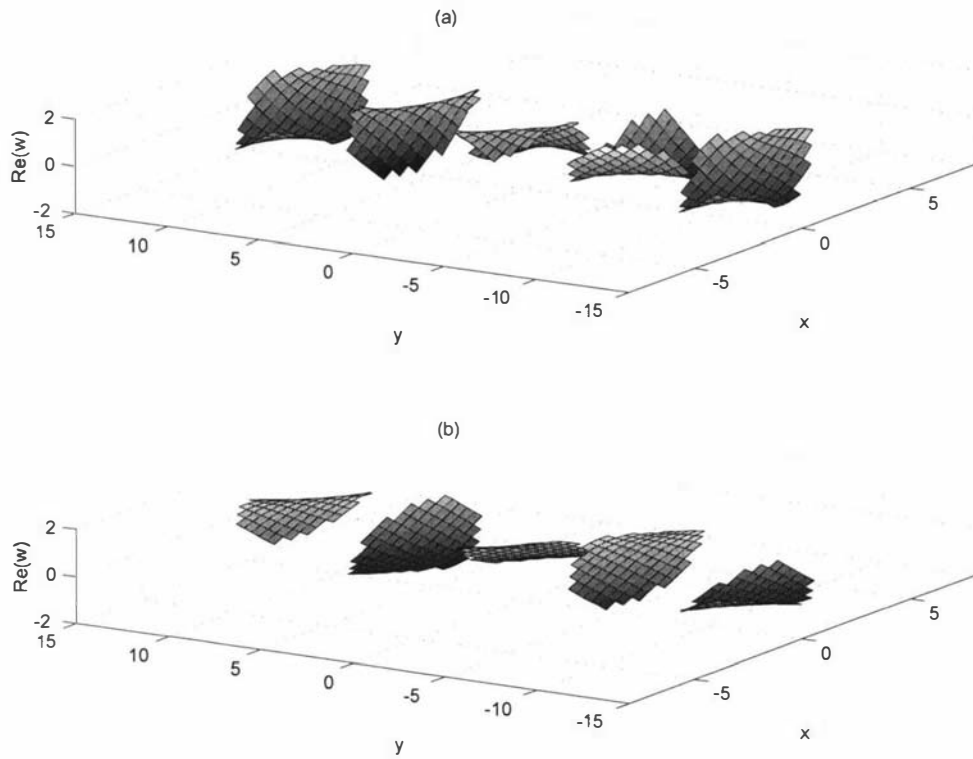


Figure 7.3.8. The displacement plot of five circular plates as part of the periodic array. Each plate has area 16, stiffness  $\beta = 0.1$ , mass  $\gamma = 0$ , and is confined by a channel of width  $l = 6$ . The array is subjected to incident wave of wavelength (a)  $\lambda = 4$  and (b)  $\lambda = 8$ . The incident angle is  $\theta = \pi/6$ .

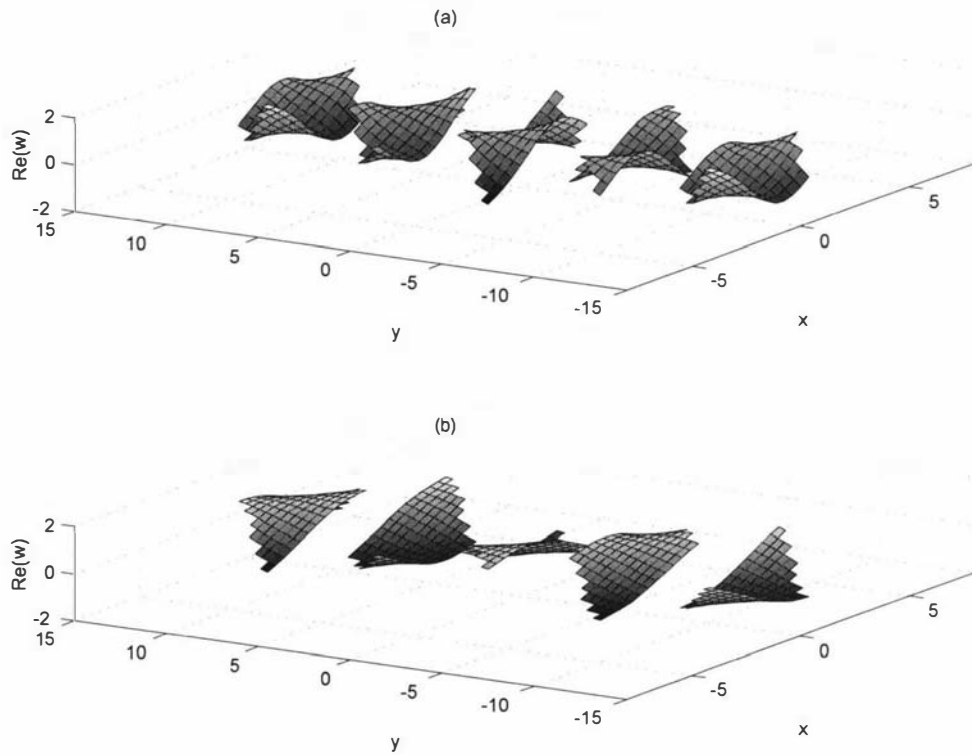


Figure 7.3.9. The displacement plot of five parallelogram plates as part of the periodic array. Each plate has area 16, stiffness  $\beta = 0.1$ , mass  $\gamma = 0$ , and is confined by a channel of width  $l = 6$ . The array is subjected to incident wave of wavelength (a)  $\lambda = 4$  and (b)  $\lambda = 8$ . The incident angle is  $\theta = \pi/6$ .

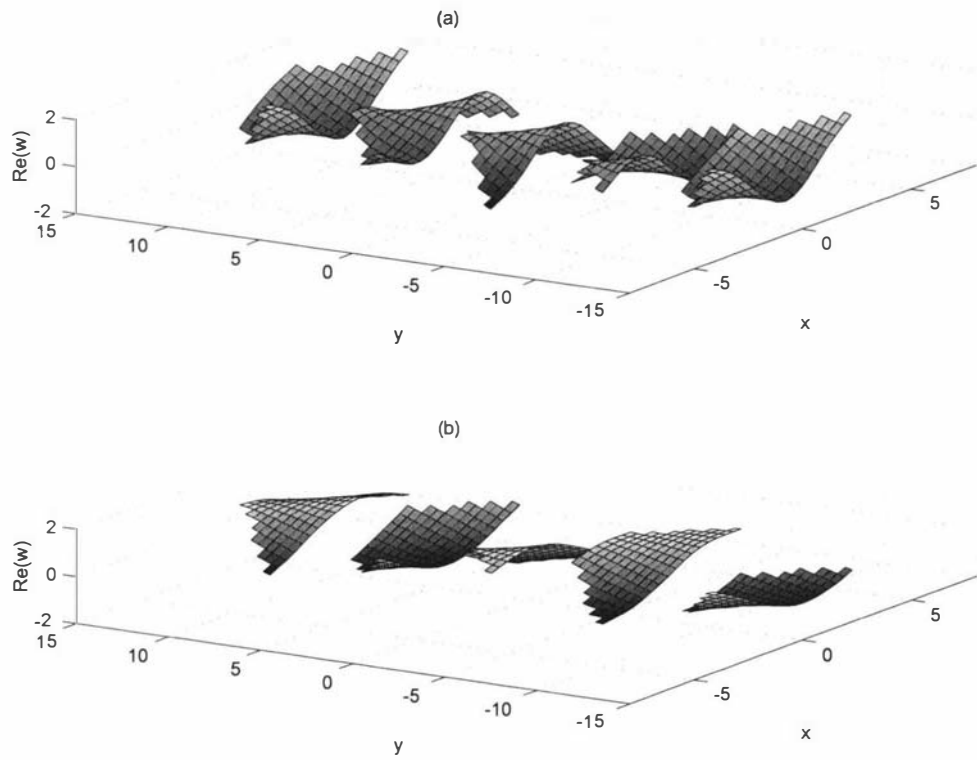


Figure 7.3.10. The displacement plot of five trapezoidal plates as part of the periodic array. Each plate has area 16, stiffness  $\beta = 0.1$ , mass  $\gamma = 0$ , and is confined by a channel of width  $l = 6$ . The array is subjected to incident wave of wavelength (a)  $\lambda = 4$  and (b)  $\lambda = 8$ . The incident angle is  $\theta = \pi/6$ .

# Chapter 8

## Summary and Conclusion

In the first part of this thesis we presented a method for calculating the linear wave response of a single plate. The method was based on Meylan's model for a plate of arbitrary geometry though our method would be of higher order than Meylan's method. A physical depiction and a mathematical model were presented in the second chapter. In the third chapter we discretized the plate into square panels and expanded the displacement of each panel in terms of the FEM basis functions. This was then used directly to minimize the variational equation for the coupled pressure equation. This yielded a matrix-vector equation that involved a forcing vector due to the potential of the water.

The forcing by the water was solved in the fourth chapter and this was later coupled with the displacement. Here we showed the difference in the order of our scheme from Meylan's. In Meylan's method the boundary integral equation of the potential was solved using the constant panel method. This was done by taking the value of the Green's function at the centre of the panels (which are of the FEM) and then assuming it as constant across the panels. A pair of mapping matrices was then used to include the Green's integral operator in the forcing vector and later in the full solution. This was done by taking the value of the Green's function at the centre of each panel. On the other hand the higher order method simply solved the boundary integral equation for the potential using the FEM basis function. This was achieved by taking an inner product of the forcing vector with the basis functions. The Green's integral equation (now over the basis functions) was solved numerically using the Gauss quadrature with Legendre polynomial. Since Meylan's method has been well-established we only presented the implementation and the results of the higher order method in the fifth chapter. Here we showed that the higher order method agreed with Meylan's method and indeed performed better than Meylan's. This was because the panels were elastic due to the use of the FEM basis functions, unlike Meylan's panels which were assumed constants. Hence the higher order method gives results which are closer to

reality. The drawback of the higher order method was the fact that the computation time of the Green's matrix was relatively large. However the use of a large number of panels is unnecessary because a small number of panels are sufficient to produce relatively accurate results (see Section 4.3).

In the second part of the thesis we extended the higher order method to calculate the response of a periodic line-array of elastic plates on infinitely deep water. In chapter six we explained the groundwork for the periodic line-array of elastic plates model. The model used ideas from the diffraction gratings in optics. We applied the Floquet's theorem to calculate the displacement and the potential. Upon applying this we obtained the same displacement equation and a slightly different boundary integral equation for the potential. We say this was slightly different because the kernel of the integral equation was now the periodic Green's function. The periodic Green's function was represented in the near-field form, far-field form, and the spectral domain form. It was known to be slow-convergent and hence we used the ideas from the surface grating in optics to accelerate this. The accelerated periodic Green's function was composed of all the three representations of the periodic Green's function. In the seventh chapter we derived the scattered waves due to the periodic line-array of elastic plates. First we separate the evanescent and the travelling waves by determining their modes. Then only modes that determined the travelling waves were used to calculate the diffracted waves. We further extracted the reflected and the transmitted waves from the zeroth mode. Finally the calculation of energy balance between the incoming and the diffracted, the reflected, and the transmitted waves were presented. Chapter eight contains the convergence study on the Green's function, the tests on the periodic line-array model, and the results.

We may improve and extend both the single plate and the multiple plates model by adding and/or modifying the methods used. In the single plate model accuracy can be improved by using triangular elements instead of square elements. This will lead to the use of slightly different mass and stiffness matrices. The single plate model can also be extended to a time-dependent model by replacing the free-surface Green's function with a time-

dependent free-surface Green's function (this is given in [Wehausen & Laitone, 1960]). A numerical time-integration scheme is needed for this extension.

The model for the periodic line-array on water of infinite depth can be easily extended to water of finite depth. A minor modification on the fast-convergent periodic Green's function is needed and this can be done using the same acceleration method explained in Section 5.4. Other than a periodical line-array of elastic plates that are used to model the MIZ, the same scheme may be used to solve a periodical line-array of barriers that extend through the depth of the water which was considered authors by Linton and Evans [Linton & Evans, 1992], Fernyhough and Evans [Fernyhough & Evans, 1995], and [Porter & Evans, 1998]. Moreover to obtain a depiction closer to the real-life MIZ we can extend the periodic line-array model from one dimensional to two-dimensional periodic gratings.

# Appendix A

## The Derivation of the Incident Plane Wave

We will derive the expression of the incident wave in water of finite depth and later generalize it for both finite and infinite depth.

The incident wave  $\phi^{In}(\mathbf{x}, z)$  must satisfy

$$\left. \begin{aligned} \nabla^2 \phi^{In} &= 0 \\ \frac{\partial \phi^{In}}{\partial z} &= \alpha \phi^{In}, \quad \mathbf{x} \notin \Delta, \quad z = 0, \end{aligned} \right\} \quad (\text{A.1})$$

At the bottom boundary we will use the boundary condition for water of finite depth

$$\frac{\partial \phi^{In}}{\partial z} = 0, \quad z = -H. \quad (\text{A.2})$$

Given a fixed angle  $\theta$  we may define a unit vector

$$\mathbf{r} = \begin{bmatrix} \cos \theta \\ \sin \theta \end{bmatrix},$$

that describe the direction of propagation of  $\phi^{In}$ . Then we can reduce the number of variables that  $\phi^{In}$  depends on from three ( $x$ ,  $y$ , and  $z$ ) to two by introducing a new variable

$$s = \mathbf{x} \cdot \mathbf{r}, \quad (\text{A.3})$$

and write  $\phi^{In}(\mathbf{x}, z) = \phi^{In}(s, z)$ . The Laplacian then simplifies into

$$\frac{\partial^2 \phi^{In}}{\partial s^2} + \frac{\partial^2 \phi^{In}}{\partial z^2} = 0. \quad (\text{A.4})$$

We solve (A.4) using the separation of variables by writing  $\phi^{In}$  into

$$\phi^{In}(s, z) = S(s) Z(z),$$

and substitute this into (A.1) and (A.2)

$$\frac{S''(s)}{S(s)} = \frac{-Z''(z)}{Z(z)} = -k^2, \quad (\text{A.5})$$

$$Z'(0) = \alpha Z(0), \quad (\text{A.6})$$

$$Z'(-H) = 0, \quad (\text{A.7})$$

where  $k$  is the wavenumber.

We can solve for  $Z(z)$  using the first order ODE from (A.5) and boundary condition (A.7)

$$Z(z) = \cosh [k(z + H)]. \quad (\text{A.8})$$

Further application of (A.7) gives us the equation for finding the travelling modes

$$\alpha = k \tanh(kH). \quad (\text{A.9})$$

Similarly we can easily obtain the solution for  $S(s)$

$$S(s) = A e^{iks} + B e^{-iks}. \quad (\text{A.10})$$

Multiplying (A.8) and (A.10) together gives us

$$\phi^{In}(s, z) = (A e^{iks} + B e^{-iks}) \cosh [k(z + H)].$$

We now substitute in (A.3)

$$\phi^{In}(\mathbf{x}, z) = (A e^{ik(\mathbf{x}\cdot\mathbf{r})} + B e^{-ik(\mathbf{x}\cdot\mathbf{r})}) \cosh [k(z + H)]. \quad (\text{A.11})$$

We impose the condition that the incident wave travels from left to right in the  $xy$ -plane and therefore we must have  $B = 0$ . The final form of  $\phi^{In}$  is

$$\phi^{In}(\mathbf{x}, z) = A e^{ik\mathbf{x}\cdot\mathbf{r}} \cosh [k(z + H)]. \quad (\text{A.12})$$

At the surface  $z = 0$  (A.12) simplifies into

$$\phi^{In}(\mathbf{x}) = A e^{ik\mathbf{x}\cdot\mathbf{r}} \cosh(kH).$$

Without loss of generality we incorporate the term  $\cosh(kH)$  into  $A$  and write the product as  $A^{In}$ . Therefore

$$\phi^{In}(\mathbf{x}) = A^{In} e^{ik\mathbf{x}\cdot\mathbf{r}}, \quad (\text{A.13})$$

is the equation for the incident wave that we use for both infinite and finite depth problems.

## Appendix B

# The Derivation of the Integral Equation for the Potential

The following procedure reduces the integral over the boundary of domain  $\Omega$  to an integral over the plate-covered area only. This method was first performed by Stoker ([Stoker, 1957]).

We apply Green's second theorem to  $\phi$

$$\int_{\Omega} [\phi \nabla^2 G - G \nabla^2 \phi] dV(\boldsymbol{\xi}, \zeta) = \int_{\partial\Omega} \left[ \phi \frac{\partial G}{\partial n} - G \frac{\partial \phi}{\partial n} \right] dS(\boldsymbol{\xi}, \zeta), \quad (\text{B.1})$$

where  $\partial\Omega$  denotes the boundary of domain  $\Omega$ . The boundary  $\partial\Omega$  consists of four parts:  $\partial\Omega_1$  is the perimeter of the imaginary bowl with radius  $a$ ,  $\partial\Omega_2$  is the free-surface,  $\partial\Omega_3$  is the plate-covered area, and  $\partial\Omega_4$  is the sea-floor. The left hand side of (B.1) can be reduced using (2.2.12) and (2.3.4) to

$$\phi(\mathbf{x}, z) = \sum_{j=1}^4 \int_{\partial\Omega_j} \left[ \phi \frac{\partial G}{\partial n} - G \frac{\partial \phi}{\partial n} \right] dS(\boldsymbol{\xi}, \zeta). \quad (\text{B.2})$$

Next we derive the expression for each  $j$  for the expression on the right hand side of (B.2). On boundary  $\partial\Omega_1$  the integrand  $\phi \frac{\partial G}{\partial n} - G \frac{\partial \phi}{\partial n}$  like  $1/a^2$  for  $a \rightarrow \infty$  since  $\phi$  and  $\frac{\partial \phi}{\partial n}$  are uniformly bounded at  $\infty$  [Stoker, 1957]. Thus, as  $a \rightarrow \infty$  the surface integral over  $\partial\Omega_1$  becomes zero. On boundary  $\partial\Omega_2$  we have

$$\begin{aligned} & \int_{\partial\Omega_2} \left[ \phi(\boldsymbol{\xi}, 0) \frac{\partial}{\partial \zeta} G(\mathbf{x}, z; \boldsymbol{\xi}, 0) - G(\mathbf{x}, z; \boldsymbol{\xi}, 0) \frac{\partial}{\partial \zeta} \phi(\boldsymbol{\xi}, 0) \right] dS_{\boldsymbol{\xi}} \\ &= \int_{\partial\Omega_2} \left[ \alpha G(\mathbf{x}, z; \boldsymbol{\xi}, 0) \phi(\boldsymbol{\xi}, 0) - G(\mathbf{x}, z; \boldsymbol{\xi}, 0) \frac{\partial}{\partial \zeta} \phi(\boldsymbol{\xi}, 0) \right] dS_{\boldsymbol{\xi}}, \end{aligned}$$

since  $\frac{\partial G}{\partial \zeta} = \alpha G$  every where on the surface,

$$\begin{aligned} & \int_{\partial\Omega_2} \left[ \phi(\boldsymbol{\xi}, 0) \frac{\partial}{\partial \zeta} G(\mathbf{x}, z; \boldsymbol{\xi}, 0) - G(\mathbf{x}, z; \boldsymbol{\xi}, 0) \frac{\partial}{\partial \zeta} \phi(\boldsymbol{\xi}, 0) \right] dS_{\boldsymbol{\xi}} \\ &= \int_{\partial\Omega_2} [\alpha G(\mathbf{x}, z; \boldsymbol{\xi}, 0) \phi(\boldsymbol{\xi}, 0) - \alpha G(\mathbf{x}, z; \boldsymbol{\xi}, 0) \phi(\boldsymbol{\xi}, 0)] dS_{\boldsymbol{\xi}}, \end{aligned}$$

as  $\frac{\partial \phi}{\partial \zeta} = \alpha \phi$  on the free-surface,

$$\int_{\partial\Omega_2} \left[ \phi(\boldsymbol{\xi}, 0) \frac{\partial}{\partial \zeta} G(\mathbf{x}, z; \boldsymbol{\xi}, 0) - G(\mathbf{x}, z; \boldsymbol{\xi}, 0) \frac{\partial}{\partial \zeta} \phi(\boldsymbol{\xi}, 0) \right] dS_{\boldsymbol{\xi}} = 0. \quad (\text{B.3})$$

On boundary  $\partial\Omega_4$  the integrand is clearly zero since  $\frac{\partial G}{\partial \zeta} = 0$  and  $\frac{\partial \phi}{\partial \zeta} = 0$  and, hence, there is no contribution from this either. On boundary  $\partial\Omega_3$  ( $\partial\Omega_3$  is equivalent to  $\Delta$ ) the surface integral becomes

$$\begin{aligned} & \int_{\partial\Omega_3} \left[ \phi(\boldsymbol{\xi}, 0) \frac{\partial}{\partial \zeta} G(\mathbf{x}, z; \boldsymbol{\xi}, 0) - G(\mathbf{x}, z; \boldsymbol{\xi}, 0) \frac{\partial}{\partial \zeta} \phi(\boldsymbol{\xi}, 0) \right] dS_{\boldsymbol{\xi}} \\ &= \int_{\partial\Omega_3} \left[ \alpha G(\mathbf{x}, z; \boldsymbol{\xi}, 0) \phi(\boldsymbol{\xi}, 0) - G(\mathbf{x}, z; \boldsymbol{\xi}, 0) \frac{\partial}{\partial \zeta} \phi(\boldsymbol{\xi}, 0) \right] dS_{\boldsymbol{\xi}}. \end{aligned} \quad (\text{B.4})$$

Finally we back substitute the results from taking the surface integral around  $\partial\Omega_1$ , (B.3), and (B.4) into the equation. This gives us the integral equation for the scattered potential

$$\phi(\mathbf{x}, z) = \int_{\Delta} \left[ \alpha G(\mathbf{x}, z; \boldsymbol{\xi}, 0) \phi(\boldsymbol{\xi}, 0) + i\sqrt{\alpha} G(\mathbf{x}, z; \boldsymbol{\xi}, 0) \frac{\partial}{\partial \zeta} \phi(\boldsymbol{\xi}, 0) \right] dS_{\boldsymbol{\xi}}. \quad (\text{B.5})$$

Clearly this procedure is applicable for the incident wave  $\phi^{In}$  and the same result can be derived.

# Appendix C

## Computing the Matrices, the Vectors and the Operators

The coding of all the matrices in the Section 3 are done with both MATLAB and C++. The MATLAB equivalent codes for the matrices and the operations in (3.5.21) and (3.5.20) codes are built in a straight forward manner. However codes and operations in C++ are somewhat different. In this section we will explain the implementation in C++.

The matrices and the vectors are built using the Template Numerical Toolkit (TNT) [Pozo, 2000]. The TNT provides C++ classes for both the FORTRAN-type C-type arrays (matrices and vectors). We will give brief definitions on the FORTRAN-type array and the C-type array. A FORTRAN-type array is column oriented, i.e. the elements are arranged and read per column, and its index begins with 1. Whereas a C-type array is row-oriented (elements are arranged and read per row) and its index begins with 0.

We intend to build the matrices and the vectors to be as close as possible to the ones in MATLAB. Therefore we use the TNT classes for the FORTRAN-type array. Matrices  $\mathbb{M}$  and  $\mathbb{K}$  are double precision and matrix  $\mathbb{G}$  is a complex double precision FORTRAN matrices (defined in `finat.h`). Vectors  $\hat{\phi}^{In}$ ,  $\hat{\phi}$ , and  $\hat{w}$  are complex double precision FORTRAN vectors. Furthermore vector  $\mathbb{N}$  and matrix  $\mathbb{N}$  are both double precision FORTRAN arrays.

The coding for submatrices in (4.1.1) and (4.1.2) is straight forward; and likewise are (3.5.30) and (3.5.31). The coding of (3.5.28) and (3.5.29) requires the calculation of the Green's function (2.3.11) or (2.3.13) as well as the Gauss quadrature-Legendre polynomial scheme. We analyze (2.3.11) and (2.3.13) separately starting with (2.3.11).

For the case of finite depth (2.3.11) we truncate the infinite sum into

$$G(\mathbf{x}; \boldsymbol{\xi}) = - \sum_{j=1}^N \frac{K_0(k_j |\mathbf{x} - \boldsymbol{\xi}|)}{2\pi C_j} \cos^2 k_j(H). \quad (\text{C.1})$$

Equation (C.1) requires the roots of the dispersion equation (2.3.8). We choose the roots in a way such that the first root  $k_0$  is a negative purely imaginary number and the remaining  $k_j$  ( $j = 1, \dots, N$ ) are positive real numbers with ascending magnitude.

The computation of the second kind modified Bessel function of order zero  $K_0(x)$  is provided by the GNU Scientific Library (GSL) function [Galassi et al., 2002a]. However, to use such function in the library,  $x$  is required to be a positive real number [Galassi et al., 2002b]. Hence the corresponding  $K_0$  for the first root cannot be calculated using the GSL  $K_0$  function. To overcome this restriction we use the relation

$$K_0(-ik|\mathbf{x} - \boldsymbol{\xi}|) = \frac{i\pi}{2} H_0(k|\mathbf{x} - \boldsymbol{\xi}|),$$

where  $H_0$  is the Hankel function of order zero. Using relation  $H_0(x) = J_0(x) + iY_0(x)$  we obtain

$$K_0(-ik|\mathbf{x} - \boldsymbol{\xi}|) = \frac{i\pi}{2} \{J_0(k|\mathbf{x} - \boldsymbol{\xi}|) + iY_0(k|\mathbf{x} - \boldsymbol{\xi}|)\}. \quad (\text{C.2})$$

[Abramowitz & Stegun, 1964]. Expression (C.2) is now solvable by GSL functions since, for both  $J_0$  and  $Y_0$  argument  $k|\mathbf{x} - \boldsymbol{\xi}|$  is a positive real number.

For the case of infinite depth we are required to individually calculate  $H_0$ ,  $Y_0$ , and  $J_0$  in (2.3.13). Since this is time-consuming we accelerate the calculation by replacing the sum of the three special functions with one table. The table contains a finite range of  $t$  and its corresponding  $f(t) = H_0(t) + Y_0(t) - 2iJ_0(t)$ . Then for each  $\alpha\mathbf{x}$  we look up the table to find its corresponding  $f(\alpha\mathbf{x})$ . This is done using the linear interpolation provided by GNU Scientific Library (GSL) [Galassi et al., 2002b].

To determine the integration points and their corresponding weight for the Gauss quadrature we use the Legendre polynomial. We recall from Section 3.5.3 the definition of  $[g]_{de}$  (3.5.14)

$$[g]_{de} = \int_{\Delta_d} \mathbf{N}(\mathbf{x}_d) \int_{\Delta_e} G(\mathbf{x}_d; \boldsymbol{\xi}_e) \mathbf{N}(\boldsymbol{\xi}_e) dS_{\boldsymbol{\xi}} dS_{\mathbf{x}}.$$

Since  $\Delta_d$  and  $\Delta_e$  are physically identical one numerical integration scheme is sufficient for both integrals in  $[g]_{de}$ .

For all area integration over  $\Delta_d$  we first write it in full

$$\int_{\Delta_d} f(\mathbf{x}) dS_{\mathbf{x}} = \int_{y=-b}^b \int_{x=-a}^a f(x, y) dx dy. \quad (\text{C.3})$$

We approximate the integral (C.3) with respect to  $x$  using Gaussian quadrature

$$\int_{x=-a}^a f(x, y) dx = \sum_{j=1}^n W_{n,j} f(x_j, y), \quad (\text{C.4})$$

where  $y$  is kept constant. The integration points (or also known as abscissae) and their corresponding weights are calculated from the roots of a set of orthogonal polynomials. Here we use the Legendre functions as the orthogonal polynomials.

The abscissae  $x_j$ 's are the roots of the Legendre polynomials. These are found using Newton-Raphson method repetitively on Legendre polynomials from order 1 to  $Q$  (the specified number of points). We use the recurrence relation of the Legendre polynomials  $1 \leq j \leq Q$  (or  $P$ )

$$P_j(x) = \frac{1}{j-1} [(2j-3)xP_{j-1}(x) - (j-2)P_{j-2}(x)], \quad (\text{C.5})$$

and its derivative

$$P'_j(x) = \frac{1}{j} [(2j-1)(P_{j-1}(x) + xP'_{j-1}(x)) - (j-1)P'_{j-2}(x)], \quad (\text{C.6})$$

where

$$P_0 = 1, \quad P_1 = x, \quad P'_2 = 3x.$$

For Gaussian quadrature (C.4) that requires a maximum of  $n$  abscissae the corresponding weights for  $x_j$ 's are calculated using

$$W_{n,j} = \frac{2}{(1-x_j^2)(P'_n(x_j))^2}. \quad (\text{C.7})$$

The same Gaussian quadrature-Legendre polynomials pair is applied to the integral with respect to  $y$  with maximum  $m$  abscissae to obtain a set of  $y_j$ 's and their corresponding weights  $W_{m,j}$ 's.

Then the total number of abscissae  $Q = n \times m$  (and likewise  $P$ ) and the weights  $u_i$ 's and  $v_j$ 's of (3.5.26) are obtained by multiplying  $W_n$ 's and  $W_m$ 's where each satisfies (C.7). Since the panel is a square then we set  $m = n$ .

Finally multiplication between a matrix and vector, such as  $\mathbb{M} \hat{\phi}^{In}$ , is done using the built-in operator in the TNT. Matrix multiplication, such as  $\mathbb{N}_1 \mathbb{G}_1 \mathbb{N}_2$ , is done using the Basic Linear Algebra Subprograms (BLAS) [Dongarra et al., 1997], in particular BLAS level 3 for general matrices. To invert the matrix  $(\mathbb{M} - \alpha \mathbb{G})$  in (3.5.21) and (3.5.20) we use a function provided by the Linear Algebra Package (LAPACK) [Anderson et al., 1999].

LAPACK also provides LU linear solver that solves (3.5.21). Substituting the solution of (3.5.21) to (3.5.20) completes the process of solving  $\hat{\mathbf{w}}$  and  $\hat{\phi}$ .

# Appendix D

## The Asymptotic Representation of the periodic Green's Function

### D.1 The Spatial Representation of the Periodic Green's function

We recall the free-surface Green's function for infinitely deep water

$$G(\mathbf{x}; \boldsymbol{\xi}) = \frac{1}{4\pi} \left( \frac{2}{|\mathbf{x} - \boldsymbol{\xi}|} - \pi\alpha [\mathbf{H}_0(\alpha|\mathbf{x} - \boldsymbol{\xi}|) + Y_0(\alpha|\mathbf{x} - \boldsymbol{\xi}|) - 2i J_0(\alpha|\mathbf{x} - \boldsymbol{\xi}|)] \right).$$

We let  $|\mathbf{x} - \boldsymbol{\xi}| \rightarrow \infty$ . Therefore we may write the Struve function  $\mathbf{H}_0$  in the asymptotic expansion

$$\mathbf{H}_0(\alpha|\mathbf{x} - \boldsymbol{\xi}|) \sim Y_0(\alpha|\mathbf{x} - \boldsymbol{\xi}|) + \frac{2}{\pi} \left( \frac{1}{\alpha|\mathbf{x} - \boldsymbol{\xi}|} - \frac{1}{(\alpha|\mathbf{x} - \boldsymbol{\xi}|)^3} + \frac{1^2 3^2}{(\alpha|\mathbf{x} - \boldsymbol{\xi}|)^5} - \dots \right).$$

As  $r \rightarrow \infty$

$$\mathbf{H}_0(\alpha|\mathbf{x} - \boldsymbol{\xi}|) \sim Y_0(\alpha|\mathbf{x} - \boldsymbol{\xi}|),$$

substituting this into (2.3.13)

$$G(\mathbf{x}; \boldsymbol{\xi}) = \frac{\alpha}{4} [2Y_0(\alpha|\mathbf{x} - \boldsymbol{\xi}|) - 2i J_0(\alpha|\mathbf{x} - \boldsymbol{\xi}|)],$$

where  $\frac{2}{|\mathbf{x} - \boldsymbol{\xi}|} \rightarrow 0$  as  $r \rightarrow \infty$ . Factoring out  $-2i$  gives

$$\begin{aligned} G(\mathbf{x}; \boldsymbol{\xi}) &= -\frac{i\alpha}{2} [J_0(\alpha|\mathbf{x} - \boldsymbol{\xi}|) + iY_0(\alpha|\mathbf{x} - \boldsymbol{\xi}|)] \\ &= -\frac{i\alpha}{2} H_0(\alpha|\mathbf{x} - \boldsymbol{\xi}|). \end{aligned} \tag{D.1.1}$$

The new representation of the Green's function (D.1.1) matches the one given by Linton [[Linton, 1998], (2.4), p.378] however with different multiplying constant.

## D.2 The Spectral Representation of the Periodic Green's function

Linton [[Linton & Evans, 1992], (2.26), p. 330] gave an alternative form of the Hankel function

$$H_0 \left( k [X^2 + Y_m^2]^{\frac{1}{2}} \right) = -\frac{i}{\pi} \int_{-\infty}^{\infty} U^{-1} e^{-kU|X|} e^{-ikY_m u} du, \quad (\text{D.2.1})$$

where  $U = (u^2 - 1)^{\frac{1}{2}}$ .

Substituting (D.2.1) into (5.3.2) yields

$$G_{\mathbf{P}}(\mathbf{x}; \boldsymbol{\xi}) = -\frac{i}{\pi} c(k) \underbrace{\sum_{m=-\infty}^{\infty} \int_{-\infty}^{\infty} U^{-1} e^{-kU|X|} e^{-ikY_m u} du}_{\hat{F}(\mathbf{x}; \boldsymbol{\xi}_m)} e^{im\sigma l}. \quad (\text{D.2.2})$$

First we observe part  $\hat{F}(\mathbf{x}; \boldsymbol{\xi}_m)$ .

$$\begin{aligned} \hat{F}(\mathbf{x}; \boldsymbol{\xi}_m) &= \sum_{m=-\infty}^{\infty} \int_{-\infty}^{\infty} U^{-1} e^{-kU|X|} e^{-ikY u + ikml} e^{im\sigma l} du \\ &= \int_{-\infty}^{\infty} U^{-1} e^{-kU|X|} e^{-ikY u} \sum_{m=-\infty}^{\infty} e^{iml(ku + \sigma)} du \end{aligned}$$

then we replace  $\sum_{m=-\infty}^{\infty} e^{iml(ku + \sigma)}$  with

$$\sum_{m=-\infty}^{\infty} e^{iml(ku + \sigma)} = 2\pi \sum_{m=-\infty}^{\infty} \delta(l(ku + \sigma) + 2\pi m),$$

and this gives

$$\hat{F}(\mathbf{x}; \boldsymbol{\xi}_m) = 2\pi \int_{-\infty}^{\infty} U^{-1} e^{-kU|X|} e^{-ikY u} \sum_{m=-\infty}^{\infty} \delta(l(ku + \sigma) + 2\pi m) du. \quad (\text{D.2.3})$$

We may rewrite (D.2.3) as

$$\begin{aligned} \hat{F}(\mathbf{x}; \boldsymbol{\xi}_m) &= 2\pi \int_{-\infty}^{\infty} \tilde{F}(u) \sum_{m=-\infty}^{\infty} \delta(l[ku + \sigma_m]) du \\ &= \frac{2\pi}{l} \sum_{m=-\infty}^{\infty} \int_{-\infty}^{\infty} \tilde{F}(u) \delta(ku + \sigma_m) du, \end{aligned} \quad (\text{D.2.4})$$

where

$$\tilde{F}(u) = U^{-1} e^{-kU|X|} e^{-ikY u} \quad (\text{D.2.5})$$

and

$$\sigma_m = \sigma + \frac{2\pi m}{l} \quad (\text{D.2.6})$$

Let  $u' = ku$  in (D.2.5)

$$\hat{F}(\mathbf{x}; \boldsymbol{\xi}_m) = \frac{2\pi}{l} \sum_{m=-\infty}^{\infty} \frac{1}{k} \int_{-\infty}^{\infty} \tilde{F}\left(\frac{u'}{k}\right) \delta(u' + \sigma_m) du' \quad (\text{D.2.7})$$

We recall that

$$\int_{-\infty}^{\infty} \delta(\tau - u) \tilde{F}(u) du = \tilde{F}(\tau). \quad (\text{D.2.8})$$

We apply (D.2.8) into (D.2.7) and find that  $\tau = \frac{-\sigma_m}{k}$ .

$$\hat{F}(\mathbf{x}; \boldsymbol{\xi}_m) = \frac{2\pi}{l} \sum_{m=-\infty}^{\infty} \frac{1}{k} \tilde{F}\left(\frac{-\sigma_m}{k}\right), \quad (\text{D.2.9})$$

and then we substitute  $\frac{-\sigma_m}{k}$  into (D.2.5)

$$\begin{aligned} \tilde{F}\left(\frac{-\sigma_m}{k}\right) &= \frac{e^{-k\left[\left(\frac{-\sigma_m}{k}\right)^2 - 1\right]^{\frac{1}{2}}|X|} e^{-ikY\left(\frac{-\sigma_m}{k}\right)}}{\left[\left(\frac{-\sigma_m}{k}\right)^2 - 1\right]^{\frac{1}{2}}} \\ &= \frac{e^{-k\left[\frac{1}{k^2}(\sigma_m^2 - k^2)\right]^{\frac{1}{2}}|X|} e^{i\sigma_m Y}}{\left[\frac{1}{k^2}(\sigma_m^2 - k^2)\right]^{\frac{1}{2}}} \\ &= \frac{k e^{-U_m|X|} e^{i\sigma_m Y}}{U_m}, \end{aligned} \quad (\text{D.2.10})$$

$$U_m = [\sigma_m^2 - k^2]^{\frac{1}{2}}. \quad (\text{D.2.11})$$

Back substitution of (D.2.10) into (D.2.9) gives us

$$\hat{F}(\mathbf{x}; \boldsymbol{\xi}_m) = \frac{2\pi}{l} \sum_{m=-\infty}^{\infty} \frac{e^{-U_m|X|} e^{i\sigma_m Y}}{U_m}, \quad (\text{D.2.12})$$

and further back-substitution of (D.2.12) into (D.2.2) yields

$$G_{\mathbf{P}}(\mathbf{x}; \boldsymbol{\xi}) = -\frac{2i}{l} c(k) \sum_{m=-\infty}^{\infty} \frac{e^{-U_m|X|} e^{i\sigma_m Y}}{U_m}, \quad (\text{D.2.13})$$

the spectral representation of the periodic Green's function for large distance. Expression (D.2.13) is also known as the Fourier transform of (D.2.2) [Jorgenson & Mittra, 1990].

# Bibliography

- Abramowitz, M. & Stegun, I. (1964). *Handbook of Mathematical Functions*. Dover Inc. New York.
- Anderson, E., Bai, Z., Bischof, C., Blackford, S., Demmel, J., Dongarra, J., Croz, J. D., Greenbaum, A., Hammarling, S., McKenney, A., , & Sorensen, D. (1999). *LAPACK Users' Guide*. Philadelphia, PA: Society for Industrial and Applied Mathematics, third edition.
- Dongarra, J., Croz, J. D., Hammarling, S., Hanson, R. J., Duff, I. S., Lawson, C. L., Kincaid, D., & Krogh, F. T. (1997). Basic linear algebra subprograms (BLAS) for FORTRAN77 [computer codes]. Online distribution: <http://www.netlib.org/blas/>.
- Fernyhough, M. & Evans, D. V. (1995). Scattering by a periodic array of rectangular blocks. *J. Fluid Mech.*, 305, 263–279.
- Galassi, M., Davies, J., Theiler, J., Gough, B., Jungman, G., Booth, M., & Rossi, F. (2002a). GNU scientific library (GSL) version 1.3 [computer codes]. Online distribution <http://sources.redhat.com/gsl/>.
- Galassi, M., Davies, J., Theiler, J., Gough, B., Jungman, G., Booth, M., & Rossi, F. (2002b). *GNU Scientific Library Reference Manual*. Network Theory Ltd., second edition.
- Hamamoto, T., Suzuki, A., & Fujita, K. (1997). Hybrid dynamic analysis of large tension leg floating structures using plate elements. *Proc. 7th Int. Offshore and Polar Eng. Conf.*, 1, 285–292.
- Hermans, A. J. (2000). A boundary element method for the interaction of free-surface waves with a very large floating flexible platform. *J. Fluids and Structures*, 14, 943–956.
- Hildebrand, F. B. (1965). *Methods of Applied Mathematics*. Prentice-Hill, 2nd edition.
- John, F. (1950). On the motion of floating bodies ii. *Commun. Pure Appl. Math.*, 3, 45–101.
- Jorgenson, R. E. & Mittra, R. (1990). Efficient calculation of the free-space periodic green's function. *IEEE Transaction on Antennas and Propagation*, 38, 633–642.

- Kashiwagi, M. (1996). A b-spline galerkin method for computing hydroelastic behaviors of a very large floating structure. *Proc. Int. Wksp. on Very Large Floating Struct*, (pp. 149–156).
- Kashiwagi, M. (1998a). A b-spline galerkin scheme for calculating hydroelastic response of a very large floating structure in waves. *J. Marine Sci. and Tech.*, 3, 37–49.
- Kashiwagi, M. (1998b). A b-spline galerkin scheme for calculating the hydroelastic response of a very large floating structures in waves. *J. Mar. Sci. Technol.*, 3, 37–49.
- Kashiwagi, M. (2000). Research on hydroelastic responses of VLFS: Recent progress and future work. *Intl. J. Offshore and Polar Eng.*, 10, 81–90.
- Lin, X. & Takaki, M. (1998). On b-spline element methods for predicting hydroelastic response of a very large floating structures in waves. *Proc. 2nd Int Conf. Hydroelast. in Marine Tech*, (pp. 219–229).
- Linton, C. M. (1998). The green's function for the two-dimensional helmholtz equation in periodic domains. *J. Eng. Math.*, 33, 377–402.
- Linton, C. M. (1999). Rapidly convergent representation for green's functions for laplace's equation. *Proc. R. Soc. Lond*, A(455), 1767–1797.
- Linton, C. M. & Evans, D. V. (1992). The radiation and scattering of surface waves by a vertical circular cylinder in a channel. *Phil. Trans. R. Soc. Lond.*, A(338), 325–357.
- Maeda, H., Masuda, K., Miyajima, S., & Ikoma, T. (1995). Hydroelastic response of pontoon type very large floating offshore structure. *J. Soc Naval Arch Japan*, 178, 203–212.
- Marchenko, A. V. & Voliak, K. I. (1997). Surface wave propagation in shallow water beneath an inhomogeneous ice cover. *J. Phys. Oceanography*, 27, 1602–1613.
- Masson, D. & LeBlond, P. H. (1989). Spectral evolution of wind-generated surface gravity waves in dispersed ice field. *J. Fluid Mech*, 202, 43–81.
- Mei, C. C. (1989). *The Applied Dynamics of Ocean Surface Waves - Advance Series on Ocean Engineering*, volume 1. World Scientific.
- Meylan, M. H. (1994). *The Behaviour of Sea Ice in Ocean Waves*. PhD thesis, University of Otago, Dunedin.

- Meylan, M. H. (1997). The wave forcing of a three dimensional floating elastic body. *Int. Offshore and Polar Eng. Conf.*, 1, 293–298.
- Meylan, M. H. (2001). A variation equation for the wave forcing of floating thin plates. *J. of Applied Ocean Res.*, 23(4), 195–206.
- Meylan, M. H. (2002). The wave response of ice floes of arbitrary geometry. *J. of Geophysical Research - Oceans*, 107(C6).
- Meylan, M. H. & Squire, V. A. (1994). The response of ice floes to ocean waves. *J. of Geophysical Research*, 99(C1), 891–900.
- Meylan, M. H. & Squire, V. A. (1996). Response of a circular ice floe to ocean waves. *J. of Geophysical Research*, 101(C4), 8869–8884.
- Meylan, M. H., Squire, V. A., & Fox, C. (1997). Towards realism in modeling ocean wave behavior in marginal ice zones. *J. of Geophysical Research*, 102(C10), 22981–22991.
- Moritz, R. E. & Ukita, J. (2000). Geometry and the deformation of pack ice: I. a simple kinematic model. *Annals. Glaciology*, 31, 313–322.
- Petyt, M. (1990). *Introduction to Finite Element Vibration Analysis*. Cambridge University Press.
- Porter, R. & Evans, D. V. (1998). Rayleigh-bloch surface waves along periodic gratings and their connection with trapped modes in waveguides. *J. Fluid Mech.*, (386), 233–258.
- Pozo, R. (2000). Template numerical toolkit (TNT) version 0.94 [computer codes]. Online distribution: <http://www.nist.gov/tnt/index.html>.
- Sarpkaya, T. & Isaacson, M. (1981). *Mechanics of Wave Forces on Offshore Structures*. Van Nostrand Reinhold.
- Scott, C. (1998). *Introduction to Optics and Optical Imaging*. IEEE Press.
- Singh, S., Richards, W. F., Zinecker, J. R., & Wilton, D. R. (1990). Accelerating the convergence of series representing the free-surface periodic green's function. *IEEE Transaction on Antennas and Propagation*, 38(12), 1958–1962.
- Squire, V. A., Duggan, J. P., Wadhams, P., Rottier, P. J., & Liu, A. J. (1995). Of ocean waves and sea ice. *Annu. Rev. Fluid Mech.*, 27, 115–168.

- Stoker, J. J. (1957). *Water Waves: The Mathematical Theory with Applications*. Interscience.
- Takaki, M. & Gu, X. (1996). Motions of a floating elastic plate in waves. *J. Soc. Naval Arch. Japan*, 180, 331–339.
- Ukita, J. & Moritz, R. E. (2000). Geometry and the deformation of pack ice: II. simulation with a random isotropic model and implication in sea-ice rheology. *Annals. Glaciology*, 31, 323–326.
- Wadhams, P. (1986). The seasonal ice zone. In N. Untersteiner (Ed.), *The Geophysics of Sea Ice* (pp. 825–991).: Plenum New York.
- Wang, C. D. & Meylan, M. H. (2004). Higher order method for the wave forcing of a floating thin plate of arbitrary geometry. *Journal of Fluid and Structures*, 19(4), 557–572.
- Watanabe, E., Utsunomiya, T., & Wang, C. M. (2004). Hydroelastic analysis of pontoon-type VLFS: A literature survey. *Eng. Struct.*, 26, 245–256.
- Wehausen, J. & Laitone, E. (1960). Surface waves. In S. Flugge & C. Truesdell (Eds.), *Handbuch der Physik, Fluid Dynamics III*, volume 9 of *Handbuch der Physik* chapter 3, (pp. 446–778). Springer-Verlag Berlin.
- Yago, K. & Endo, H. (1996). Model experiment and numerical calculation of the hydroelastic behaviour of matlike VLFS. *Int. Wksp. on Very Large Floating Struct.*, (pp. 209–216).
- Yasuzawa, Y., Kagawa, K., & Kawano, D. (1996). Wave response analysis of a flexible large floating structure. *Int. Wksp. on Very Large Floating Struct.*, (pp. 221–228).

# Index

- angular frequency,  $\omega$ , 12
- assembler matrix, 22, 41
  - bypassing the, 40
- B-spline functions, 2
  - bi-cubic, 2
- Bernoulli
  - Euler equation, 1, 2, 11, 18
  - linearised law, 2, 10
  - Linearized equation, 3
- boundary condition, 5, 14, 112
  - bottom, 15
    - finite depth, 10
    - finite depth water, 111
    - infinitely deep water, 10
  - dynamic, 18
  - free edge, 11
  - radiation, 15
  - Sommerfeld, 13
  - surface, 15
    - dynamic, 10
    - kinematic, 10
- Boundary Element Method (BEM), 3
  - and FEM (see also Finite Element Method), 4, 17
  - boundary integral equation for the potential, 13
  - derivation of the boundary integral equation, 113
  - via integro-differential equation, 4
- boundary integral equation
  - for periodic array of plates, 65, 74
  - for the potential, 15
  - with Green's integral operator, 31
- channel, 63
- computer codes
  - C++, 115
  - FORTRAN, 115
  - GSL, 116
  - MATLAB, 115
  - TNT, 115
- constant panel method, 26
  - accuracy, 43
  - comparison of accuracy with higher order method, 43
  - comparison with higher order method, 43, 45
  - convergence, 43
  - forcing vector, 28
    - by constant panel method, 29
  - linear equation, 29
  - $\mathbb{P}^\Delta$ ,  $\mathbb{P}^\Omega$ , 28
  - piecewise constants area FEM basis functions, 29
  - relationship with assembler matrix, 28, 29
  - result, 45
  - solution to the Green's function, 27, 28
- coupled pressure equation, 11, 108
- density of the water, 10
- diffracted waves, 73, 74, 78, 87
  - amplitude, 75
  - angles (see also diffraction angle), 75
  - coefficient of order 0, 77
  - directions of propagation, 75
  - $x \rightarrow -\infty$ , 74
  - negative  $x$  direction, 77
  - negative  $y$ -region, 75
  - $x \rightarrow \infty$ , 74
  - positive  $x$  direction, 77
  - positive  $y$ -region, 75
- diffraction angle, 75
  - and incident angle, 75
- diffraction coefficient, 77
- diffraction gratings, 6, 63, 109

- diffraction order, 65, 75
  - lower, 72
  - upper, 72
- dispersion equation, 16
- displacement vector
  - for a panel, 21
  - for a plate, 21
- energy balance, 109
  - relation with diffracted, reflected, and transmitted waves, 78
  - relation with incident wave, 78
  - total, 78
- Evans
  - Fernyhough and, 6, 110
  - Linton and, 110
  - Porter and, 6, 110
- field panel, 32
- Finite Element Method
  - elements of potential vector, 31
- Finite Element Method (FEM), 19, 108
  - assembler matrix (see also assembler matrix), 22
  - basis vector, 19
  - displacement equation, 19
    - for plate, 25
  - displacement vector
    - for a panel, 21
    - for a plate, 21
  - elements of displacement vector, 21
  - mass matrix
    - panel, 25, 37
    - plate, 26, 33, 37
  - potential vector, 31
    - incident, 31
  - stiffness matrix
    - panel, 25, 39
    - plate, 25, 37
  - transformation matrices, 40
- Floquet's theorem, 62, 63
  - application of, 63
- forcing vector, 26, 28
- Fourier series
  - representation of wave spectra, 65
- Fourier transform
  - of periodic Green's function, 67
- gap, 63
- Gauss-Legendre, 45, 56, 108, 116
  - number of points, 47
- gravitational acceleration, 10
- Green's function
  - asymptotic approximation, 66
  - construction of, 15
  - finite depth, 15
    - series representation, 16
  - free surface, 4, 6
    - and boundary element method, 13
    - infinitely deep water, 119
    - periodic (also see periodic), 6
    - singularity, 28
    - time-dependent, 110
  - free-surface, 15
  - implementation in computer codes, 115
    - infinitely deep water, 16
    - integral equation (see also Green's integral operator), 27
    - zero-draft (also see free surface), 1
- Green's integral equation
  - for periodic line-array, 65
- Green's integral operator, 27, 31
  - periodic, 66
- Green's matrix, 36, 41
  - calculation using Gauss-Legendre quadrature, 115
  - composite, 41
    - panel, 33
    - plate, 33
- Green's second theorem, 14, 113
- Hamamoto, 2, 3
- Hankel function, 116

- Hermans, 4
- higher order method, 6
  - and Meylan's method, 34
  - error comparison, 45
  - assembling matrices, 37
  - boundary integral equation
    - for a panel, 33
  - comparison with Meylan's method, 43
  - convergence of, 45
  - extension to line-array, 6
  - forcing vector of the plate (see also forcing vector), 26
  - Green's matrix, 33, 37
    - and Gaussian quadrature, 34
  - integral equation, solution to, 32
  - linear equation, 34
  - numerical implementation, 37
  - quadrature points, 45
  - results, 45
  - solution to the plate-water motion, 29
- images, 63
- incident wave, 13, 14, 74, 112
  - angle (waveangle), 13
  - derivation of, 111
- inner product, 32
- integral equation
  - boundary (see also Boundary Element Method (BEM)), 16
  - boundary, solution by Meylan (see also Meylan's method), 26
- isotropic plate, 11
- Kashiwagi, 1–3, 8
- Kochin's function, 45, 47
- Kummer's transformation, 69
- Laplace
  - laplacian, 4
- Laplace's equation, 10, 14, 111
- Linton
  - see also Green's function, 16
- Maeda, 2
- Maeda et al., 2
- Marchenko
  - Voliak, 5
- Masson
  - and LeBlond, 5
- Mey, 15
- Meylan, 4–6, 8, 18
  - , Squire, and Fox, 5
  - and Squire, 3
  - constant panel method (see also constant panel method), 26
  - et al., 5
  - method (see also constant panel method), 5, 6, 18, 26, 37, 108
    - Green's matrix, 28
    - library of codes, 29
    - two-dimensional beam, 85
- MIZ (Marginal Ice Zone), 1, 3–5, 110
- modes
  - evanescent, 71
  - propagation, 71
    - order 0, 72
    - real and pure imaginary, 72
- modulus of rigidity,  $D$ , 11
- Moritz and Ukita, 5
- Newton-Raphson, 117
- panel
  - arithmetic sum of the total number of, 41
- periodic array of plates
  - elastic and discrete
    - scattered waves due to, 94
- periodic Green's function, 62
  - accelerated, 83
    - convergence test, 80
  - accelerated (see also fast-convergent), 70
  - asymptotic form, 7
  - convergence of, 67
  - far-field, 66, 67

- fast-convergent (see also accelerated), 110
- near-field, 66
- slow-convergence, 7
- slow-convergent
  - far-field, 79
  - near-field, 79
- slow-convergent test, 83
- spatial
  - singularity, 68
- spectral, 67, 83
  - singularity, 68
- the divergence of, 73
- truncating the spectral representation of, 72
- periodic Green's functions
  - accelerated, 79
- periodic line-array of plates
  - connection with diffraction gratings, 63
  - elastic and discrete
    - displacement of, 102
  - relating the wavelength, waveangle, and channel's width, 89
  - relationship with two-dimensional beam, 85
  - stiff and unmovable, 87
    - effect on the angular scattering, 87
- periodic Green's function
  - convergence of
    - far-field (spatial), 68
    - far-field (spectral), 68
    - near-field, 68
- Petyt, 37
- phase difference, 63
- Poisson's ratio  $\nu$ , 11
- potential
  - boundary integral equation
    - solution, 18
- pressure
  - dimensionless coupled equation, 13
- pressure-distribution method, 1, 2
- propagating wave
  - order 0, 75
- propagation angle, 80
- propagation constants, 67, 71, 72, 75
  - order 0, 75, 77
- reflected wave, 75, 77, 78
  - coefficient, 77
- Sarpkaya and Isaacson, 15
- scattered wave, 74
  - reflected wave, 77
  - spectrum of, 74
  - transmitted wave, 77
- scattered waves, 74
- scattered waves (see also diffracted waves), 71
- shallow-draft model, 1
- single frequency
  - displacement, 13
  - equations of motion, 12
- smoothing factor, 70, 79
  - the effect on convergence, 80
- Sommerfeld radiation condition
  - see also boundary condition, 13
- source panel, 32
- spatial variables
  - non-dimensionalized, 11
- Squire
  - et al., 4
- stiffness constant,  $\beta$ , 12
- Stoker, 8, 113
- Takaki
  - and Gu, 2
  - and Lin, 2
- time variables
  - non-dimensionalized, 11
- transmitted wave, 75, 77, 78
  - coefficient, 78
- variational equation
  - see also coupled pressure equation, 23

VLFS (Very Large Floating Structure), 1, 3

Wadhams, 4

Watanabe et al., 1

wavelength,  $\lambda$ , 13

wavenumber

infinite depth,  $\alpha$ , 13

finite depth,  $k$ , 13

Wehausen and Laitone, 16

wet modes, 3

wet-modes, 2

Yago and Endo, 2

Yasuzawa et al., 2, 3

Young's modulus,  $E$ , 11